Pattern Formation and Anomalous modes in Axisymmetic, Compressible Taylor-Couette Flow

A Thesis
Submitted for the Degree of
MS(ENGG.)

by

PRATIK AGHOR

ENGINEERING MECHANICS UNIT
JAWAHARLAL NEHRU CENTRE FOR ADVANCED SCIENTIFIC RESEARCH
(A Deemed University)
Bangalore – 560 064

April 2018

I strongly believe that one does not need to be a ‘genius’ (as portrayed by popular romantic ideas) to produce good scientific work. I dedicate this thesis to all ‘ordinary’ girls and boys who have been told that they are not geniuses, but whose scientific spirits still remain unvanquished.

DECLARATION

I hereby declare that the matter embodied in the thesis entitled “**Pattern Formation and Anomalous modes in Axisymmetic, Compressible Taylor-Couette Flow**” is the result of investigations carried out by me at the Engineering Mechanics Unit, Jawaharlal Nehru Centre for Advanced Scientific Research, Bangalore, India under the supervision of **Prof. M. Alam**, and that it has not been submitted elsewhere for the award of any degree or diploma.

In keeping with the general practice in reporting scientific observations, due acknowledgment has been made whenever the work described is based on the findings of other investigators.

Pratik Aghor

CERTIFICATE

I hereby certify that the matter embodied in this thesis entitled "**Pattern Formation and Anomalous modes in Axisymmetic, Compressible Taylor-Couette Flow**" has been carried out by **Mr. Pratik Aghor** at the Engineering Mechanics Unit, Jawaharlal Nehru Centre for Advanced Scientific Research, Bangalore, India under my supervision and that it has not been submitted elsewhere for the award of any degree or diploma.

Prof. M. Alam
(Research Supervisor)

Acknowledgements

To begin with, I would like to thank Prof. Alam for his guidance and support. Working with him has been a huge learning experience for me. He always encouraged valid scientific questions. I still remember a conversation I had with him over a lunch about odd-numbered rolls in Taylor-Couette flow (TCF). I was oblivious of the extensive research on ‘anomalous modes’ [Benjamin [4]] in the incompressible TCF. He told me that there have been studies on such ‘exotic’ things. It was just a curious thought and I did not pursue it any further. However, the next day Prof. Alam gave me about fifteen research papers to read which got me extremely interested in these anomalous modes as well as things like transitions from n to $n+2$ rolls and hysteresis associated with it. He also introduced me to ‘chaosbook’ by Cvitanović et al. [11] which helped me confirm my research interests and gave me challenging side-projects such as tracking snaking branches corresponding to spatially localized solutions of the Swift-Hohenberg equation. Prof. Alam was patient with me when I was pestered with bugs in my code. His Zen advice of ‘Do it!’ reflected his belief in my abilities which I greatly appreciated. I also deeply value the creative freedom he granted me with during this work, for example, Chapter 4 of this thesis would not have been possible without that freedom. Finally, during the writing of this thesis, his active interest and encouragement helped me improve my scientific writing.

I thank Prof. Ganesh Subramanian, Prof. Santosh Ansumali, Prof. K.R. Sreenivas, Prof. Meher Prakash, Prof. Kavita Jain and Prof. Rajesh Ganapathy for their amazing courses. I would also like to thank Prof. Tapomoy Guha Sarkar, Prof. Sai Jagan Mohan and Prof. Amol Marathe for their guidance and help during my undergraduate years at BITS Pilani.

I thank my friends at EMU: Mayank Toprani, Pulkit Dubey, Mohammad Atif, Piyush Garg, Prateek Anand, Rafiuddin Mohammad (Rafi), Praveen Kolluru and Arun Varanasi for interesting discussions and helping me fix bugs in my code. Thanks to Vybhav Yalasi and Rafi for helping me with the experimental project. I thank my lab-mates Achal Mahajan, Ronak Gupta, Nandu Gopan, (T)Sunil Bharadwaj, Ramkrishna Rongali and Saikat Saha for welcoming me to Prof. Alam’s lab. I also thank V.K. Ponnulakshmi for being a well-wisher and helping me prepare for my comprehensive examination. Thanks to Tanumoy Dhar for his innocent questions; I have learned many things while answering them. Interactions with him as well as Pulkit Dubey and Mayank Toprani have made me realize where I stand on ‘how should one do science?’ I thank my friend Kaveri for good literature suggestions and times. I am grateful for her moral support and love. I thank Chaitanya Mokashi, Aaditya Anand, Prashanth Ramesh and Ruchir Dwivedi for helping me with my PhD applications and for being awesome friends. I have had immense number of discussions, scientific and otherwise, with Ruchir, which I greatly benifited from. Thanks to Akhilesh Bhagurkar, Alankrit Kharbanda and Mukul Khedwal for being great retreats. Taking up martial arts training was one of the best decisions I have taken and I thank Pritha Kundu, Srikant Venkitachalam and Pulkit Dubey for dragging me to Kung-Fu classes even when I was worried about work or simply bored. It provided me with a change of environment and intensive workout which made my mind clearer, and I was able to work better.

I would also like to express my gratitude towards Richard Feynman, V. Balakrishnan (Balki), Leonard Susskind and Predrag Cvitanović: professors I never interacted with but from whose courses and books I have learned a great deal of physics and mathematics.

Finally, I thank my family for always being there and making me realize that no matter what happens, I have a place to belong to.

Abstract

In this thesis, pattern formation in axisymmetric, compressible Taylor-Couette flow (TCF) is studied via direct numerical simulation. Taylor-Couette flow is the annular flow between two concentric, differentially rotating cylinders. It is known for its rich complexity of patterns and makes a good test-case for validating theory and numerics as it is experimentally feasible. Throughout this study, the outer cylinder is kept stationary while the inner cylinder is rotated at different angular velocities. In chapter 1, a brief history of the incompressible Taylor-Couette problem is presented. Rayleigh's inviscid instability criterion is derived using an energy argument. An overview of the literature on compressible TCF is given.

In chapter 2, a numerical code is developed using finite differences to solve governing equations in a cylindrical geometry. Governing equations are compressible Navier-Stokes equations coupled with the energy equation and an equation of state for an ideal gas. Equations are written in the rest frame of reference in cylindrical co-ordinates with axisymmetry imposed. Boundary conditions are no-slip at walls, periodic in the axial direction (z) for infinite cylinders and no-slip (Dirichlet) in $z-$direction in case of finite cylinders. Non-dimensionalization is done based on the viscous time-scale and the average density of the gas. This choice of characteristic scales is motivated by experiments. The dimensionless equations are coded using finite difference method. Numerical method and its implementation are described. Benchmarking is done by comparing the results with the published literature on thermally- and mechanically-driven flows. Physical explanations for the flow profiles are given.

In chapter 3, another verification of the code is presented by matching the analytically known base state of the compressible TCF to the one obtained via long-time marching of time dependent compressible Navier-Stokes equations. Observations and interpretations are given based on the base-state profiles. Effects of variable viscosity on the onset of Taylor vortex flow (TVF) are investigated. It is found that when viscosity is described by well-known Sutherland's law of shear viscosity, the critical inner Reynolds number (Re_1) for the onset of instability increases compared to that for a constant viscosity. Hence, we conclude that variable viscosity stabilizes the Taylor-Couette flow.

At higher Re_1, it is found that when axisymmetry is imposed, TVF bifurcates to a traveling wave propagating in the negative axial direction (i.e., negative $z-$direction). Dominant frequen-

cies of the time series are extracted from the kinetic energy versus time graphs via fast Fourier transform (FFT). First and second dominant frequencies are plotted against Re_1. In order to understand how dominant and sub-dominant frequencies vary with the rotation rate of the inner cylinder, dimensionless frequencies are also plotted on the inertial time-scale.

Chapter 4 is dedicated for studying finite-size effects in the Taylor-Couette system. The so-called 'anomalous modes' of Benjamin [4], especially single-cell modes (or, asymmetric two-cell modes) are obtained in the compressible TCF for small aspect ratios ($\Gamma = h/d \sim 1$, where h is the height of cylinders and $d = R_2 - R_1$ is the gap width). Bifurcation from mid-plane symmetric Taylor vortex flow (TVF) to asymmetric single-cell modes is characterized and the bifurcation diagrams are plotted for different values of Γ. Some speculations and guesses are presented concerning the bifurcation scenario and a qualitative phase diagram is plotted in the (Re_1, Γ) plane, delineating the regions of normal and anomalous modes. These two regions seem to be connected via a line of limit points for the present case of compressible TCF at a Mach number of unity.

When Γ is increased from 3.1 to 6.1 and then decreased back again to 3.1, keeping the Re_1 constant, interesting behavior is observed. At $Re_1 = 100$ and 125, while increasing Γ, a $2 \rightarrow 4 \rightarrow 6$-roll transitions are observed and while coming back $6 \rightarrow 4 \rightarrow 2$-roll transitions are seen. However, at higher $Re_1 = 150$ and 200, while increasing Γ, a direct $2 \rightarrow 6$-roll jump is seen but while coming back, $6 \rightarrow 4 \rightarrow 2$-roll jumps are observed. These observations indicate that the bifurcation diagrams in (Γ, Re_1) plane are more complicated than a simple cusp catastrophe. It appears that pattern formation in the (Γ, Re_1) plane of compressible TCF has more than one cusp entangled with each other.

In chapter 5, a discussion and summary of the work is presented with possible directions for future work.

Table of contents

List of figures xvii

List of tables xxiii

1 Introduction 1

1.1 A Brief History of Taylor-Couette Flow . . . 1
1.2 Why Study Taylor-Couette flow? . . . 5
1.3 Previous Work on the Compressible TCF . . . 6
1.4 Outline of the thesis . . . 7

2 Numerical Implementation and Code Validation 9

2.1 Introduction and Governing Equations . . . 9
2.1.1 Governing Equations and Boundary Conditions . . . 10
2.2 Numerical Method and its Implementation . . . 12
2.3 Developing Finite Difference Approximation . . . 13
2.3.1 The Finite Difference Approximation . . . 13
2.3.2 Donor Cell or Upwind Scheme for Convective Derivatives . . . 15
2.3.3 Caveats While Using the DuFort-Frankel Leapfrog Type Scheme . . . 17
2.3.4 The Remedy: Filtering . . . 18
2.4 Putting It All Together . . . 19
2.5 Physical Interpretation of Results . . . 20
2.5.1 Thermally Driven Flow . . . 21
2.5.2 Mechanically Driven Flow . . . 23
2.6 Thermally Driven Flow - Code Validation . . . 24
2.7 Mechanically Driven Flow - Code Validation . . . 26
2.8 Summary and Conclusion . . . 29

3 Compressible Taylor-Couette Flow 31

3.1 Introduction . . . 31

3.2 Dimensional Governing Equations 32
3.3 General Dimensionless Equations 33
3.3.1 Method 1 35
3.3.2 Method 2 36
3.4 Dimensionless Governing Equations and Boundary Conditions in Cylindrical Coordinates 38
3.4.1 Governing Equations for an Axisymmetric Flow 41
3.4.2 Writing Governing Equations in Terms of $\bar{\rho}$ 42
3.4.3 Numerical Method 44
3.5 Verifying the Base State for Compressible Taylor-Couette Flow 44
3.5.1 Observations and Interpretation 48
3.6 Effect of Variable Transport Coefficients 49
3.6.1 Average Kinetic Energies 49
3.6.2 Sutherland's Law of Shear Viscosity 50
3.6.3 Circulation of a Two-roll Structure - Comparison 51
3.6.4 Radial Average of Radial Velocity versus z - Comparison 53
3.6.5 Specific Angular Momentum 55
3.6.6 Local Mach Number 55
3.6.7 Procedure to Analyze Bifurcation 57
3.6.8 Typical Fields Before and After Bifurcation - Varying Re_1 at $k = 4$ . . 58
3.6.9 Varying Height of the Computational Domain, at $Re_1 = 100$ 59
3.7 Results at Higher Reynolds Numbers 61
3.7.1 $Re_1 = 190$ 63
3.7.2 $Re_1 = 210$ 65
3.7.3 $Re_1 = 230$ 67
3.7.4 $Re_1 = 250$ 69
3.7.5 $Re_1 = 270$ 71
3.7.6 Plotting Dominant Frequencies and Amplitudes against Re_1 73
3.8 Summary and Conclusion 77

4 Finite-Size Effects and Anomalous Modes **79**
4.1 Introduction 79
4.2 Breaking Mid-plane Symmetry: Single-Cell Modes 83
4.2.1 Numerical Method 83
4.2.2 Temperature Boundary Condition Trick 83
4.2.3 Other ways of Manifesting Single-cell Modes 85
4.3 Quantification of Bifurcation from a Two-roll to a Single-roll Structure 86

4.3.1 Comparison Between Single-cell Modes Obtained from Different Procedures at $\Gamma = 1$ 89
4.3.2 Uncovering the Bifurcation Scenario in the (Re_1, Γ) Plane 89
4.3.3 Discussion on Single-cell Modes 90
4.4 Changing Γ at a Given Re_1 93
4.4.1 Changing Γ at $Re_1 = 100$ 93
4.4.2 Changing Γ at $Re_1 = 125$ 97
4.4.3 Changing Γ at $Re_1 = 150$ 100
4.4.4 Changing Γ at $Re_1 = 200$ 103
4.5 Summary and Conclusion 107

5 Summary and Outlook **109**
5.1 Pattern Formation in Compressible TCF with Periodic Boundary Conditions . 110
5.2 Finite-size Effects in Compressible TCF 112
5.3 Possible Future Work 115

References **117**

List of figures

1.1 Geometry of Taylor-Couette setup, Taylor [39] 1

1.2 Rayleigh line in the phase plane. 4

1.3 Taylor's viscous stability criterion - blue line. 4

1.4 Phase plane of the Newtonian, incompressible Taylor-Couette setup. Taken from Andereck et al. [1]. Here $Re_i = \Omega_i R_i d/\nu$ and $Re_o = \Omega_o R_o d/\nu$ represent Reynolds number based on inner and outer cylinder velocities $\Omega_i R_i$ and $\Omega_o R_o$, respectively. Ω_i and Ω_o are angular velocities of inner and outer cylinders, respectively. d is the gap width $R_o - R_i$ and ν is the kinematic viscosity of the fluid. 5

2.1 Domain. 9

2.2 Boundary conditions: (a) Thermally driven flow and (b) Mechanically driven flow. 10

2.3 Four possible cases for upwind scheme. 16

2.4 Time series for kinetic energies, case 2 from Table - 2.2: (a) KE_u, (b) KE_w. . 20

2.5 Thermally driven flow. 21

2.6 Velocity vector plot for thermally driven flow, case 2 (Table - 2.2). 22

2.7 Mechanically driven flow. 23

2.8 Mechanically driven flow: velocity vector plots for (a) case 3 and (b) case 4 (Table - 2.2). 24

2.9 Profiles in black are from Harada [17], colored ones are from the present code (a) u vs z at different r, (b) v vs z at different r, (c) w vs r at $z = 0.5$. 25

2.10 Temperature contours, case 2, (Table - 2.2) (a) present code and (b) Harada [17]. 26

2.11 Azimuthal velocity contours, case 2, (Table - 2.2) (a) present code and (b) Harada [17]. 26

2.12 Profiles in black are from Harada [17], colored ones are from the present code. (a) angular velocity $\frac{v+r}{r}$ vs r at different z, case 3, (b) angular velocity $\frac{v+r}{r}$ vs z at different r, case 3, (c) u vs z at different r, case 3, (d) w vs r at different z, case 3, (e) angular velocity $\frac{v+r}{r}$ vs z at different r, case 4, (f) w vs r at different z, case 4. 27
2.13 Temperature contours, case 3, (Table - 2.2) (a) present code and (b) Harada [17]. 28
2.14 Temperature contours, case 4, (Table - 2.2) (a) present code and (b) Harada [17]. 28
2.15 Azimuthal velocity contours contours, case 3, (Table - 2.2) (a) present code and (b) Harada [17]. 29

3.1 Taylor-Couette flow (TCF) with periodic boundaries in z-direction. 31
3.2 Base state for $Pr = 1, Re_2 = 0, Re_1 =$ close to critical, varying Ma: (a)v_0 versus r, (b)T_0 vs r, (c) ρ_0 vs r. 47
3.3 Base state for $Ma = 1, Re_2 = 0, Re_1 =$ close to critical, varying Pr: (a)v_0 versus r, (b)T_0 vs r, (c) ρ_0 vs r. 48
3.4 Checking grid independence: $Re_1 = 75, k = 4, Ma = 1, Pr = 1$: (a) KE_u versus t and (b) KE_w versus t. 50
3.5 Velocity vector plots in the (r,z) plane for CCF and TVF: $k = 2\pi/h = 4, Ma = 1$ and $Pr = 1$: (a) $Re_1 = 71(< Re_c)$ and (b) $Re_1 = 75(> Re_c)$. 51
3.6 Average circulation versus Re_1 with $Ma = 1$ and $Pr = 1$ for constant and variable viscosity for different heights $(= 2\pi/k)$ of the computational domain: (a) $k = 3.1729$ and (b) $k = 4$. 52
3.7 r-averaged values of the radial velocity versus z: (a) $k = 3.1729$, constant μ, (b) $k = 3.1729$, variable μ,(c) $k = 4$, constant μ, (d) $k = 4$, variable μ. 53
3.8 Schematic of the axial profile of $< u >_r$ 54
3.9 r-averaged u vs Re_1 comparison for constant and variable viscosity for different heights $(= 2\pi/k)$ of the computational domain with $Ma = 1$, $Pr = 1$, (a) $k = 3.1729$ and (b) $k = 4$. 54
3.10 Cartoon of the procedure. 57
3.11 Constant viscosity: First panel: $Re_1 = 71$, Second panel: $Re_1 = 75$, Third panel: $Re_1 = 78$. (a) velocity plot, (b) ρ, (c) T, (d) $\mathscr{L}_s$, (e) azimuthal velocity (v). 58
3.12 Variable viscosity: First panel: $Re_1 = 78$, Second panel: $Re_1 = 83$. (a) velocity plot, (b) ρ contours, (c) T contours, (d) $\mathscr{L}_s$ contours, (e) azimuthal velocity (v) contours. 59
3.13 $Re_1 = 100, Re_2 = 0$, constant viscosity, (i) $k = 2$, (ii) $k = 3$, (iii) $k = 4$, (iv) $k = 5$, (v) $k = 6$, (vi) $k = 7$, (a) velocity plot, (b) ρ contours, (c) T contours, (d) $\mathscr{L}_s$ contours, (e) azimuthal velocity v contours (f) local Ma contours. 60

3.14 $Re_1 = 100, Re_2 = 0$, variable viscosity, (i) $k = 2$, (ii) $k = 3$, (iii) $k = 4$, (iv) $k = 5$, (v) $k = 6$, (vi) $k = 7$. (a) velocity plot, (b) ρ contours, (c) T contours, (d) $\mathscr{L}_s$ contours, (e) azimuthal velocity v contours (f) local Ma contours. . . . 61

3.15 $Re_1 = 190, Re_2 = 0$, $k = 4$, traveling wave: (a) velocity plot, (b) ρ contours, (c) T contours, (d) $\mathscr{L}_s$ contours, (e) azimuthal velocity v contours (f) local Ma contours. 63

3.16 Time series for kinetic energies, $Re_1 = 190$, traveling wave: (a) KE_u and (b) KE_w. Fig. 3.15 shows snapshots of the flow at the marked points. 64

3.17 $Re_1 = 190$, traveling wave, single-sided amplitude spectrum for: (a) KE_u and (b) KE_w. 64

3.18 $Re_1 = 210, Re_2 = 0$, $k = 4$, traveling wave: (a) velocity plot, (b) ρ contours, (c) T contours, (d) $\mathscr{L}_s$ contours, (e) azimuthal velocity v contours (f) local Ma contours. 65

3.19 Time series for kinetic energies, $Re_1 = 210$, traveling wave: (a) KE_u and (b) KE_w. Fig. 3.18 shows snapshots of the flow at the marked points. 66

3.20 $Re_1 = 210$, traveling wave, single-sided amplitude spectrum for: (a) KE_u and (b) KE_w. 66

3.21 $Re_1 = 230, Re_2 = 0$, $k = 4$, traveling wave: (a) velocity plot, (b) ρ contours, (c) T contours, (d) $\mathscr{L}_s$ contours, (e) azimuthal velocity v contours (f) local Ma contours. 67

3.22 Time series for kinetic energies, $Re_1 = 230$, traveling wave: (a) KE_u and (b) KE_w. Fig. 3.21 shows snapshots of the flow at the marked points. 68

3.23 $Re_1 = 230$, traveling wave, single-sided amplitude spectrum for: (a) KE_u and (b) KE_w. 68

3.24 $Re_1 = 250, Re_2 = 0$, $k = 4$, traveling wave: (a) velocity plot, (b) ρ contours, (c) T contours, (d) $\mathscr{L}_s$ contours, (e) azimuthal velocity v contours (f) local Ma contours. 69

3.25 Time series for kinetic energies, $Re_1 = 250$, traveling wave: (a) KE_u and (b) KE_w. Fig. 3.24 shows snapshots of the flow at the marked points. 70

3.26 $Re_1 = 250$, traveling wave, single-sided amplitude spectrum for: (a) KE_u and (b) KE_w. 70

3.27 $Re_1 = 270, Re_2 = 0$, $k = 4$, traveling wave: (a) velocity plot, (b) ρ contours, (c) T contours, (d) $\mathscr{L}_s$ contours, (e) azimuthal velocity v contours (f) local Ma contours. 71

3.28 Time series for kinetic energies, $Re_1 = 270$, traveling wave: (a) KE_u and (b) KE_w. Fig. 3.27 shows snapshots of the flow at the marked points. 72

3.29 $Re_1 = 270$, traveling wave, single-sided amplitude spectrum for: (a) KE_u and (b) KE_w. 72

3.30 Dominant Amplitudes (a,b) and Frequencies (c) for KE_u and KE_w versus Re_1: (a) Dominant amplitude versus Re_1 for Ke_u, (b) Dominant amplitude versus Re_1 for Ke_w, (c) Dominant frequency versus Re_1. 74

3.31 Second dominant Amplitudes (a,b) and Frequencies (c) for KE_u and KE_w versus Re_1: (a) Second dominant amplitude versus Re_1 for Ke_u, (b) Second dominant amplitude versus Re_1 for Ke_w, (c) Second dominant frequency versus Re_1. 75

3.32 (a) First dominant frequency versus Re_1, (b) second-dominant frequency versus Re_1 and (c) ratio of f_{1max} and f_{2max} versus Re_1 on inertial time-scale. 76

4.1 (a) Finite-cylinders geometry and (b)dimensionless boundary conditions for TCF with rigid lids at top and bottom. 79

4.2 Mid-plane symmetric Taylor-vortex mode. 80

4.3 A schematic of anomalous modes. 81

4.4 A schematic of the cusp catastrophe taken from Benjamin [4]. 82

4.5 Single-cell modes, $Re_1 = 180$, $Ma = 1$, $Pr = 1$, $\Gamma = 1$: (a) $\varepsilon = 0.1$, (b) $\varepsilon = -0.1$. 84

4.6 Temperature Boundary condition trick, $\varepsilon = 0.1$: $Re_1 = 180$, $Ma = 1$, $Pr = 1$, $\Gamma = 1$ (a) $t = 0$: temperature gradient switched on, (b) $t = 8$: single-cell mode settles, (c) $t = 16$: temperature gradient switched off, (d) $t = 24$: single-cell mode survives. 84

4.7 Temperature Boundary condition trick, $\varepsilon = -0.1$: $Re_1 = 180$ (a) $t = 0$: temperature gradient switched on, (b) $t = 8$: single-cell mode settles, (c) $t = 16$: temperature gradient switched off, (d) $t = 24$: single-cell mode survives. 85

4.8 Bifurcation diagrams: w at mid-plane, mid-height versus Re_1 for different Γ; $Ma = 1$, $Pr = 1$. 87

4.9 Transition from symmetric 2-roll (Panel (b)) to 1-roll (asymmetric 2-roll) solutions (Panel (c) and (d)): (a) Upper branch of the bifurcation diagram of Fig. 4.8d. Velocity plots at points marked in Fig. 4.9a: (b) $Re_1 = 158$, (c) $Re_1 = 170$, (d) $Re_1 = 175$ at $\varepsilon = 0.1$, $Ma = 1$, $Pr = 1$, $\Gamma = 1$. 88

4.10 Comparison between bifurcation diagrams generated by different methods with $\Gamma = 1$, $Ma = 1$, $Pr = 1$: (i) blue circles- using the temperature gradient trick and (ii) black circles- abrupt change in Γ. 89

4.11 Qualitative phase diagram in the (Re_1, Γ) plane. 90

4.12 (a) Subcritical bifurcation and (b) subcritical bifurcation from infinity. 92

4.13 Velocity vector plots in (r,z) plane at $Re_1 = 100$, $Re_2 = 0$, $Ma = 1$, $Pr = 1$, increasing Γ from 3.1 to 6.1. 94

4.14 Velocity vector plots in (r,z) plane at $Re_1 = 100$, $Re_2 = 0$, $Ma = 1$, $Pr = 1$, decreasing Γ from 6.1 to 3.1. 95

4.15 A schematic of hysteresis seen in the bifurcation diagram at $Re_1 = 100$. . . . 96

4.16 $Re_1 = 100$, $Re_2 = 0$, $Ma = 1$, $Pr = 1$, vary Γ, time series for (a) KE_u and (b) KE_w. 97

4.17 Velocity vector plots in (r,z) plane at $Re_1 = 125$, $Re_2 = 0$, $Ma = 1$, $Pr = 1$, increasing Γ from 3.1 to 6.1. 98

4.18 Velocity vector plots in (r,z) plane at $Re_1 = 125$, $Re_2 = 0$, $Ma = 1$, $Pr = 1$, decreasing Γ from 6.1 to 3.1. 99

4.19 $Re_1 = 125$, $Re_2 = 0$, $Ma = 1$, $Pr = 1$, vary Γ, time series for (a) KE_u and (b) KE_w. 100

4.20 A schematic of hysteresis seen in the bifurcation diagram at $Re_1 = 125$. . . . 100

4.21 Velocity vector plots in (r,z) plane at $Re_1 = 150$, $Re_2 = 0$, $Ma = 1$, $Pr = 1$, increasing Γ from 3.1 to 6.1. 101

4.22 Velocity vector plots in (r,z) plane at $Re_1 = 150$, $Re_2 = 0$, $Ma = 1$, $Pr = 1$, increasing Γ from 6.1 to 3.1. 102

4.23 $Re_1 = 150$, $Re_2 = 0$, $Ma = 1$, $Pr = 1$, vary Γ, time series for (a) KE_u and (b) KE_w. 103

4.24 A schematic of hysteresis seen in the bifurcation diagram at $Re_1 = 150$. . . . 103

4.25 Velocity vector plots in (r,z) plane at $Re_1 = 200$, $Re_2 = 0$, $Ma = 1$, $Pr = 1$, increasing Γ from 3.1 to 6.1. 104

4.26 Velocity vector plots in (r,z) plane at $Re_1 = 200$, $Re_2 = 0$, $Ma = 1$, $Pr = 1$, decreasing Γ from 6.1 to 3.1. 105

4.27 $Re_1 = 200$, $Re_2 = 0$, $Ma = 1$, $Pr = 1$, vary Γ, time series for (a) KE_u and (b) KE_w. 106

4.28 A schematic of hysteresis seen in the bifurcation diagram at $Re_1 = 200$. . . . 107

4.29 Schematics of hysteresis for (a) $Re_1 = 100$, (b) $Re_1 = 125$, (c) $Re_1 = 150$, (d) $Re_1 = 200$. 108

5.1 Geometry of the Taylor-Couette setup, Taylor [39]. 109

5.2 Average circulation versus Re_1 with $Ma = 1$ and $Pr = 1$ for constant and variable viscosity for different heights $(= 2\pi/k)$ of the computational domain: (a) $k = 3.1729$ and (b) $k = 4$. 110

5.3 Traveling wave at $Re_1 = 190$, $Re_2 = 0$, $Ma = 1$, $Pr = 1$, $k = 2\pi/h = 4$: (a) Time series for kinetic energy KE_u, (b) single-sided amplitude spectrum for KE_u. Figures 5.3c-5.3g show snapshots of the velocity vector plots at points marked in Fig. 5.3a. Velocity vector plots at (c) $t = 7$, (d) $t = 10$, (e) $t = 10.4$, (f) $t = 11$, (g) $t = 11.8$. 111
5.4 Transition from symmetric 2-roll (Panel (b)) to 1-roll (asymmetric 2-roll) solutions (Panel (c) and (d)): (a) Upper branch of the bifurcation diagram of Fig. 4.8d. Velocity plots at points marked in Fig. 5.4a: (b) $Re_1 = 158$, (c) $Re_1 = 170$, (d) $Re_1 = 175$ at $\varepsilon = 0.1$, $Ma = 1$, $Pr = 1$, $\Gamma = 1$. 113
5.5 Qualitative phase diagram in the (Re_1, Γ) plane. 114
5.6 Schematics of hysteresis for (a) $Re_1 = 100$, (b) $Re_1 = 125$, (c) $Re_1 = 150$, (d) $Re_1 = 200$. 115

List of tables

2.1 Characteristic quantities 10
2.2 Cases from Harada [17]. 20

3.1 Reference Scales. 35
3.2 Higeher Re_1: dominant frequencies and amplitudes 73
3.3 Higeher Re_1: second dominant frequencies and amplitudes 74

Chapter 1

Introduction

"It seems doubtful whether we can expect to understand fully the instability of fluid flow without obtaining a mathematical representation of the motion of a fluid in some particular case in which instability can actually be observed, so that a detailed comparison can be made between the results of analysis and those of experiment." - G.I. Taylor

1.1 A Brief History of Taylor-Couette Flow

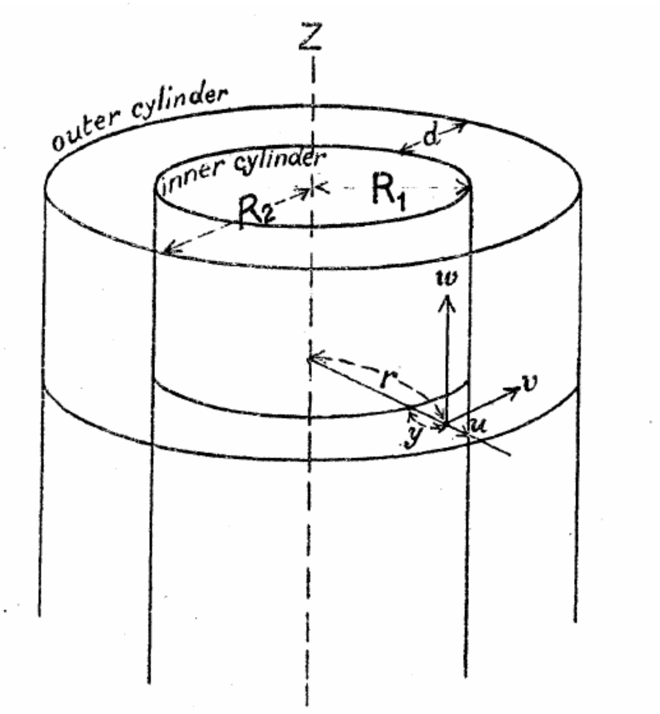

Fig. 1.1 Geometry of Taylor-Couette setup, Taylor [39]

Taylor-Couette flow is the annular flow between two concentric, differentially rotating cylinders. Figure 1.1 shows the geometry of the setup and is taken from Taylor [39]. Due to its geometric simplicity, this flow has been a topic of scientific investigation for centuries - for example, Newton [30] used the setup to describe the flow of rotating fluids in his *Principia* in 1687. In 1880, Stokes [36] made an attempt of investigation of the flow and realized the difficulty lied in the treatment of boundary conditions.

The advent of Navier-Stokes equations led to a debate on how one can determine the viscosity of a fluid. Both Mallock [25] and Couette [10] independently came up with the idea of resolving this question by studying the flow of a fluid using differentially rotating concentric cylinders. Couette only rotated the outer cylinder, keeping the inner cylinder fixed. In addition to the experiments on the same lines as Couette, Mallock also rotated the inner cylinder, keeping the outer cylinder fixed.

The main theoretical stride began in 1916, when Rayleigh [33] gave a physical explanation and demonstrated the existence of an instability in an inviscid, rotating fluid. One can give an energy based argument to show Rayleigh's inviscid instability criterion. Consider a swirling flow where the angular velocity $\Omega(r)$ is an arbitrary function of the radial dependence r. The axisymmetric, inviscid governing equations can be written in the polar co-ordinates r, ϕ and z as follows:

Continuity:

$$\frac{\partial u_r}{\partial r}+\frac{u_r}{r}+\frac{\partial u_z}{\partial z}=0 \tag{1.1}$$

Momentum:

$$\frac{Du_r}{Dt}-\frac{u_\phi^2}{r}=-\frac{1}{\rho}\frac{\partial p}{\partial r} \tag{1.2a}$$

$$\frac{Du_\phi}{Dt}+\frac{u_r u_\phi}{r}=0 \tag{1.2b}$$

$$\frac{Du_z}{Dt}=-\frac{1}{\rho}\frac{\partial p}{\partial z} \tag{1.2c}$$

where the material derivative is

$$\frac{D}{Dt}=\frac{\partial}{\partial t}+u_r\frac{\partial}{\partial r}+u_z\frac{\partial}{\partial z}. \tag{1.3}$$

Consider the initial flow to be purely azimuthal, i.e.,

$$\underline{u}=u_\phi(r)\hat{\phi}, \tag{1.4}$$

where $\hat{\phi}$ is a unit vector in the ϕ-direction and u_ϕ is an arbitrary function of r given by

$$u_\phi = r\Omega(r). \tag{1.5}$$

One can recast the azimuthal momentum balance in ϕ direction as follows:

$$\frac{D(ru_\phi)}{Dt} = 0. \tag{1.6}$$

Equation (1.6) implies that the quantity $H = ru_\phi$ is conserved for a material volume. H is nothing but the angular momentum of a material blob of fluid. As this is an inviscid analysis, there is no viscous dissipation and the conservation of angular momentum makes intuitive sense. Now one can define the kinetic energy per unit volume associated with the azimuthal motion in terms of H as follows:

$$\frac{1}{2}\rho u_\phi^2 = \frac{1}{2}\frac{\rho H^2}{r^2}. \tag{1.7}$$

Let us consider two material volumes of equal volume dV at different radial locations, one at $r = r_1$ and the other at $r = r_2$. We assume $r_2 > r_1$ without loss of generality. Their total kinetic energy per unit volume will be:

$$KE_{initial} = \frac{1}{2}\rho\left(\frac{H_1^2}{r_1^2} + \frac{H_2^2}{r_2^2}\right). \tag{1.8}$$

Imagine that these two material elements swap positions. Because of Eqn.(1.6), each material element retains its angular momentum. After the swap, the new kinetic energy per unit volume will be:

$$KE_{new} = \frac{1}{2}\rho\left(\frac{H_1^2}{r_2^2} + \frac{H_2^2}{r_1^2}\right), \tag{1.9}$$

and hence

$$KE_{new} - KE_{initial} = \frac{1}{2}\rho(H_2^2 - H_1^2)\left(\frac{1}{r_1^2} - \frac{1}{r_2^2}\right). \tag{1.10}$$

As $r_2 > r_1$, $\left(\frac{1}{r_1^2} - \frac{1}{r_2^2}\right) > 0$. If the swap releases energy, i.e., if $KE_{new} - KE_{initial} < 0$, or, $H_2^2 - H_1^2 < 0$, the base flow will be unstable. That is, if H^2 decreases with r the flow is unstable. Hence the criterion for instability is given by

$$\frac{d(H^2)}{dr} < 0. \tag{1.11}$$

The above criterion (1.11) is known as **Rayleigh's inviscid instability criterion.**

In the (Ω_2, Ω_1) plane, the Rayleigh line is given by $\Omega_1 r_1^2 = \Omega_2 r_2^2$ in case of the Taylor-Couette flow, where R_1 and R_2 are the radii of the inner and outer cylinders, respectively. This is depicted by the red line in Fig. 1.2

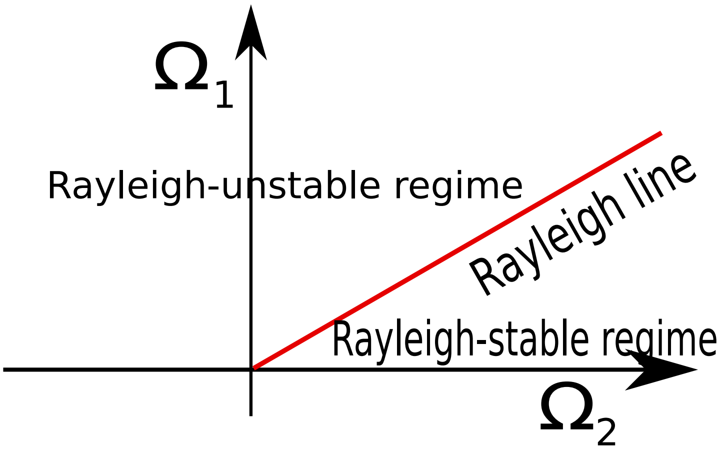
Ω_1
Rayleigh-unstable regime
Rayleigh line
Rayleigh-stable regime
Ω_2

Fig. 1.2 Rayleigh line in the phase plane.

In his seminal paper of 1923, Taylor [39] performed the linear stability analysis for viscous fluids based on the Navier-Stokes equations and no-slip boundary conditions at the wall. He also performed experiments and matched them with his theoretical results. The results were accurate and historically important because they established the validity of the no-slip boundary conditions and gave the first experimental evidence for the validity of the Navier-Stokes equations. The blue line in Fig. 1.3 represents a schematic of Taylor's neutral stability curve in (Ω_2, Ω_1) - plane.

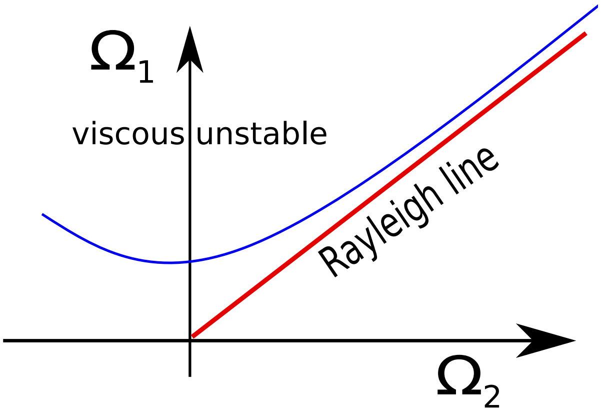
Ω_1
viscous unstable
Rayleigh line
Ω_2

Fig. 1.3 Taylor's viscous stability criterion - blue line.

After Taylor's ground-breaking work, there has been much research in the Taylor-Couette flow (TCF). The system is known to show an incredibly complex set of patterns depending on the rotation rates of the inner and outer cylinders, for example, see the experimental studies by Coles [9] and Andereck et al. [1] and a recent review by Grossmann et al. [15]. With the increase in the computational power and popularization of spectral methods by Orszag [31], many Direct Numerical Simulation (DNS) studies were carried out on the incompressible TCF. Marcus [27] conducted one of the first DNS studies of TCF based on spectral methods. More recently, Shi et al. [35] have studied the problem with a highly efficient, parallel solver. Figure 1.4, taken from Andereck et al. [1], shows different regimes of flow patterns.

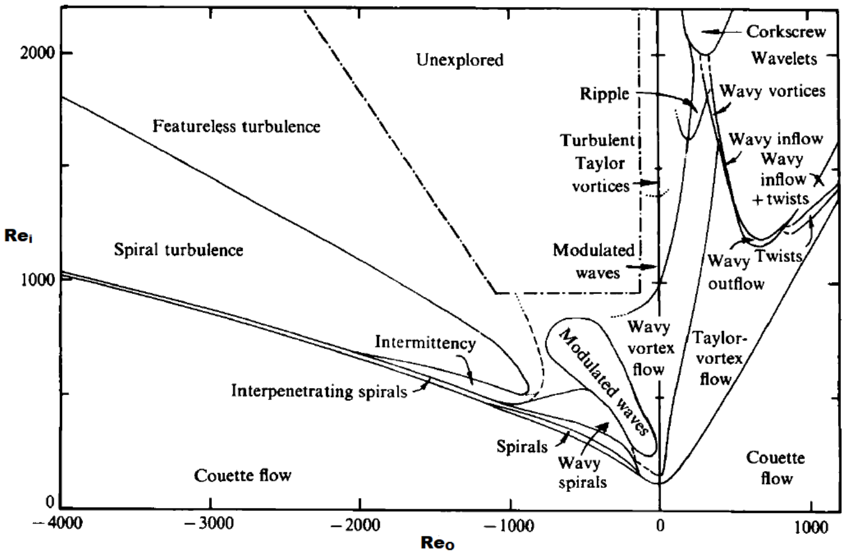

Fig. 1.4 Phase plane of the Newtonian, incompressible Taylor-Couette setup. Taken from Andereck et al. [1]. Here $Re_i = \Omega_i R_i d/\nu$ and $Re_o = \Omega_o R_o d/\nu$ represent Reynolds number based on inner and outer cylinder velocities $\Omega_i R_i$ and $\Omega_o R_o$, respectively. Ω_i and Ω_o are angular velocities of inner and outer cylinders, respectively. d is the gap width $R_o - R_i$ and ν is the kinematic viscosity of the fluid.

1.2 Why Study Taylor-Couette flow?

Perhaps the most important reason to study Taylor-Couette flow is its geometric simplicity, making it practical for experimental investigations. The setup has been used as a test to check validity of theoretical descriptions in the past and it still remains popular. Also, it has proven useful to study accretion disks in astrophysical flows, see Grossmann et al. [15]. It is interesting to see if the origin turbulence in accretion disks has purely hydrodynamic origins or does it require some other mechanism such as the magnetorotational instability (MRI), first seen by Velikhov [40] and later generalized by Chandrasekhar [5] and Balbus and Hawley [2]. In this thesis, we study the pattern formation in the Taylor-Couette setup for a compressible gas, a relatively unexplored area.

1.3 Previous Work on the Compressible TCF

A lot of work has been done in the area of incompressible Taylor-Couette flow, for example, see Chandrasekhar [6], DiPrima and Swinney [12] and Grossmann et al. [15]. However, not much work, be it theoretical, experimental or numerical, has been done on its compressible counterpart.

Kuhlthau [21] conducted an experimental study on the compressible Taylor-Couette problem with dry air as the compressible fluid. In these experiments, the peripheral Mach number ($Ma = \Omega_i R_i/(\gamma R T_i)^{1/2}$, where Ω_i is the angular velocity and R_i is the radius of the inner cylinder, T_i is the temperature maintained at the inner cylinder wall, $\gamma = c_{p/c_v}$ is the ratio of heat capacities and R is the universal gas constant) was kept constant while the average density was increased, thereby decreasing the Knudsen number ($Kn \propto \frac{Ma}{Re}$ and $Re \propto$ average density $\Rightarrow$ $Kn \propto$ (1/average density)). Experiments were done for the values of peripheral Ma such that $0.7 \lesssim Ma \lesssim 15$. The critical Kn was found to increase with increasing Ma. However, the critical Reynolds number ($Re_{1c} \sim Ma/Kn$) was found to be almost the same as its incompressible counterpart.

Kao and Chow [20] assumed axisymmetric disturbances and carried out a linear stability analysis for the compressible Taylor-Couette flow with radius ratio $\eta = \frac{R_1}{R_2} = 0.5$. Their results apparently implied that increasing Mach number (Ma) destabilized the flow. In other words, the critical inner Reynolds number (Re_1) decreased in comparison to the incompressible case when Ma was increased. Hatay et al. [18] considered the linear stability problem for a wide range of parameters and found out that increasing Ma stabilizes the flow for narrow gaps ($\eta > 0.8$) and destabilizes for wide gaps. Hence, their results agreed with Kao and Chow [20]. Both Kao and Chow [20] and Hatay et al. [18] defined the Reynolds number based on the local density. As Manela and Frankel [26] correctly pointed out, the local density cannot be *a priori* prescribed in numerics or experiments. Also, because of large supersonic speeds, variation between local and average densities can be quite large. Hence, using the critical Re_1 based on the local density is not a good measure when comparing with its incompressible counterpart. For this reason, the stabilizing or destabilizing effect of increasing Ma might not be unequivocal.

Manela and Frankel [26] focused on narrow-gaps, conducted a linear stability analysis and concluded that increasing Ma stabilizes the flow. Following Manela and Frankel [26], Welsh et al. [41] carried out the linear stability analysis for the Taylor-Couette flow for a wide-gap case, with radiaus ratio $\eta = \frac{R_1}{R_2} = 0.5$. At high Prandtl numbers (Pr), they found new instability modes that become unstable to oscillatory axisymmetric modes at the onset. They also found that the onset of instability can occur even when the angular momentum **increases** outwards. Hence the notable finding is that the classical Rayleigh criterion can be violated in the compressible Taylor-Couette case.

1.4 Outline of the thesis

Chapter 2 focuses on the mathematical formulation of the problem, development of a numerical code to solve axisymmetric, compressible Navier-Stokes equations in cylindrical geometry as well as code validation.

Chapter 3 begins with writing dimensionless equations and boundary conditions for the Taylor-Couette flow. Characteristic scales for non-dimentionalization are so chosen that numerical results can be compared with experiments (see Welsh et al. [41]). Another verification of the code is presented by matching the analytically known base state of the compressible TCF with the one obtained from long-time marching of the compressible Navier-Stokes equations. The effect of variable viscosity on the onset of Taylor vortex flow (TVF) is investigated. At higher Re_1, an interesting behavior is uncovered. When axisymmetry is imposed, Taylor vortex flow is seen to bifurcate to an axisymmetric wave traveling in the negative z direction. Average kinetic energies based on radial and axial velocities are plotted which show oscillations in time. A fast Fourier transform (FFT) is done to extract the dominant frequencies and the same procedure is repeated over a range of Re_1. Extracted dominant frequencies are plotted against Re_1 to see the effect of increasing Reynolds number.

Chapter 4 is devoted to studying the finite-size effects and anomalous modes in the compressible Taylor-Couette flow. The effect of variation in the aspect ratio at a constant Re_1 is also studied. Evidence for hysteresis is presented by plotting kinetic energy versus time. The implications of this work and possible future directions are discussed briefly in the final chapter.

Chapter 2

Numerical Implementation and Code Validation

"A computation is a temptation that should be resisted as long as possible." - J.P. Boyd

2.1 Introduction and Governing Equations

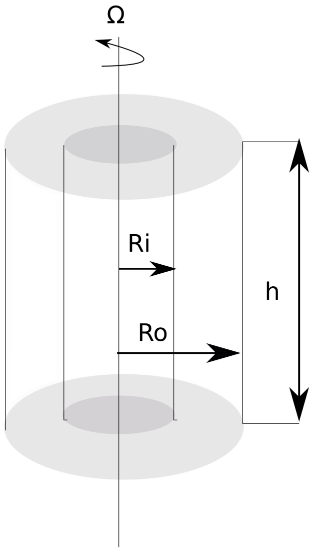

Fig. 2.1 Domain.

In this chapter, a numerical code is developed to solve the compressible Navier-Stokes equations in cylindrical geometry. To validate the code, we compare our results with Harada [17]. A

Taylor-Couette-type setup as shown in Fig. 2.1 is used where both the cylinders are rotating at the same angular velocity Ω. The initial condition is that of a solid body rotation for the annular gas as in the work of Harada [17]. We wish to investigate two problems to validate the code:

- “Thermally driven flow”: a vertical temperature gradient is imposed suddenly, see Fig. 2.2a

- “Mechanically driven flow”: the inner and bottom plates are stopped suddenly, see Fig. 2.2b

Accordingly, the boundary conditions are marked as shown in Fig. 2.2.

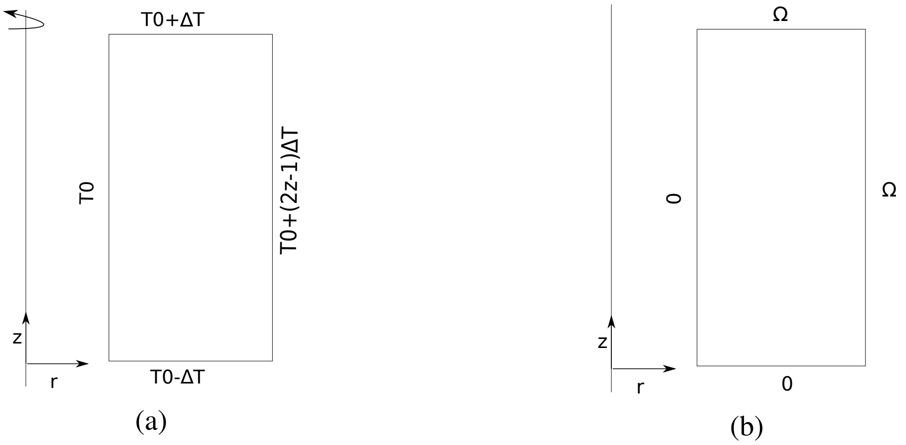

(a) (b)

Fig. 2.2 Boundary conditions: (a) Thermally driven flow and (b) Mechanically driven flow.

2.1.1 Governing Equations and Boundary Conditions

The governing equations are written in the rotating frame of reference, rotating with Ω with respect to the rest frame. The characteristic quantities are defined in table 2.1.

Dimensional Quantity	Characteristic Quantity
t_R^*	Ω^{-1}
L_R^*	R_0
U_R^*	ΩR_0
ρ_R^*	ρ_0
T_R^*	T_0
p_R^*	$(c_p - c_v)\rho_0 T_0$

Table 2.1 Characteristic quantities

Here R_0 is the radius of the outer boundary, Ω is the initial angular velocity of the system, ρ_0 and T_0 are initial density and temperature at the outer wall. The velocities in the r, ϕ and z directions are denoted by u, v, and w, respectively. The dimensionless governing equations can be written as follows.

$$\frac{\mathscr{D}\rho}{\mathscr{D}t} = 0, \tag{2.1}$$

$$\frac{\mathscr{D}(\rho u)}{\mathscr{D}t} - \rho r - \rho v\left(2 + \frac{v}{r}\right) = -\frac{1}{\gamma M^2}\frac{\partial p}{\partial r} + E\left(\mathscr{L}u + \frac{1}{3}\frac{\partial Q}{\partial r}\right) \tag{2.2}$$

$$\frac{\mathscr{D}(\rho v)}{\mathscr{D}t} + \rho u\left(2 + \frac{v}{r}\right) = E\mathscr{L}v \tag{2.3}$$

$$\frac{\mathscr{D}(\rho w)}{\mathscr{D}t} = -\frac{1}{\gamma M^2}\frac{\partial p}{\partial z} + E\left(\nabla^2 w + \frac{1}{3}\frac{\partial Q}{\partial z}\right) \tag{2.4}$$

$$\frac{\mathscr{D}(\rho T)}{\mathscr{D}t} + (\gamma - 1)\rho T Q = -\frac{\gamma E}{Pr}\nabla^2 T + (\gamma - 1)\gamma M^2 E\Phi \tag{2.5}$$

$$p = \rho T \tag{2.6}$$

where

$$\frac{\mathscr{D}}{\mathscr{D}t} = \frac{\partial}{\partial t} + \nabla.[()q],$$

$$q = (u, v, w),$$

$$\nabla^2 = \frac{\partial^2}{\partial r^2} + \frac{1}{r}\frac{\partial}{\partial r} + \frac{\partial^2}{\partial z^2},$$

$$\mathscr{L} = \nabla^2 - \frac{1}{r^2},$$

$$Q = \frac{1}{r}\frac{\partial (ru)}{\partial r} + \frac{\partial w}{\partial z},$$

$$\Phi = 2\left[\left(\frac{\partial u}{\partial r}\right)^2 + \left(\frac{u}{r}\right)^2 + \left(\frac{\partial w}{\partial z}\right)^2\right] + \left(\frac{\partial v}{\partial r} - \frac{v}{r}\right)^2 + \left(\frac{\partial v}{\partial z}\right)^2 + \left(\frac{\partial w}{\partial r} + \frac{\partial u}{\partial z}\right)^2 - \frac{2}{3}Q^2.$$

The Ekman Number is defined via

$$E \equiv \frac{(\mu/\rho_0)}{\Omega R_0^2},$$

the peripheral Mach number is

$$M \equiv \frac{\Omega R_0}{(\gamma R T)^{\frac{1}{2}}},$$

and the Prandtl number is

$$Pr \equiv \mu C_p/\kappa.$$

Here μ is the shear viscosity, κ is the thermal conductivity, C_p and C_v are specific heats at constant pressure and volume, respectively. Ω is the angular velocity with which both the cylinders are rotating initially. The initial condition in both thermally and mechanically driven flows is that of a solid body rotation. In non-dimensional parameters, the initial conditions are given as follows:

$$u = v = w = 0, \tag{2.7}$$

$$T = 1, \tag{2.8}$$

$$\rho_e = exp[(1/2)\gamma M^2(r^2 - 1)]. \tag{2.9}$$

Finally, the boundary conditions in non-dimensional form read as:

1. Thermally Driven Flow
    - $u = v = w = 0$ at all boundaries
    - $T = 1 - \varepsilon$ at $z = 0$
    - $T = 1 + \varepsilon$ at $z = \Lambda = h/R_o$
    - $T = 1 + \varepsilon(2z/\Lambda - 1)$ at $r = R_o$
    - $T = 1$ at $r = R_i$
2. Mechanically Driven Flow
    - $u = w = 0$ at all boundaries
    - $T = 1$ at all boundaries
    - $v = 0$ at $r = R_o$ and $z = \Lambda = h/R_o$
    - $v = -r$ at $z = 0$
    - $v = -r_a$ at $r = R_i$

where $\varepsilon = \Delta T/T_0$, $R_i = 0.3$, $R_o = 1.0$, $\Lambda = h/R_o = 1.0$

2.2 Numerical Method and its Implementation

A variant of the numerical method used in Harada[17, 16] and Hyun and Park [19] is developed. The details of the numerical implementation are described below.

A finite difference method is developed based on the conservation laws. Primitive variables are used to write down the governing equations and appropriate boundary conditions. For numerical simplicity, the equations are written for a torus of volume $(2\pi)rdrdz$. Writing equations this way amounts to multiplying the governing equations by r throughout. As the numerical method is developed in the upcoming sections, the usefulness of this move will become evident later. Essentially, if we define a new variable $\bar{\rho} = \rho r$ and write the governing equations is terms of $\bar{\rho}$ instead of ρ, the convective derivatives in the cylindrical coordinates look as if they were written in a Cartesian coordinate system.

As we are developing a scheme for the axisymmetric solutions, we use a two-dimensional ($2d$), uniform, staggered grid. The choice of staggered grid is motivated by the physics of the problem. We do not, in general, have boundary conditions for density and pressure. So to avoid creating artificial boundary conditions in order to make the problem **well-posed**, we push the calculation of density and pressure fields **inside** the domain. Hence, no artificial density or pressure boundary conditions are required. This choice also ensures local mass conservation in a given cell, Harada[17, 16] and Hyun and Park [19].

To approximate first-order derivatives in space, we employ the familiar **central difference method**. For convective derivatives, we use **the upwind scheme or the donor-cell method**. Finally, for diffusion terms and time stepping, we use **a leapfrog type DuFort-Frankel method.**

2.3 Developing Finite Difference Approximation

2.3.1 The Finite Difference Approximation

We multiply the governing equations (2.1)-(2.6) by r throughout and write them in terms of a new variable

$$\bar{\rho} = \rho r. \tag{2.10}$$

$$\frac{\mathscr{D}\bar{\rho}}{\mathscr{D}t} = 0, \tag{2.11}$$

$$\frac{\mathscr{D}(\bar{\rho}u)}{\mathscr{D}t} - \bar{\rho}r - \bar{\rho}v\left(2+\frac{v}{r}\right) = -r\frac{1}{\gamma M^2}\frac{\partial p}{\partial r} + Er\left(\mathscr{L}u + \frac{1}{3}\frac{\partial Q}{\partial r}\right) \tag{2.12}$$

$$\frac{\mathscr{D}(\bar{\rho}v)}{\mathscr{D}t} + \bar{\rho}u\left(2+\frac{v}{r}\right) = Er\mathscr{L}v \tag{2.13}$$

$$\frac{\mathscr{D}(\bar{\rho}w)}{\mathscr{D}t} = -r\frac{1}{\gamma M^2}\frac{\partial p}{\partial z} + Er\left(\nabla^2 w + \frac{1}{3}\frac{\partial Q}{\partial z}\right) \tag{2.14}$$

$$\frac{\mathscr{D}(\bar{\rho}T)}{\mathscr{D}t} + (\gamma-1)\bar{\rho}TQ = -\frac{\gamma Er}{Pr}\nabla^2 T + r(\gamma-1)\gamma M^2 E\Phi \tag{2.15}$$

$$p = \bar{\rho}T/r \tag{2.16}$$

The finite difference approximation can be written down easily. As mentioned in the introduction, we use **central difference method** for first derivatives in space. For convective derivatives, we use **upwind scheme or donor-cell method**. Finally, for diffusion terms and time stepping, we use **a leapfrog type DuFort-Frankel method.** The discretized version of Eqs. (2.11)-(2.16) can be written as follows:

$$(\bar{\rho}^{n+1}-\bar{\rho}^{n-1})/2\Delta t = -[\delta_r(\bar{\rho}u)^{n+1}+\delta_z(\bar{\rho}w)^{n+1}], \tag{2.17}$$

$$\begin{aligned}((\bar{\rho}u)^{n+1}-(\bar{\rho}u)^{n-1})/2\Delta t = -[\delta_r(u\bar{\rho}u)^n+\delta_z(w\bar{\rho}u)^n]+\left[\bar{\rho}\left(r+v\left(2+\frac{v}{r}\right)\right)\right]^n-\frac{1}{\gamma M^2}r\delta_r p^n \\ +Er\left[\frac{4}{3}\left(\delta_r\delta_r u^n+\delta_r\left(\frac{u}{r}\right)\right)+\delta_z\delta_z u^n+\frac{1}{3}\delta_r\delta_z w^n\right],\end{aligned} \tag{2.18}$$

$$\begin{aligned}((\bar{\rho}v)^{n+1}-(\bar{\rho}v)^{n-1})/2\Delta t = -[\delta_r(u\bar{\rho}v)^n+\delta_z(w\bar{\rho}v)^n]+\left[\bar{\rho}u\left(2+\frac{v}{r}\right)\right]^n \\ +Er\left[\left(\delta_r\delta_r v^n+\delta_r\left(\frac{v}{r}\right)\right)+\delta_z\delta_z v^n\right],\end{aligned} \tag{2.19}$$

$$\begin{aligned}((\bar{\rho}w)^{n+1}-(\bar{\rho}w)^{n-1})/2\Delta t = -[\delta_r(u\bar{\rho}w)^n+\delta_z(w\bar{\rho}w)^n]-\frac{1}{\gamma M^2}r\delta_z p^n \\ +Er\left[\delta_r\delta_r w^n+\frac{1}{r}\delta_r w^n+\frac{4}{3}\delta_z\delta_z w^n+\frac{1}{3}\delta_z\delta_r u^n+\frac{1}{3}\delta_z\left(\frac{u^n}{r}\right)\right],\end{aligned} \tag{2.20}$$

$$\begin{aligned}((\bar{\rho}T)^{n+1}-(\bar{\rho}T)^{n-1})/2\Delta t = -[\delta_r(\bar{\rho}u)^{n+1}T^n+\delta_z(\bar{\rho}w)^{n+1}T^n]-(\gamma-1)(\bar{\rho}T)^{n+1}Q^n+ \\ \frac{\gamma E}{Pr}r\left[\delta_r\delta_r T^n+\frac{1}{r}\delta_r T^n+\delta_z\delta_z T^n\right]+(\gamma-1)\gamma M^2 Er\Phi^n,\end{aligned} \tag{2.21}$$

$$p^{n+1}=(\bar{\rho}T)^{n+1}/r, \tag{2.22}$$

where

$$\Phi^n = \mu(\rho,T)\left[2e_{ij}e_{ij} - \frac{2}{3}(\nabla\cdot\underline{u})^2\right]$$
$$= \mu\left\{\left[2(\delta_r u^n)^2 + \frac{2}{r^2}(u^n)^2 + 2(\delta_z w^n)^2 + (\delta_r v^n - v^n/r)^2 + (\delta_z u^n + \delta_r w^n)^2 + (\delta_z v^n)^2\right] - \frac{2}{3}(Q^n)^2\right\}, \tag{2.23a}$$

$$Q^n = (\nabla.\underline{\mathrm{u}})^n = (1/r)(\delta_r(ru^n)) + \delta_z w^n. \tag{2.23b}$$

In equations (2.17)-(2.22), we used the following notation

$$\delta_x\phi_i = \phi_{(i+\frac{1}{2})} - \phi_{(i-\frac{1}{2})}/\Delta x_i. \tag{2.24}$$

We use Dufort-Frankel method to approximate the second derivatives, i.e.,

$$\delta_x\delta_x\phi_i = [(\phi_{(i+1)} - \bar{\phi}_i)/\Delta x_{i+\frac{1}{2}} - (\bar{\phi}_i - \phi_{(i-1)})/\Delta x_{i-\frac{1}{2}}]^n/\Delta x_i, \tag{2.25}$$

where

$$\bar{\phi}_i{}^n = \frac{1}{2}(\phi_i^{n+1} - \phi_i^n),$$
$$\Delta x_{i+\frac{1}{2}} = (\Delta x_i + \Delta x_{i+1})/2,$$

and

$$\Delta x_i = (\Delta x_{i+\frac{1}{2}} + \Delta x_{i-\frac{1}{2}})/2.$$

Since we are going to use uniform grid, we have

$$\Delta x_{i+\frac{1}{2}} = \Delta x_{i-\frac{1}{2}} = \Delta x_i$$

From Eqns.(2.17)-(2.25) although it appears as if we are using an implicit method, since ϕ_i^{n+1} is on the right hand side, the truth is far from it. We can easily rearrange the terms and take this term from future to left hand side to make the scheme explicit. Therefore, while coding, we only calculate a part of any second derivative.

2.3.2 Donor Cell or Upwind Scheme for Convective Derivatives

We now describe the “donor cell” or “upwind scheme” used to approximate the convective derivative terms. We take a one dimensional example for this purpose. Let ϕ be any scalar quantity, being advected by the velocity u. Then the convective derivative $\frac{\partial(u\phi)}{\partial x}$ at a particular node , say at i can be calculated according to the velocity u at the cell boundaries which are at $i+\frac{1}{2}$ and $i-\frac{1}{2}$. Depending on the signs of the neighboring velocities, there are four possible cases. Figure 2.3 highlights these cases.

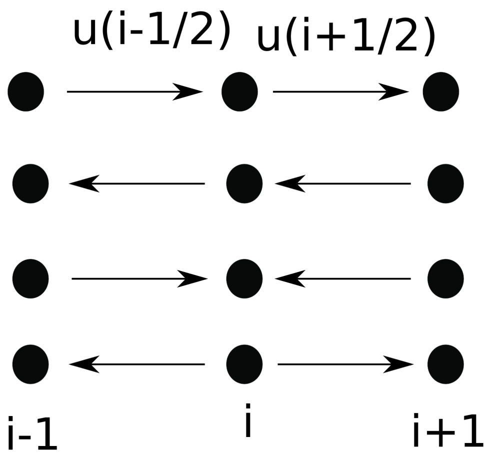

Fig. 2.3 Four possible cases for upwind scheme.

1. If $u_{(i-\frac{1}{2})} \geqslant 0, u_{(i+\frac{1}{2})} \geqslant 0$,

$$\frac{\partial(u\phi)}{\partial x} = \frac{u_{(i+\frac{1}{2})}\phi_i - u_{(i-\frac{1}{2})}\phi_{i-1}}{\Delta x}. \tag{2.26}$$

2. If $u_{(i-\frac{1}{2})} \leqslant 0, u_{(i+\frac{1}{2})} \leqslant 0$,

$$\frac{\partial(u\phi)}{\partial x} = \frac{u_{(i+\frac{1}{2})}\phi_{i+1} - u_{(i-\frac{1}{2})}\phi_i}{\Delta x}. \tag{2.27}$$

3. If $u_{(i-\frac{1}{2})} \geqslant 0, u_{(i+\frac{1}{2})} \leqslant 0$,

$$\frac{\partial(u\phi)}{\partial x} = \frac{u_{(i+\frac{1}{2})}\phi_{i+1} - u_{(i-\frac{1}{2})}\phi_{i-1}}{\Delta x}. \tag{2.28}$$

4. If $u_{(i-\frac{1}{2})} \leqslant 0, u_{(i+\frac{1}{2})} \geqslant 0$,

$$\frac{\partial(u\phi)}{\partial x} = \frac{u_{(i+\frac{1}{2})}\phi_i - u_{(i-\frac{1}{2})}\phi_i}{\Delta x} \tag{2.29}$$

This method is applied to calculate the following derivatives: $\delta_r(u\bar{\rho}u), \delta_r(u\bar{\rho}v), \delta_r(u\bar{\rho}w), \delta_z(w\bar{\rho}u), \delta_z(w\bar{\rho}v)$ and $\delta_z(w\bar{\rho}w)$. One of the important reasons to choose this method is that it **respects local mass conservation**, Harada[17, 16] and Hyun and Park [19].

2.3.3 Caveats While Using the DuFort-Frankel Leapfrog Type Scheme

To calculate the second derivatives (diffusion terms), we use a DuFort-Frankel leapfrog type scheme. The scheme is as follows: To approximate diffusion terms, we use (2.24). As for the time derivative, we use the following second order scheme

$$\frac{du}{dt} = \frac{u^{n+1} - u^{n-1}}{2\delta t} \tag{2.30}$$

We can see that there is a slight problem. We need **two initial conditions.** If we somehow get u^0 and u^1, we can update for u^2. However, we only know the physical initial condition u^0. In literature, the second initial condition is referred to as the **computational initial condition**. Now the pertinent question is, **how to get u^1?** Let us take a concrete example of the oscillation equation and see how and why computational mode can cause problems.

Leapfrog Scheme for the Oscillation Equation

Let us consider the following equation:

$$\frac{du}{dt} = i\omega u \tag{2.31}$$

where i is the square root of -1 and ω is a real number. Let us define A, the amplification factor, as follows:

$$u^{n+1} = Au^n \tag{2.32}$$

Now if we write a leapfrog scheme for the oscillation equation above, we will have

$$u^{n+1} - u^{n-1} = 2\Delta t i\omega u \tag{2.33}$$

Let us first consider a simpler sub-case of $\omega = 0$

Case 1

Here, the leapfrog scheme takes the following form.

$$u^{n+1} - u^{n-1} = 0 \tag{2.34}$$

Which is, of course, the exact solution. It is worthy of notice here, that all the values of u at even time steps will be governed by the physical initial condition. While all the odd ones, will be governed by $u(n=1)$. If we make the choice $u(n=1) \neq u(n=0)$, we will have oscillations(u^0, u^1, u^0, u^1..., these are clearly not physical, for we have set $\omega = 0$). On the other hand, if we choose $u^1 = u^0$, we get the exact solution without oscillations. This example illustrates how important the choice of the computational initial condition is.

Case 2

Here, let ω be some positive real number. Eqn.(2.33) can be rearranged as

$$u^{n+1} - 2\Delta t i \omega u^n - u^{n-1} = 0 \tag{2.35}$$

Putting (2.32) in (2.35), we have

$$A^2 - 2\Delta t i \omega A - 1 = 0 \tag{2.36}$$

We can now see that this quadratic equation has two possible roots for A: $A_{\pm} = i\omega\Delta t \pm \sqrt{1-(\omega\Delta t)^2}$ Therefore, we see that there are two **'modes'**.

$$u_{\pm}^{n+1} = A_{\pm} u^n \tag{2.37}$$

Since we had a first order differential equation in time, we must only have one solution. So one of these solutions has nothing to do with the physics of the problem. It is just an artifact of the scheme that we have been using. Consider the limit $\omega \to 0$, for which it is easy to see that $A_+ \to +1$ while $A_- \to -1$ There are a few things to notice here.

- the origin of the computational mode has nothing to do with the physics of the problem. It is an artifact of the leapfrog scheme.
- as $\Delta t \to 0$, $u_-^{n+1} \nrightarrow u_-^n$,i.e., making the time step smaller won't make the computational mode go away.
- after n steps, the general solution will be a combination of both the modes, i.e. $u^n = au_+^n + bu_-^n$ or $\Rightarrow u^n = A_+^n au^0 + A_-^n bu^0$

2.3.4 The Remedy: Filtering

Now the pertinent question is, how to get rid of the computational mode? In simple problems, like the oscillation equation above, we can choose the initial condition in such a way that the coefficient of the computational mode goes to zero. But in general cases, like compressible Navier-Stokes equations, we cannot do so. If we cannot get rid of the computational mode, what should we do? One of the possible remedies is, restarting the code after every few steps. Another possible approach is to smooth out the solution after every few time steps. This is known as time filtering. We 'filter' out the computational mode by some mechanism. In the present numerical calculation, we simply put $u^1 = u^0$. After every certain number of time steps, (20 or 30), we **filter** the solution in order to suppress the computational mode. The filtering is done by the following simple formula, see Harada[17, 16] and Hyun and Park [19].

$$\phi^{n\pm\frac{1}{2}} = \frac{1}{2}(\phi^n + \phi^{n\pm1}) \tag{2.38}$$

2.4 Putting It All Together

Once we have discretized the governing equations according to the last section, the numerical implementation involves solving them in the following manner.

1. In the present numerical calculation, we simply put $\phi^1 = \phi^0$, where ϕ can be $u, v, w, \bar{\rho}, T, p$.

2. Solve for $(\bar{\rho}u)^{n+1}$, $(\bar{\rho}v)^{n+1}$, $(\bar{\rho}w)^{n+1}$ from momentum equations (2.18)-(2.20).

3. Get $\bar{\rho}^{n+1}$ by plugging in the updated velocity fields obtained from the previous step into the continuity equation (2.17).

4. Get $(\bar{\rho}T)^{n+1}$ from the energy equation (2.21).

5. Update pressure p^{n+1} from the equation of state (2.22).

6. Obtain u^{n+1}, v^{n+1}, w^{n+1}, T^{n+1} by dividing $(\bar{\rho}u)^{n+1}$, $(\bar{\rho}v)^{n+1}$, $(\bar{\rho}w)^{n+1}$, $(\bar{\rho}T)^{n+1}$ by $\bar{\rho}^{n+1}$.

7. To avoid computational splitting caused by leapfrogging, filter after every m time steps according to Eq. (2.38).

8. Keep going until the steady state is reached. We monitor whether the kinetic energy curves have saturated to check if the steady state has been reached. Figure 2.4 shows KE_u and KE_w (as defined in Harada [17] and Section 3.6.1) versus time plots. The saturation of kinetic energies is evident from Fig. 2.4.

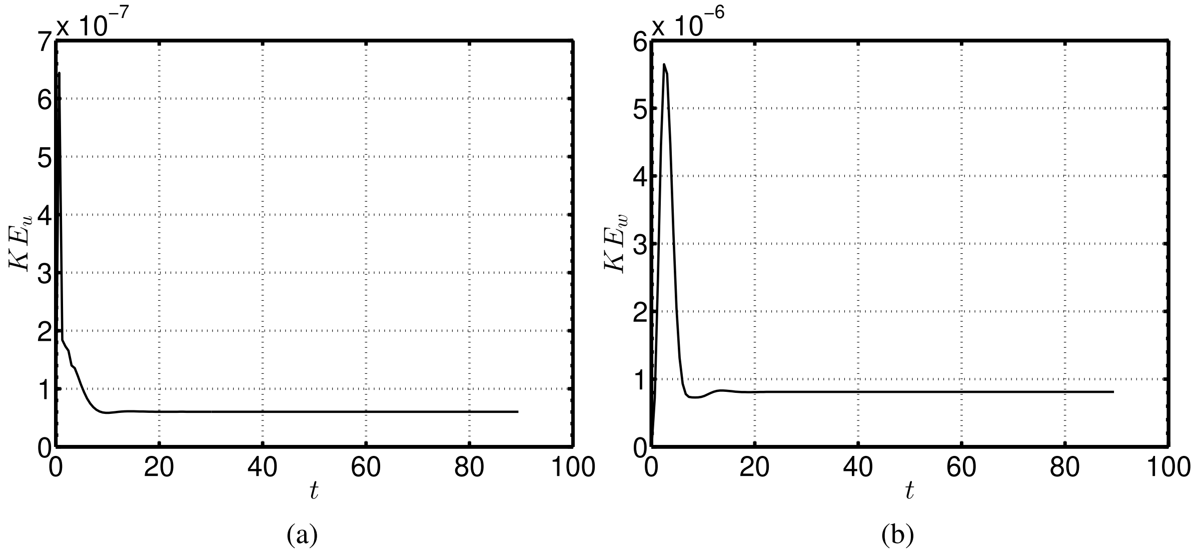

Fig. 2.4 Time series for kinetic energies, case 2 from Table - 2.2: (a) KE_u, (b) KE_w.

2.5 Physical Interpretation of Results

"Never make a calculation until you know the answer. Make an estimate before every calculation, try a simple physical argument..." - John Wheeler.

In this section, we present some physical arguments on how the flow ought to look like, in the cases of thermally and mechanically driven flows. The initial condition is the solid body rotation, where in the interior, pressure gradient in the radial direction is balanced by the centrifugal force. The development of the flow starts by different mechanisms in the thermally and mechanically driven flows. Let us try to understand how the flow would start to develop in each of these cases. Table -2.2 summarizes the details of each of the cases studied.

Case	Mach number (M)	Details
1	3.0	Thermally driven flow
2	4.0	Thermally driven flow
3	4.0	Mechanically driven flow, with viscous dissipation
4	4.0	Mechanically driven flow, without viscous dissipation

Table 2.2 Cases from Harada [17].

Other parameters are as follows. $E = 1.03 \times 10^{-3}$ (Ekman number), $Pr = 0.97$ (Prandtl number), $M = 4.0$ (Peripheral Mach number) and $\varepsilon = 3.125 \times 10^{-2} = \Delta T / T_0$ (Thermal Rossby number).

2.5.1 Thermally Driven Flow

The gas is rotating in a solid body rotation in the annulus. We have the balance of radial forces in non-dimensional terms given by:

$$|\frac{1}{\gamma M^2}\frac{\delta p}{\delta r}| = |\rho r|,$$

as shown in the upper part of Fig. 2.5. Suddenly, we lower the temperature of the bottom plate from 1 to $1-\varepsilon$ and raise the temperature of the upper plate from 1 to $1+\varepsilon$. This way, we introduce a temperature gradient in the system. We also assume that the outer wall is thermally conducting and it immediately establishes a linear temperature profile where temperature varies from $1-\varepsilon$ to $1+\varepsilon$ with the vertical height z. Now in the lower-right corner, we will have the heaviest fluid while in the upper-left corner (because most of it will have been pushed outwards by the centrifugal force), we have the lightest fluid blob (because density is a function of temperature). Therefore, in non-dimensional terms,

$$|\frac{1}{\gamma M^2}\frac{\delta p}{\delta r}| < |\rho_{New} r|.$$

where ρ_{New} is the new local density in the lower-right corner, which will be greater than ρ the original density because the temperature near the wall has been lowered. The balance of forces is no more valid, for in the lower-right corner in the $r-z$ plane, the centrifugal force on the blob of the gas will be higher than the radial pressure gradient, (because the density will be more), as shown in Fig. 2.5.

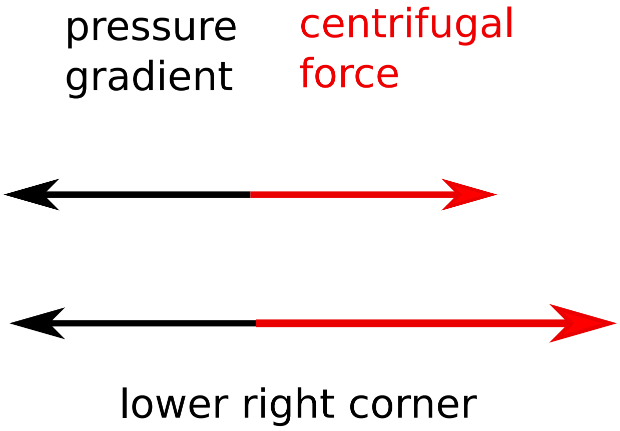

Fig. 2.5 Thermally driven flow.

In other words, the radial pressure gradient will not be able to balance the centrifugal force and the blob will have a tendency to go radially outwards. As it is physically impossible because of the presence of the outer side wall, the blob has nowhere to go but upwards. Similarly, near the upper-left corner, centrifugal force won't be enough to balance the pressure gradient and the lighter blob will have a tendency to go inwards. But because of a solid wall, it will have no choice but to go downwards, which is where it will go. The inner core flow will be set up due to the continuity of the gas. As soon as the gas starts to move, the Coriolis force will try to push it outside the $r-z$ plane. Now by symmetry, the flow at the mid-height $z=\Lambda/2$ will be purely axial and the Coriolis force will be zero there. Thus we will get symmetric azimuthal velocities. This way, we can explain how the flow starts and its qualitative behavior, which is in agreement with the numerical results. The velocity plot for the thermally driven flow, case 2 of Harada [17], is shown in Fig. 2.6.

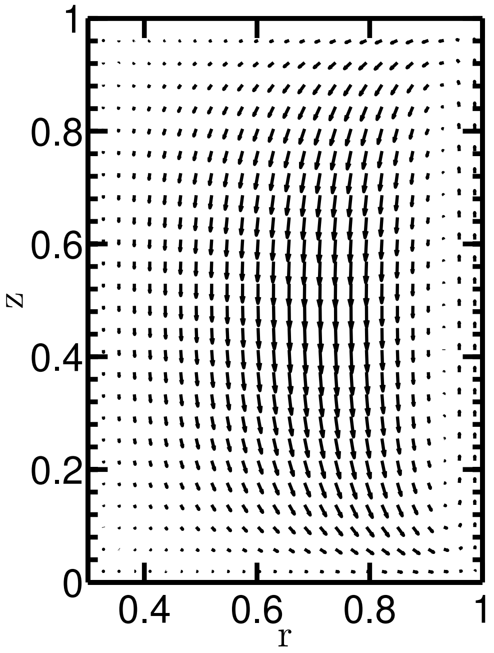

Fig. 2.6 Velocity vector plot for thermally driven flow, case 2 (Table - 2.2).

2.5.2 Mechanically Driven Flow

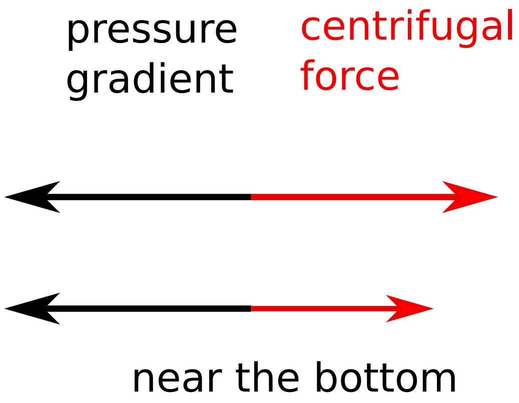

Fig. 2.7 Mechanically driven flow.

As we stop the inner and the bottom plate from the state of solid body rotation, we will have a case similar to the classical case of spin-down. For example, see Greenspan and Howard [14] for a study of the classical linear spin-down of a rapidly rotating fluid in an axisymmetric container with rigid boundaries, followed by an instantaneous small change in the angular velocity of the boundary at small Ekman number. The gas near the bottom wall will slow down, owing to viscosity or in other words, the no-slip boundary condition. The negative pressure gradient, which was balancing the centrifugal force in the solid body rotation, will now take over, as shown in Fig. 2.7. This will happen because the centrifugal force will no longer be able to balance the pressure gradient. The gas will start flowing radially inwards, towards the axis of rotation. From then on, the Coriolis force will try to push it out of the plane. The flow will be set-up this way and mass conservation will drive the flow. The velocity plots for cases 3 and 4 from Harada [17])(table - 2.2) are given in Fig. 2.8:

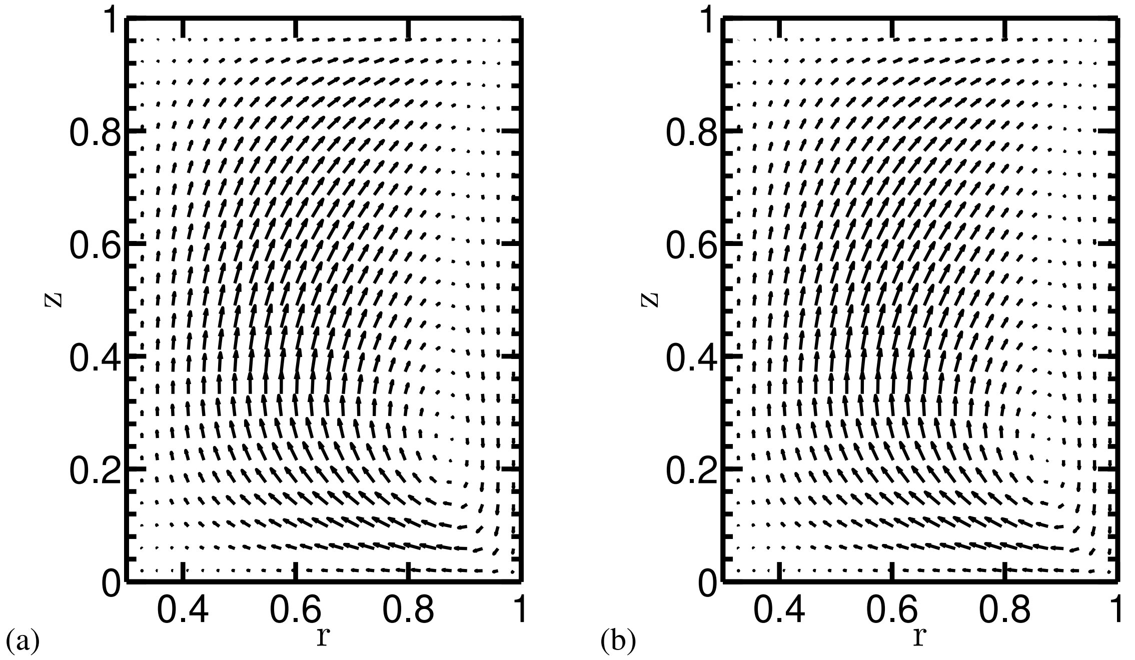

Fig. 2.8 Mechanically driven flow: velocity vector plots for (a) case 3 and (b) case 4 (Table - 2.2).

2.6 Thermally Driven Flow - Code Validation

In this subsection, we consider Case 2 from Harada [17] to validate the present code, (Table - 2.2). The parameters are taken as $E = 1.03 \times 10^{-3}$ (Ekman number), $Pr = 0.97$ (Prandtl number), $M = 4.0$ (Peripheral Mach number) and $\varepsilon = 3.125 \times 10^{-2} = \Delta T / T_0$ (Thermal Rossby number).

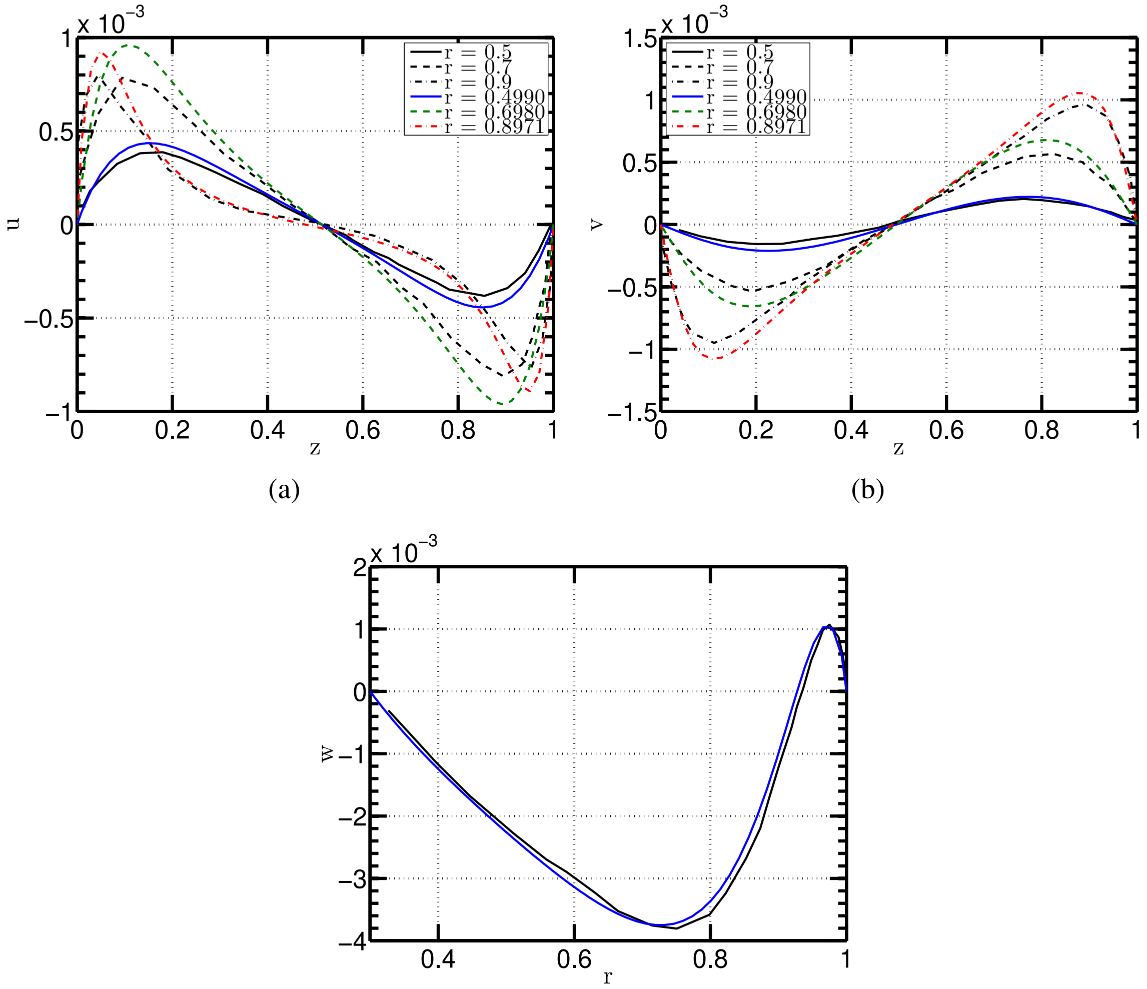

(a) (b)

(c)

Fig. 2.9 Profiles in black are from Harada [17], colored ones are from the present code (a) u vs z at different r, (b) v vs z at different r, (c) w vs r at $z = 0.5$.

Figure 2.9 shows axial and radial profiles of different velocity components for thermally driven flow. In Fig. 2.9a, the extracted values of Harada [17] are multiplied by 10; it is probably a printing mistake in the paper. Overall, there is a good agreement.

Temperature and azimuthal velocity contours are also plotted in Fig. 2.10 and 2.11, with good agreement of present solution with those of Harada [17].

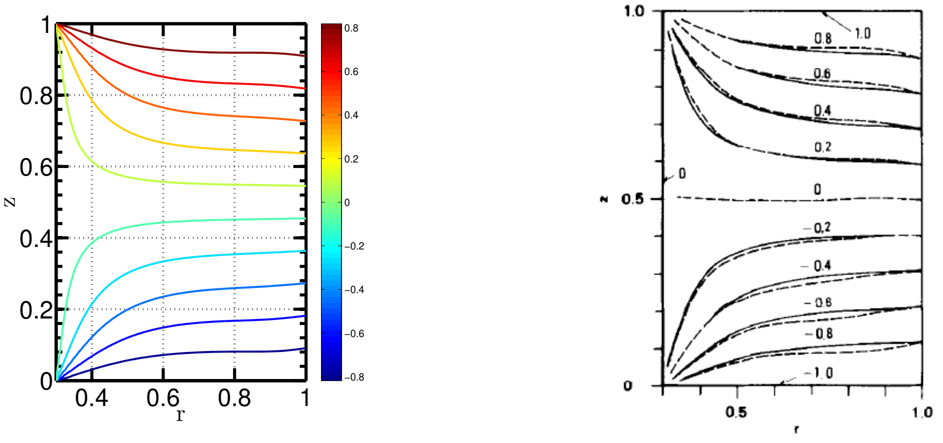

(a)

(b)

Fig. 2.10 Temperature contours, case 2, (Table - 2.2) (a) present code and (b) Harada [17].

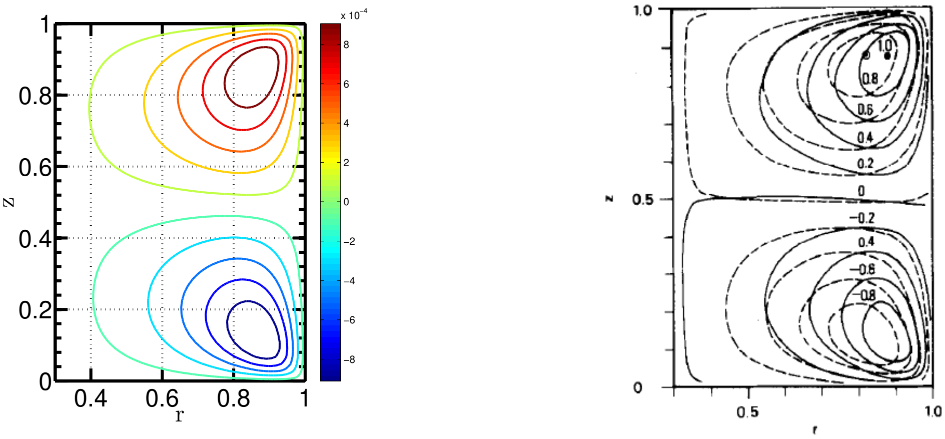

(a)

(b)

Fig. 2.11 Azimuthal velocity contours, case 2, (Table - 2.2) (a) present code and (b) Harada [17].

2.7 Mechanically Driven Flow - Code Validation

In this section, we compare present results for cases 3 and 4 from Harada [17], (Table - 2.2), see Figs. 2.12, 2.13, 2.14 and 2.15. We observe a good quantitative match between the velocity and angular velocity profiles, but for case 3, we could not find even a qualitative match with the published result of Harada [17], see, for example, Fig. 2.13. However, when the viscous dissipation was switched off, we again observe a good quantitative match between the published results and the ones produced with the present code.

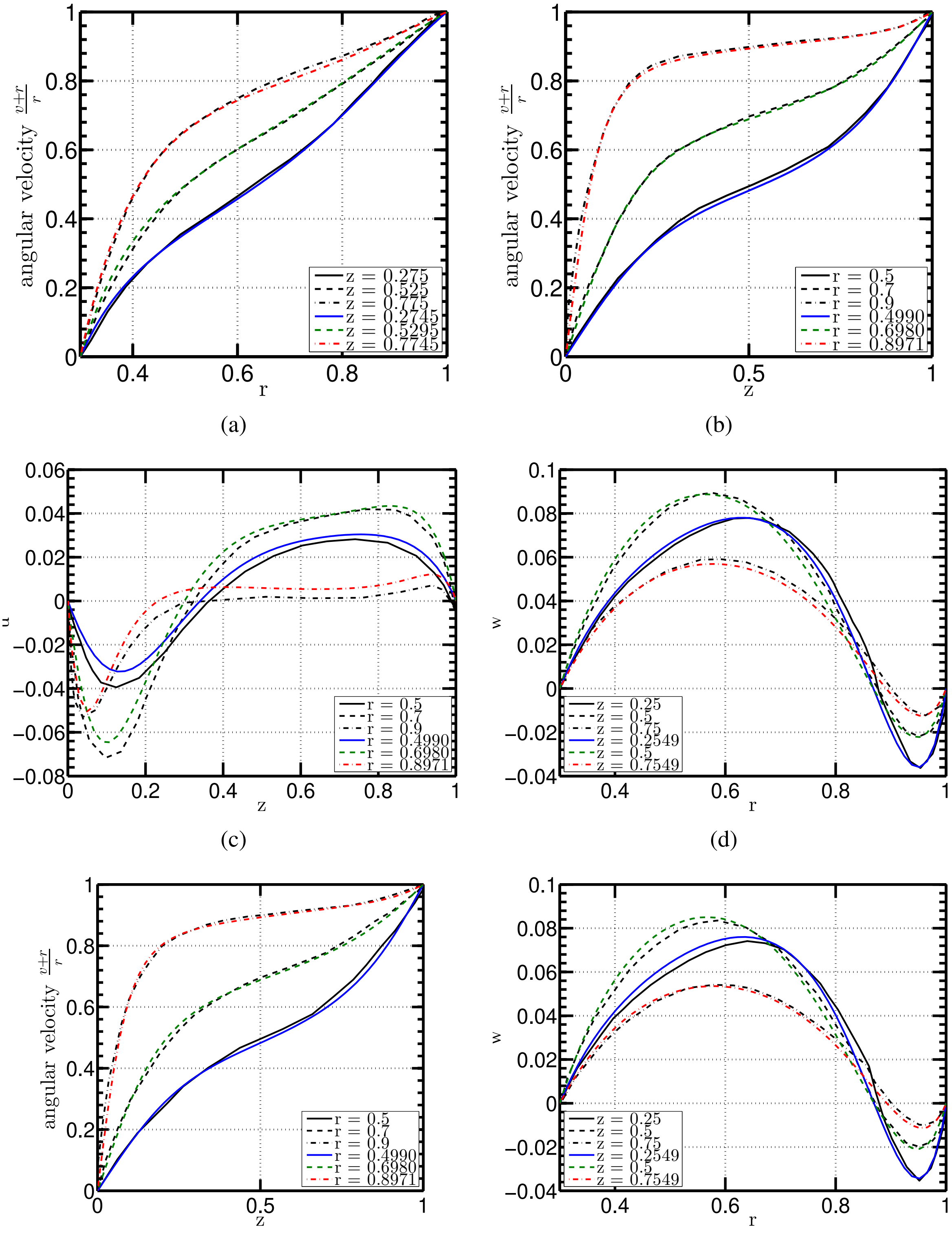

(a) (b) (c) (d) (e) (f)

Fig. 2.12 Profiles in black are from Harada [17], colored ones are from the present code. (a) angular velocity $\frac{v+r}{r}$ vs r at different z, case 3, (b) angular velocity $\frac{v+r}{r}$ vs z at different r, case 3, (c) u vs z at different r, case 3, (d) w vs r at different z, case 3, (e) angular velocity $\frac{v+r}{r}$ vs z at different r, case 4, (f) w vs r at different z, case 4.

The reasons for small departures of the present results from the published results may lie in the discretization. The code was run at 51×51 grid-size, while the published results were calculated at 19×21 grid-size. For details, see Harada [17]. Also, several printing mistakes were found in the manuscript, for example, in the Eqn. (15) of Harada [17], the Coriolis and the centrifugal terms are missing a factor of v, the azimuthal velocity. Furthermore, although the temperature contours differ qualitatively for case 3, they do seem to be following the no-flux or Neumann boundary condition, instead of Dirichlet boundary condition at the bottom wall. Finally, the correct temperature contours obtained from the present code for case 3 and 4 are plotted in Fig. 2.13 and Fig. 2.14:

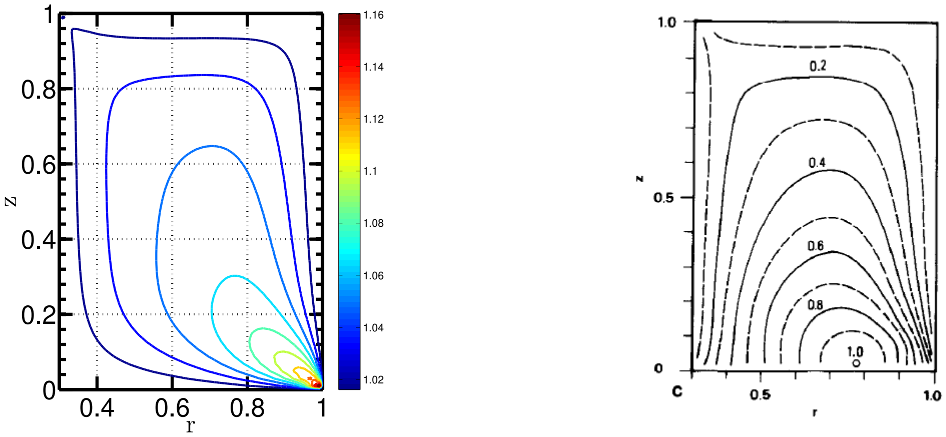

(a)

(b)

Fig. 2.13 Temperature contours, case 3, (Table - 2.2) (a) present code and (b) Harada [17].

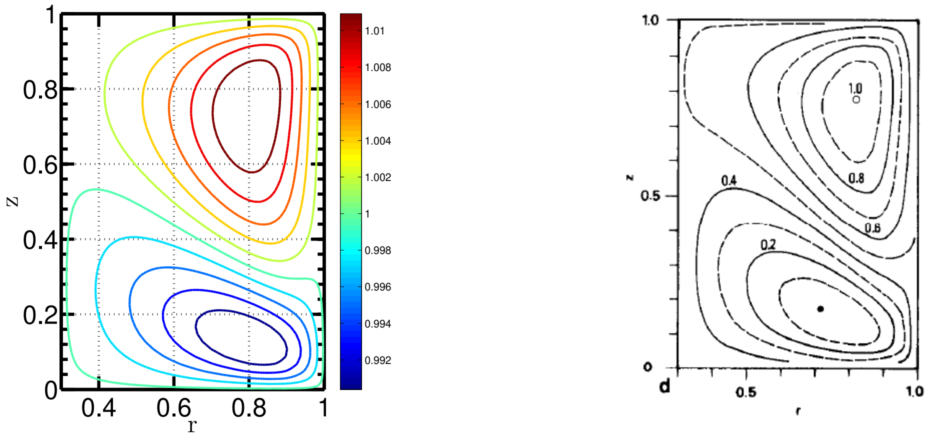

(a)

(b)

Fig. 2.14 Temperature contours, case 4, (Table - 2.2) (a) present code and (b) Harada [17].

The azimuthal velocity contours are found to match. We plot the azimuthal velocity contours for case 3 in Fig. 2.15

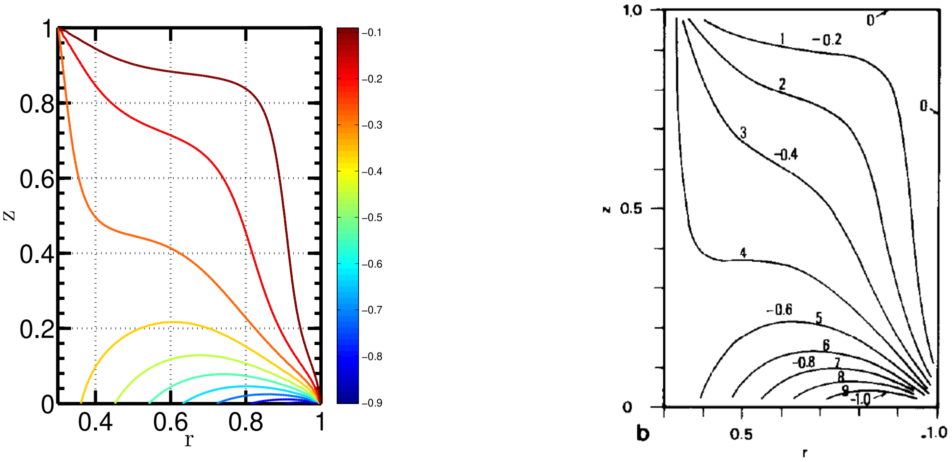

(a)

(b)

Fig. 2.15 Azimuthal velocity contours contours, case 3, (Table - 2.2) (a) present code and (b) Harada [17].

2.8 Summary and Conclusion

A variant of the numerical method used in Harada[17, 16] and Hyun and Park [19] has been developed. Results from the code developed using this method are compared with published literature Harada [17] for bench-marking. Physical interpretation is given in order to explain numerical results for both thermally and mechanically driven flows. Some mistakes in the work of Harada [17] have been identified and corrected. [see Fig. 2.13].

Chapter 3

Compressible Taylor-Couette Flow

> *"The worthwhile problems are the ones you can really solve or help solve, the ones you can really contribute something to. ...No problem is too small or too trivial if we can really do something about it. "* - Richard Feynman in a letter to a student.

3.1 Introduction

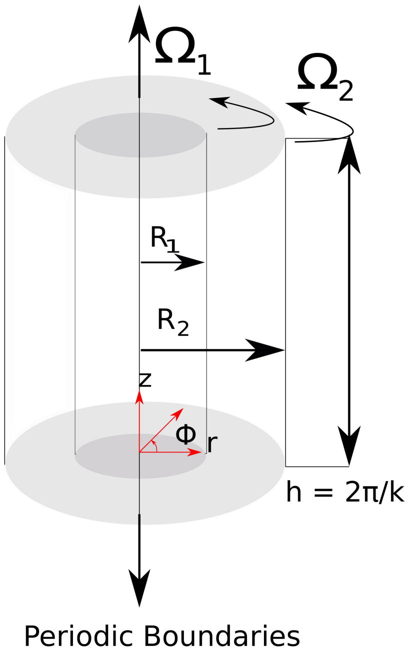
Ω_1
Ω_2
R_1
R_2
z
Φ
r
h = 2π/k
Periodic Boundaries

Fig. 3.1 Taylor-Couette flow (TCF) with periodic boundaries in z-direction.

Figure 3.1 shows a sketch of the Taylor-Couette geometry with periodic boundary conditions in axial direction. As usual, the inner and outer cylinders can rotate at different angular velocities. No top or bottom lids are assumed and this is achieved by applying periodic boundary conditions in the z-direction. The annulus is filled with an ideal gas.

3.2 Dimensional Governing Equations

The governing equations for a compressible gas are:
Continuity:

$$\frac{\partial \rho^*}{\partial t^*} + \nabla^* \cdot (\rho \underline{u}^*) = 0. \tag{3.1}$$

Momentum:

$$\rho^* \left(\frac{\partial \underline{u}^*}{\partial t^*} + \underline{u}^* \cdot \nabla^* \underline{u}^* \right) = -\nabla^* p^* + \nabla^* \cdot (2\hat{\mu}^*(\rho^*, T^*) \underline{\underline{e}}^*) + \nabla^* (\lambda^*(\rho^*, T^*) \nabla^* \cdot \underline{u}^*). \tag{3.2}$$

Energy:

$$\rho^* c_v \left(\frac{\partial T^*}{\partial t^*} + \underline{u}^* \cdot \nabla^* T^* \right) = -p^* \nabla^* \cdot \underline{u}^* + \nabla^* \cdot (\hat{\kappa}^*(\rho^*, T^*) \nabla^* T^*) + \Phi^*, \tag{3.3}$$

where

$$\Phi^* = \hat{\mu}^*(\rho^*, T^*) \left(2 e^*_{ij} e^*_{ij} \right) + \lambda^* (\nabla^* \cdot \underline{u}^*)^2 \tag{3.4}$$

Throughout this thesis, we have assumed Stokes' assumption of zero bulk viscosity ($\xi^* = \lambda^* + \frac{2\mu^*}{3} = 0$, see Eqn. (3.5)). Mathematically,

$$\begin{aligned} (\lambda^* + \frac{2\mu^*}{3}) &= \xi^*. \\ \Rightarrow \lambda^* &= -\frac{2\mu^*}{3}. \end{aligned} \tag{3.5}$$

Although the developed code is robust and can handle non-zero bulk viscosity as well, we only include results for zero bulk viscosity in this work. Also,

$$e^*_{ij} = \frac{1}{2} \left(\frac{\partial u^*_i}{\partial x^*_j} + \frac{\partial u^*_j}{\partial x^*_i} \right).$$

Finally, the equation of state for an ideal gas is:

$$p^* = (c^*_p - c^*_v) \rho^* T^* \tag{3.6}$$

where $(.)^*$ are dimensional quantities.

In literature, predominantly, there are two kinds of non-dimensionalizations leading to different non-dimensionalized equations. The terms remain the same, but the coefficients change depending on the choice of reference scales. Accordingly, the boundary conditions also change. We start with dimensional equations and then go on to derive general non-dimensional equations with characteristic length scale 'L_R', characteristic velocity scale 'U_R' and so on. We then plug in the different characteristic variables as described in the literature to derive different forms of dimensionless equations.

3.3 General Dimensionless Equations

Let us choose U_R^*, L_R^*, ρ_R^*, T_R^*, p_R^*, μ_R^*, k_R^* as the characteristic velocity, length, density, temperature, pressure, viscosity and thermal conductivity scales, respectively. It follows that the characteristic time scale will be $t_R^* = L_R^*/U_R^*$. Let us substitute $\underline{u}^* = U_R^*\underline{u}$, $\nabla^* = \frac{1}{L_R}\nabla$, $\rho^* = \rho_R^*\rho$, $T^* = T_R^*T$, $p^* = p_R^*p$, $\mu^* = \mu_R^*\mu$ and $\kappa^* = \kappa_R^*k$ in equations (3.1) – (3.6). Here, non-starred quantities are dimensionless.

Continuity:

$$\frac{\rho_R^*}{t_R^*}\frac{\partial\rho}{\partial t}+\frac{\rho_R^*U_R^*}{L_0^*}\nabla^*\cdot(\rho\underline{u})=0 \tag{3.7a}$$

⇒

$$\frac{\partial\rho}{\partial t}+\nabla\cdot(\rho\underline{u})=0. \tag{3.7b}$$

Momentum:

$$\left(\frac{\rho_R^*(U_R^*)^2}{L_R^*}\right)\rho\left(\frac{\partial\underline{u}}{\partial t}+\underline{u}\cdot\nabla\underline{u}\right)=\left(\frac{p_R^*}{L_R^*}\right)(-\nabla p)+\left(\frac{\mu_R^*U_R}{(L_R^*)^2}\right)\left[\nabla\cdot(2\hat{\mu}(\rho,T)\underline{\underline{e}})+\nabla(\lambda(\rho,T)\nabla\cdot\underline{u})\right], \tag{3.8a}$$

⇒

$$\rho\left(\frac{\partial\underline{u}}{\partial t}+\underline{u}\cdot\nabla\underline{u}\right)=\left(\frac{p_R^*}{\rho_R^*(U_R^*)^2}\right)(-\nabla p)+\left(\frac{\mu_R^*}{\rho_R^*U_R^*L_R^*}\right)\left[\nabla\cdot(2\hat{\mu}(\rho,T)\underline{\underline{e}})+\nabla(\lambda(\rho,T)\nabla\cdot\underline{u})\right]. \tag{3.8b}$$

Energy:

$$\left(\frac{\rho_R^*T_R^*U_R^*}{L_R^*}\right)\left[\rho\left(\frac{\partial T}{\partial t}+\underline{u}\cdot\nabla T\right)\right]=\frac{p_R^*U_R^*}{c_vL_R^*}(-p\nabla\cdot\underline{u})+\left(\frac{\kappa_R^*T_R^*}{c_v(L_R^*)^2}\right)(\nabla\cdot(\hat{\kappa}(\rho,T)\nabla T))+\left(\frac{(U_R^*)^2}{c_v(L_R^*)^2}\right)\Phi, \tag{3.9a}$$

$\Rightarrow$

$$\rho\left(\frac{\partial T}{\partial t}+\underline{u}\cdot\nabla T\right)=\frac{p_R^*}{c_v\rho_R^*T_R^*}(-p\nabla\cdot\underline{u})+\left(\frac{\kappa_R^*}{\rho_R^*U_R^*L_R^*c_v}\right)(\nabla\cdot(\hat{\kappa}(\rho,T)\nabla T))+\left(\frac{U_R}{\rho_R^*U_R^*L_R^*c_v}\right)\Phi. \tag{3.9b}$$

$$\lambda=-\frac{2\mu}{3}. \tag{3.10}$$

Equation of state for an ideal gas:

$$p_R^*p=(c_p-c_v)\rho_R^*T_R^*(\rho T). \tag{3.11}$$

Let us choose $p_R^*=(c_p-c_v)\rho_R^*T_R^*$ so that the non-dimensional equation of state becomes

$$p=\rho T. \tag{3.12}$$

From here, we will consider two different forms of non-dimensional equations. Table - 3.1 summarizes the characteristic quantities used in two methods of obtaining the dimensionless form. Method 1 uses inertial time scale

$$t_R=\frac{d}{\Omega_1 R_1}, \tag{3.13}$$

while method 2 uses viscous time scale as reference time scale.

$$t_R=\frac{\rho_R^*d^2}{\mu_R^*} \tag{3.14}$$

Another important difference between the two methods is that method 1 uses local density while method 2 uses average density as the characteristic density.

Quantity	Method 1	Method 2
t_R^*	$\frac{d}{\Omega_1 R_1}$	$\frac{\rho_R^* d^2}{\mu_R^*}$ (Viscous time scale)
L_R^*	$d = R_2 - R_1$	$d = R_2 - R_1$
U_R^*	$\Omega_1 R_1$	$\frac{\mu_R^*}{\rho_R^* d}$
ρ_R^*	$\rho^*\vert_{R_1}$ or $\rho^*\vert_{R_2}$	$\frac{M_t}{\pi(R_2^2 - R_1^2)}$
μ_R^*	$\mu^*\vert_{R_1}$	$\mu^*\vert_{R_1}$
κ_R^*	$\kappa^*\vert_{R_1}$	$\kappa^*\vert_{R_1}$
T_R^*	$T^*\vert_{R_1}$	$T^*\vert_{R_1}$
p_R^*	$(c_p - c_v)\rho_R^* T_R^*$	$(c_p - c_v)\rho_R^* T_R^*$

Table 3.1 Reference Scales.

NOTE:

- d is the gap width ⇒ $d = R_2 - R_1$
- M_t is the mass per unit length of the fluid in the cylindrical annulus. The reason for choosing this to non-dimensionalize ρ_R^* is motivated by experiments. Only M_t can be prescribed in experiments and not the local density [Welsh et al. [41].]
- $T^*|_{R_1}$ ⇒ temperature at the inner cylinder and so on.

3.3.1 Method 1

In this method, we consider a non-dimensionalization similar to Harada [17], Hyun and Park [19], Malik et al. [23] and Malik et al. [24]. The reference scales can be found in table -3.1. The dimensionless governing equations are:

$$\frac{\partial \rho}{\partial t} + \nabla \cdot (\rho \underline{u}) = 0, \tag{3.15}$$

$$\rho \frac{Du_i}{Dt} = -\frac{1}{\gamma Ma^2}\nabla p + \frac{1}{Re_1}\left[\mu(\rho,T)\nabla^2 \underline{u} + \frac{\partial}{\partial x_i}(\lambda \nabla \cdot u) + \mu \frac{\partial}{\partial x_i}(\nabla \cdot u) + (\nabla \mu)\cdot(\nabla u_i) + \frac{\partial \underline{u}}{\partial x_i}\cdot(\nabla \mu)\right], \tag{3.16}$$

$$\rho \frac{DT}{Dt} = -(\gamma - 1)p\nabla \cdot \underline{u} + \frac{\gamma}{Re_1}\nabla \cdot (\hat{\kappa}\nabla T) + \frac{(\gamma-1)\gamma Ma^2}{Re_1}\Phi, \tag{3.17}$$

$$p = \rho T, \tag{3.18}$$

where the inner Reynolds number based on the angular velocity of the inner cylinder is defined by

$$Re_1 = \frac{\rho_R^* U_R^* L_R^*}{\mu_R^*} = \frac{\rho_R^* \Omega_1 R_1 d}{\mu_R^*}. \tag{3.19a}$$

Prandtl number is defined by

$$Pr = \mu^* c_p / \hat{\kappa}^*. \tag{3.19b}$$

The dimensionless thermal diffusivity is

$$\hat{\kappa} = \frac{\mu}{Pr}, \tag{3.19c}$$

the peripheral Mach number is

$$Ma = \frac{U_R^*}{\sqrt{\gamma R T_R^*}}. \tag{3.19d}$$

where R is the universal gas constant and $\gamma = c_p/c_v$ is the ratio of specific heat capacities. We employ Stokes' assumption of zero bulk viscosity ($\xi = 0$) and write

$$\lambda = -\frac{2\mu}{3}. \tag{3.19e}$$

In this way of non-dimensionalizing the governing equations, the boundary conditions will take the following form:

- $u = w = 0$ on $r = \frac{\eta}{1-\eta}, r = \frac{1}{1-\eta}$,
- $v = Re_1$ on $r = \frac{\eta}{1-\eta}$,
- $v = Re_2$ on $r = \frac{1}{1-\eta}$,
- $T = 1$ on $r = \frac{\eta}{1-\eta}$,
- $T = \chi = \frac{T_2}{T_1}$ on $r = \frac{1}{1-\eta}$,
- Periodic boundary conditions in z- and ϕ-direction.
- $\eta = \frac{R_1}{R_2} = 0.5$
- $\chi = \frac{T_2}{T_1}$ is the temperature ratio.

3.3.2 Method 2

If we consider the viscous time scale as the characteristic time scale and non-dimensionalize ρ^* based on the mass per unit length of the fluid in the annulus M_t; we get the following non-dimensional form which is in line with Welsh et al. [41].

$$\frac{\partial \rho}{\partial t}+\nabla\cdot(\rho\underline{u})=0, \tag{3.20}$$

$$\begin{aligned}
&\rho\frac{Du_i}{Dt}\\
&=-\frac{Re_1^2}{Ma^2}\nabla p+\left[\mu(\rho,T)\nabla^2\underline{u}+\frac{\partial}{\partial x_i}(\lambda\nabla\cdot\underline{u})+\mu\frac{\partial}{\partial x_i}(\nabla\cdot\underline{u})+(\nabla\mu)\cdot(\nabla u_i)+\frac{\partial\underline{u}}{\partial x_i}\cdot(\nabla\mu)\right]\\
&=-\frac{Re_1^2}{Ma^2}\nabla p+\left[\mu(\rho,T)\nabla^2\underline{u}+\frac{\mu(\rho,T)}{3}\frac{\partial}{\partial x_i}(\nabla\cdot\underline{u})-\frac{2}{3}(\nabla\cdot\underline{u})\frac{\partial\mu(\rho,T)}{\partial x_i}+(\nabla\mu)\cdot(\nabla u_i)+\frac{\partial\underline{u}}{\partial x_i}\cdot(\nabla\mu)\right],
\end{aligned} \tag{3.21}$$

$$\rho\frac{DT}{Dt}=-(\gamma-1)p\nabla\cdot\underline{u}+\gamma\nabla\cdot(\hat{\kappa}\nabla T)+\frac{(\gamma-1)Ma^2}{Re_1^2}\Phi, \tag{3.22}$$

$$p=\rho T, \tag{3.23}$$

where

- $\eta=\frac{R_1}{R_2}=0.5$ throughout this chapter.
- Isothermal speed of sound $c_s^2=(c_p-c_v)(\rho_R^*)^2T_R^*d^2/(\mu_R^*)^2$.
- Peripheral Mach number is defined as $Ma=Re_1/c_s$.
- Reynolds numbers based on inner and outer angular velocities are $Re_i=\frac{\Omega_iR_i\rho_R^*d}{\mu_R^*}$, $i=1,2$.
- Prandtl number (Pr), dimensionless thermal diffusivity ($\hat{\kappa}$) and γ are the same as defined in Eqns. (3.19).
- Stokes' assumption of zero bulk viscosity is also taken to hold and can be written as Eqn. (3.19e).

The boundary conditions become:

- $u=w=0$ on $r=\frac{\eta}{1-\eta},r=\frac{1}{1-\eta}$,
- $v=Re_1$ on $r=\frac{\eta}{1-\eta}$,
- $v=Re_2$ on $r=\frac{1}{1-\eta}$,
- $T=1$ on $r=\frac{\eta}{1-\eta}$,

- $T = \chi = \frac{T_2}{T_1}$ on $r = \frac{1}{1-\eta}$,

- Periodic boundary conditions in z- and ϕ-direction.

3.4 Dimensionless Governing Equations and Boundary Conditions in Cylindrical Coordinates

"Formulas hamper the understanding." - S. Smale.

In this work, we use the second method of non-dimensionalization as defined in Section 3.3.2. The reason for adapting method 2 is because it is better to use average density as the characteristic quantity than the local one, as described in the work of Manela and Frankel [26] and Welsh et al. [41]. There are two advantages to this approach:

1. The effect of increasing Ma on the critical Re_1 can be established unequivocally.

2. Comparison with experiments can be made. As mentioned in Chapter 1, it is difficult to prescribe local density *a priori*, whereas average density can be prescribed in physical experiments.

We choose the cylindrical coordinate system with the z axis coinciding with the axis of rotation of the cylinders as shown in Fig. 3.1. We write (3.7)-(3.11) in cylindrical coordinates in **the rest frame of reference**.

Continuity:

$$\frac{\partial \rho}{\partial t} + \frac{1}{r}\frac{\partial}{\partial r}(r\rho u) + \frac{1}{r}\frac{\partial}{\partial \phi}(\rho v) + \frac{\partial}{\partial z}(\rho w) = 0. \tag{3.24}$$

r-Momentum:

$$\begin{aligned}
&\frac{\partial(\rho u)}{\partial t} + \frac{1}{r}\frac{\partial}{\partial r}[ru(\rho u)] + \frac{1}{r}\frac{\partial}{\partial \phi}[v(\rho u)] + \frac{\partial}{\partial z}[w(\rho u)] - \frac{\rho v^2}{r} \\
&= -\frac{Re_1^2}{Ma^2}\left(\frac{\partial p}{\partial r}\right) + \Bigg[\mu\left(\frac{\partial^2 u}{\partial r^2} + \frac{1}{r^2}\frac{\partial^2 u}{\partial \phi^2} + \frac{\partial^2 u}{\partial z^2} + \frac{\partial}{\partial r}\left(\frac{u}{r}\right) - \frac{2}{r^2}\frac{\partial v}{\partial \phi}\right) \\
&+ (\mu+\lambda)\frac{\partial}{\partial r}\left(\frac{1}{r}\frac{\partial}{\partial r}(ru) + \frac{1}{r}\frac{\partial}{\partial \phi}(v) + \frac{\partial}{\partial z}(w)\right) + \left(\frac{1}{r}\frac{\partial}{\partial r}(ru) + \frac{1}{r}\frac{\partial}{\partial \phi}(v) + \frac{\partial}{\partial z}(w)\right)\left(\frac{\partial \lambda}{\partial r}\right) \\
&+ \left(\frac{\partial \mu}{\partial r}\frac{\partial u}{\partial r} + \frac{1}{r^2}\frac{\partial \mu}{\partial \phi}\frac{\partial u}{\partial \phi} + \frac{\partial \mu}{\partial z}\frac{\partial u}{\partial z}\right) + \left(\frac{\partial \mu}{\partial r}\frac{\partial u}{\partial r} + \frac{1}{r}\frac{\partial \mu}{\partial \phi}\frac{\partial v}{\partial r} + \frac{\partial \mu}{\partial z}\frac{\partial w}{\partial r}\right)\Bigg].
\end{aligned} \tag{3.25}$$

ϕ-Momentum:

$$
\begin{aligned}
&\frac{\partial(\rho v)}{\partial t} + \frac{1}{r}\frac{\partial}{\partial r}[ru(\rho v)] + \frac{1}{r}\frac{\partial}{\partial \phi}[v(\rho v)] + \frac{\partial}{\partial z}[w(\rho v)] + \frac{\rho u v}{r} \\
&= -\frac{Re_1^2}{Ma^2}\left(\frac{1}{r}\frac{\partial p}{\partial \phi}\right) + \Bigg[\mu\left(\frac{\partial^2 v}{\partial r^2} + \frac{1}{r^2}\frac{\partial^2 v}{\partial \phi^2} + \frac{\partial^2 v}{\partial z^2} + \frac{\partial}{\partial r}\left(\frac{v}{r}\right) + \frac{2}{r^2}\frac{\partial u}{\partial \phi}\right) \\
&+ (\mu+\lambda)\frac{1}{r}\frac{\partial}{\partial \phi}\left(\frac{1}{r}\frac{\partial}{\partial r}(ru) + \frac{1}{r}\frac{\partial}{\partial \phi}(v) + \frac{\partial}{\partial z}(w)\right) + \frac{1}{r}\left(\frac{1}{r}\frac{\partial}{\partial r}(ru) + \frac{1}{r}\frac{\partial}{\partial \phi}(v) + \frac{\partial}{\partial z}(w)\right)\frac{\partial \lambda}{\partial \phi} \\
&+ \left(\frac{\partial \mu}{\partial r}\frac{\partial v}{\partial r} + \frac{1}{r^2}\frac{\partial \mu}{\partial \phi}\frac{\partial v}{\partial \phi} + \frac{\partial \mu}{\partial z}\frac{\partial v}{\partial z}\right) + \left(\frac{1}{r}\frac{\partial \mu}{\partial r}\left(\frac{\partial u}{\partial \phi} - v\right) + \frac{1}{r^2}\frac{\partial \mu}{\partial \phi}\left(\frac{\partial v}{\partial \phi} + u\right) + \frac{1}{r}\frac{\partial \mu}{\partial z}\frac{\partial w}{\partial \phi}\right)\Bigg].
\end{aligned}
\tag{3.26}
$$

z-Momentum:

$$
\begin{aligned}
&\frac{\partial(\rho w)}{\partial t} + \frac{1}{r}\frac{\partial}{\partial r}[ru(\rho w)] + \frac{1}{r}\frac{\partial}{\partial \phi}[v(\rho w)] + \frac{\partial}{\partial z}[w(\rho w)] \\
&= -\frac{Re_1^2}{Ma^2}\left(\frac{\partial p}{\partial z}\right) + \Bigg[\mu\left(\frac{\partial^2 w}{\partial r^2} + \frac{1}{r^2}\frac{\partial^2 w}{\partial \phi^2} + \frac{\partial^2 w}{\partial z^2} + \frac{1}{r}\frac{\partial w}{\partial r}\right) \\
&+ (\mu+\lambda)\frac{\partial}{\partial z}\left(\frac{1}{r}\frac{\partial}{\partial r}(ru) + \frac{1}{r}\frac{\partial}{\partial \phi}(v) + \frac{\partial}{\partial z}(w)\right) + \left(\frac{1}{r}\frac{\partial}{\partial r}(ru) + \frac{1}{r}\frac{\partial}{\partial \phi}(v) + \frac{\partial}{\partial z}(w)\right)\frac{\partial \lambda}{\partial z} \\
&+ \left(\frac{\partial \mu}{\partial r}\frac{\partial w}{\partial r} + \frac{1}{r^2}\frac{\partial \mu}{\partial \phi}\frac{\partial w}{\partial \phi} + \frac{\partial \mu}{\partial z}\frac{\partial w}{\partial z}\right) + \left(\frac{\partial \mu}{\partial r}\frac{\partial u}{\partial z} + \frac{1}{r}\frac{\partial \mu}{\partial \phi}\frac{\partial v}{\partial z} + \frac{\partial \mu}{\partial z}\frac{\partial w}{\partial z}\right)\Bigg].
\end{aligned}
\tag{3.27}
$$

Energy:

$$
\begin{aligned}
&\frac{\partial(\rho T)}{\partial t} + \frac{1}{r}\frac{\partial}{\partial r}[ru(\rho T)] + \frac{1}{r}\frac{\partial}{\partial \phi}[v(\rho T)] + \frac{\partial}{\partial z}[w(\rho T)] \\
&= -(\gamma-1)(p)\left(\frac{1}{r}\frac{\partial}{\partial r}(ru) + \frac{1}{r}\frac{\partial}{\partial \phi}(v) + \frac{\partial}{\partial z}(w)\right) + \gamma\Bigg[\hat{\kappa}\left(\frac{1}{r}\frac{\partial}{\partial r}\left(r\frac{\partial T}{\partial r}\right) + \frac{1}{r^2}\frac{\partial^2 T}{\partial \phi^2} + \frac{\partial^2 T}{\partial z^2}\right) \\
&+ \left(\frac{\partial T}{\partial r}\frac{\partial \hat{\kappa}}{\partial r} + \frac{1}{r^2}\frac{\partial T}{\partial \phi}\frac{\partial \hat{\kappa}}{\partial \phi} + \frac{\partial T}{\partial z}\frac{\partial \hat{\kappa}}{\partial z}\right)\Bigg] + (\gamma-1)\frac{Ma^2}{Re_1^2}\Phi,
\end{aligned}
\tag{3.28a}
$$

where

$$
\begin{aligned}
&\Phi = \mu(\rho,T)(2e_{ij}e_{ij}) + \lambda(\rho,T)(\nabla\cdot\underline{u})^2\\
&= \mu(\rho,T)\Bigg\{\Bigg[2\left(\frac{\partial u}{\partial r}\right)^2 + \frac{2}{r^2}\left(\frac{\partial v}{\partial \phi}+u\right)^2 + 2\left(\frac{\partial w}{\partial z}\right)^2\\
&+\left(\frac{1}{r}\left(\frac{\partial u}{\partial \phi}-v\right)+\frac{\partial v}{\partial r}\right)^2 + \left(\frac{\partial u}{\partial z}+\frac{\partial w}{\partial r}\right)^2 + \left(\frac{1}{r}\frac{\partial w}{\partial \phi}+\frac{\partial v}{\partial z}\right)^2\Bigg]\\
&+\frac{\lambda(\rho,T)}{\mu(\rho,T)}\left[\frac{1}{r^2}\left(\frac{\partial (ru)}{\partial r}\right)^2 + \frac{1}{r^2}\left(\frac{\partial v}{\partial \phi}\right)^2 + \left(\frac{\partial w}{\partial z}\right)^2 + \frac{2}{r^2}\frac{\partial (ru)}{\partial r}\frac{\partial v}{\partial \phi} + \frac{2}{r}\frac{\partial (ru)}{\partial r}\frac{\partial w}{\partial z} + \frac{2}{r}\frac{\partial w}{\partial z}\frac{\partial v}{\partial \phi}\right]\Bigg\}.
\end{aligned}
\tag{3.28b}
$$

For completeness, we write the boundary conditions again:

- $u = w = 0$ on $r = \frac{\eta}{1-\eta}, r = \frac{1}{1-\eta}$,
- $v = Re_1$ on $r = \frac{\eta}{1-\eta}$,
- $v = Re_2$ on $r = \frac{1}{1-\eta}$,
- $T = 1$ on $r = \frac{\eta}{1-\eta}$,
- $T = \chi = \frac{T_2}{T_1}$ on $r = \frac{1}{1-\eta}$,
- Periodic boundary conditions in z- and ϕ-direction.

where

- $\eta = \frac{R_1}{R_2} = 0.5$ throughout this chapter.
- Isothermal speed of sound $c_s^2 = (c_p - c_v)(\rho_R^*)^2 T_R^* d^2/(\mu_R^*)^2$.
- Peripheral Mach number is defined as $Ma = Re_1/c_s$.
- Reynolds numbers based on inner and outer angular velocities are $Re_i = \frac{\Omega_i R_i \rho_R^* d}{\mu_R^*}$, $i = 1,2$.
- Prandtl number (Pr), dimensionless thermal diffusivity ($\hat{\kappa}$) and γ are the same as defined in Eqns. (3.19).
- Stokes' assumption of zero bulk viscosity is also taken to be true and can be written as Eqn. (3.19e).

3.4.1 Governing Equations for an Axisymmetric Flow

While writing the governing equations for an axisymmetric flow, we switch off the ϕ-derivatives, thereby imposing axisymmetry. **Continuity:**

$$\frac{\partial \rho}{\partial t}+\frac{1}{r}\frac{\partial}{\partial r}(r\rho u)+\frac{\partial}{\partial z}(\rho w)=0. \tag{3.29}$$

r-Momentum:

$$\begin{aligned}
&\frac{\partial(\rho u)}{\partial t}+\frac{1}{r}\frac{\partial}{\partial r}[ru(\rho u)]+\frac{\partial}{\partial z}[w(\rho u)]-\frac{\rho v^2}{r}\\
&=-\frac{Re_1^2}{Ma^2}\left(\frac{\partial p}{\partial r}\right)+\left[\mu\left(\frac{\partial^2 u}{\partial r^2}+\frac{\partial^2 u}{\partial z^2}+\frac{\partial}{\partial r}\left(\frac{u}{r}\right)\right)\right.\\
&+(\mu+\lambda)\frac{\partial}{\partial r}\left(\frac{1}{r}\frac{\partial}{\partial r}(ru)+\frac{\partial}{\partial z}(w)\right)+\left(\frac{1}{r}\frac{\partial}{\partial r}(ru)+\frac{\partial}{\partial z}(w)\right)\left(\frac{\partial \lambda}{\partial r}\right)\\
&\left.+\left(\frac{\partial \mu}{\partial r}\frac{\partial u}{\partial r}+\frac{\partial \mu}{\partial z}\frac{\partial u}{\partial z}\right)+\left(\frac{\partial \mu}{\partial r}\frac{\partial u}{\partial r}+\frac{\partial \mu}{\partial z}\frac{\partial w}{\partial r}\right)\right].
\end{aligned} \tag{3.30}$$

ϕ-Momentum:

$$\begin{aligned}
&\frac{\partial(\rho v)}{\partial t}+\frac{1}{r}\frac{\partial}{\partial r}[ru(\rho v)]+\frac{\partial}{\partial z}[w(\rho v)]+\frac{\rho uv}{r}\\
&=\left[\mu\left(\frac{\partial^2 v}{\partial r^2}+\frac{\partial^2 v}{\partial z^2}+\frac{\partial}{\partial r}\left(\frac{v}{r}\right)\right)+\left(\frac{\partial \mu}{\partial r}\frac{\partial v}{\partial r}+\frac{\partial \mu}{\partial z}\frac{\partial v}{\partial z}\right)+\frac{1}{r}\frac{\partial \mu}{\partial r}\left(-v\right)\right].
\end{aligned} \tag{3.31}$$

z-Momentum:

$$\begin{aligned}
&\frac{\partial(\rho w)}{\partial t}+\frac{1}{r}\frac{\partial}{\partial r}[ru(\rho w)]+\frac{\partial}{\partial z}[w(\rho w)]\\
&=-\frac{Re_1^2}{Ma^2}\left(\frac{\partial p}{\partial z}\right)+\left[\mu\left(\frac{\partial^2 w}{\partial r^2}+\frac{\partial^2 w}{\partial z^2}+\frac{1}{r}\frac{\partial w}{\partial r}\right)\right.\\
&+(\mu+\lambda)\frac{\partial}{\partial z}\left(\frac{1}{r}\frac{\partial}{\partial r}(ru)+\frac{\partial}{\partial z}(w)\right)+\left(\frac{1}{r}\frac{\partial}{\partial r}(ru)+\frac{\partial}{\partial z}(w)\right)\frac{\partial \lambda}{\partial z}\\
&\left.+\left(\frac{\partial \mu}{\partial r}\frac{\partial w}{\partial r}+\frac{\partial \mu}{\partial z}\frac{\partial w}{\partial z}\right)+\left(\frac{\partial \mu}{\partial r}\frac{\partial u}{\partial z}+\frac{\partial \mu}{\partial z}\frac{\partial w}{\partial z}\right)\right].
\end{aligned} \tag{3.32}$$

Energy:

$$\begin{aligned}&\frac{\partial(\rho T)}{\partial t}+\frac{1}{r}\frac{\partial}{\partial r}[r(\rho u)T]+\frac{\partial}{\partial z}[(\rho w)T]\\&=-(\gamma-1)(p)\left(\frac{1}{r}\frac{\partial}{\partial r}(ru)+\frac{\partial}{\partial z}(w)\right)+\gamma\left[\kappa\left(\frac{1}{r}\frac{\partial}{\partial r}\left(r\frac{\partial T}{\partial r}\right)+\frac{\partial^2 T}{\partial z^2}\right)\right.\\&\left.+\left(\frac{\partial T}{\partial r}\frac{\partial \kappa}{\partial r}+\frac{\partial T}{\partial z}\frac{\partial \kappa}{\partial z}\right)\right]+(\gamma-1)\frac{Ma^2}{Re_1^2}\Phi,\end{aligned} \tag{3.33a}$$

where

$$\begin{aligned}&\Phi=\mu(\rho,T)(2e_{ij}e_{ij})+\lambda(\rho,T)(\nabla\cdot\underline{u})^2\\&=\mu(\rho,T)\left[2\left(\frac{\partial u}{\partial r}\right)^2+\frac{2}{r^2}\left(u\right)^2+2\left(\frac{\partial w}{\partial z}\right)^2+\left(\frac{1}{r}\left(-v\right)+\frac{\partial v}{\partial r}\right)^2+\left(\frac{\partial u}{\partial z}+\frac{\partial w}{\partial r}\right)^2+\left(\frac{\partial v}{\partial z}\right)^2\right]\\&+\lambda(\rho,T)\left[\frac{1}{r^2}\left(\frac{\partial(ru)}{\partial r}\right)^2+\left(\frac{\partial w}{\partial z}\right)^2+\frac{2}{r}\frac{\partial(ru)}{\partial r}\frac{\partial w}{\partial z}\right].\end{aligned} \tag{3.33b}$$

3.4.2 Writing Governing Equations in Terms of $\bar{\rho}$

Consider mass conservation, Eq. (3.27). Multiplying Eq. (3.27) throughout by r gives

$$\frac{\partial(\rho r)}{\partial t}+\frac{\partial}{\partial r}(r\rho u)+\frac{\partial}{\partial z}(r\rho w)=0. \tag{3.34}$$

Defining

$$\bar{\rho}=\rho r, \tag{3.35}$$

The continuity equation reduces to

$$\frac{\partial\bar{\rho}}{\partial t}+\frac{\partial}{\partial r}(\bar{\rho}u)+\frac{\partial}{\partial z}(\bar{\rho}w)=0. \tag{3.36}$$

Notice how the convective derivatives look **as if** they were written in Cartesian coordinates. Doing the same thing for momentum and energy equations, we convert the equations in terms of the new variable $\bar{\rho}$. This converts the convective derivatives into ones that look like Cartesian convective derivatives. The momentum and energy equations then take the following form:

r-Momentum:

$$
\begin{aligned}
&\frac{\partial(\bar{\rho}u)}{\partial t}+\frac{\partial}{\partial r}[u(\bar{\rho}u)]+\frac{\partial}{\partial z}[w(\bar{\rho}u)]-\frac{\bar{\rho}v^2}{r}\\
&=-\frac{Re_1^2}{Ma^2}\left(r\frac{\partial p}{\partial r}\right)+r\left[\mu\left(\frac{\partial^2 u}{\partial r^2}+\frac{\partial^2 u}{\partial z^2}+\frac{\partial}{\partial r}\left(\frac{u}{r}\right)\right)\right.\\
&+(\mu+\lambda)\frac{\partial}{\partial r}\left(\frac{1}{r}\frac{\partial}{\partial r}(ru)+\frac{\partial}{\partial z}(w)\right)+\left(\frac{1}{r}\frac{\partial}{\partial r}(ru)+\frac{\partial}{\partial z}(w)\right)\left(\frac{\partial\lambda}{\partial r}\right)\\
&\left.+\left(\frac{\partial\mu}{\partial r}\frac{\partial u}{\partial r}+\frac{\partial\mu}{\partial z}\frac{\partial u}{\partial z}\right)+\left(\frac{\partial\mu}{\partial r}\frac{\partial u}{\partial r}+\frac{\partial\mu}{\partial z}\frac{\partial w}{\partial r}\right)\right].
\end{aligned}
\tag{3.37}
$$

ϕ-Momentum:

$$
\begin{aligned}
&\frac{\partial(\bar{\rho}v)}{\partial t}+\frac{\partial}{\partial r}[u(\bar{\rho}v)]+\frac{\partial}{\partial z}[w(\bar{\rho}v)]+\frac{\bar{\rho}uv}{r}\\
&=r\left[\mu\left(\frac{\partial^2 v}{\partial r^2}+\frac{\partial^2 v}{\partial z^2}+\frac{\partial}{\partial r}\left(\frac{v}{r}\right)\right)+\left(\frac{\partial\mu}{\partial r}\frac{\partial v}{\partial r}+\frac{\partial\mu}{\partial z}\frac{\partial v}{\partial z}\right)+\frac{1}{r}\frac{\partial\mu}{\partial r}\left(-v\right)\right].
\end{aligned}
\tag{3.38}
$$

z-Momentum:

$$
\begin{aligned}
&\frac{\partial(\bar{\rho}w)}{\partial t}+\frac{\partial}{\partial r}[u(\bar{\rho}w)]+\frac{\partial}{\partial z}[w(\bar{\rho}w)]\\
&=-\frac{Re_1^2}{Ma^2}\left(r\frac{\partial p}{\partial z}\right)+r\left[\mu\left(\frac{\partial^2 w}{\partial r^2}+\frac{\partial^2 w}{\partial z^2}+\frac{1}{r}\frac{\partial w}{\partial r}\right)\right.\\
&+(\mu+\lambda)\frac{\partial}{\partial z}\left(\frac{1}{r}\frac{\partial}{\partial r}(ru)+\frac{\partial}{\partial z}(w)\right)+\left(\frac{1}{r}\frac{\partial}{\partial r}(ru)+\frac{\partial}{\partial z}(w)\right)\frac{\partial\lambda}{\partial z}\\
&\left.+\left(\frac{\partial\mu}{\partial r}\frac{\partial w}{\partial r}+\frac{\partial\mu}{\partial z}\frac{\partial w}{\partial z}\right)+\left(\frac{\partial\mu}{\partial r}\frac{\partial u}{\partial z}+\frac{\partial\mu}{\partial z}\frac{\partial w}{\partial z}\right)\right].
\end{aligned}
\tag{3.39}
$$

Energy:

$$
\begin{aligned}
&\frac{\partial(\bar{\rho}T)}{\partial t}+\frac{\partial}{\partial r}[(\bar{\rho}u)T]+\frac{\partial}{\partial z}[(\bar{\rho}w)T]\\
&=-(\gamma-1)(p)r\left(\frac{1}{r}\frac{\partial}{\partial r}(ru)+\frac{\partial}{\partial z}(w)\right)+r\gamma\left[\kappa\left(\frac{1}{r}\frac{\partial}{\partial r}\left(r\frac{\partial T}{\partial r}\right)+\frac{\partial^2 T}{\partial z^2}\right)\right.\\
&\left.+\left(\frac{\partial T}{\partial r}\frac{\partial\kappa}{\partial r}+\frac{\partial T}{\partial z}\frac{\partial\kappa}{\partial z}\right)\right]+r(\gamma-1)\frac{Ma^2}{Re_1^2}\Phi,
\end{aligned}
\tag{3.40a}
$$

where

$$
\begin{aligned}
\Phi &= \mu(\rho,T)(2e_{ij}e_{ij}) + \lambda(\rho,T)(\nabla\cdot\underline{u})^2 \\
&= \mu(\rho,T)\left[2\left(\frac{\partial u}{\partial r}\right)^2 + \frac{2}{r^2}\left(u\right)^2 + 2\left(\frac{\partial w}{\partial z}\right)^2 + \left(\frac{1}{r}\left(-v\right) + \frac{\partial v}{\partial r}\right)^2 + \left(\frac{\partial u}{\partial z} + \frac{\partial w}{\partial r}\right)^2 + \left(\frac{\partial v}{\partial z}\right)^2\right] \\
&+ \lambda(\rho,T)\left[\frac{1}{r^2}\left(\frac{\partial(ru)}{\partial r}\right)^2 + \left(\frac{\partial w}{\partial z}\right)^2 + \frac{2}{r}\frac{\partial(ru)}{\partial r}\frac{\partial w}{\partial z}\right].
\end{aligned}
\tag{3.40b}
$$

Also, Stokes' assumption of zero bulk viscosity ($\xi = 0$) is used according to Eqn. (3.19e).

3.4.3 Numerical Method

Numerical method as described in Section 2.3 of Chapter 2 was used. Central differences were used to approximate first and mixed spatial derivatives. For second derivatives, DuFort-Frankel or leapfrog type scheme was used as described in Subsection 2.3.3. To approximate convective derivatives, upwind scheme was used as explained in Subsection 2.3.2. Overall accuracy of the scheme was hence second order in space owing to central difference, DuFort-Frankel and upwind schemes and second order in time, due to two-level time stepping employed in the DuFort-Frankel method. To avoid computational splitting inherent to the DuFort-Frankel method, filtering was done after every 20 dimensionless time-steps as discussed in Subsection 2.3.4. The algorithm was as enumerated in Section 2.4, motivated by Harada[17, 16] and Hyun and Park [19].

3.5 Verifying the Base State for Compressible Taylor-Couette Flow

Another check for verification of the code is to find the base state for the compressible TCF. In the dimensionless form, the base state can be solved for analytically, except for the density field [see Welsh et al. [41]]. To find the base state from Eqns. (3.24)-(3.28), subjected to appropriate boundary conditions, we seek a solution with $u_0 = w_0 = 0$. We follow Chandrasekhar [5] and write

$$v_0(r) = Ar + \frac{B}{r}, \tag{3.41}$$

where

$$A = Re_1 \frac{\mu' - \eta^2}{\eta(1+\eta)} \tag{3.42a}$$

and

$$B = Re_1 \frac{\eta(1-\mu')}{(1-\eta)(1-\eta^2)}, \tag{3.42b}$$

where the radius ratio is given by $\eta = R_1/R_2$ and the rotation ratio is $\mu' = \Omega_2/\Omega_1$. To get the steady state temperature, we need to solve the following equation.

$$\frac{1}{r}\frac{d}{dr}\left(r\frac{dT_0}{dr}\right) + \frac{\gamma-1}{\gamma}\frac{PrMa^2}{Re_1^2}\left[r\frac{d}{dr}\left(\frac{v_0}{r}\right)\right]^2 = 0. \tag{3.43}$$

Analytical solution for Eqn. (3.43) is known, given in Welsh et al. [41],

$$T_0(r) = \chi + \frac{\gamma-1}{\gamma}\frac{PrMa^2}{Re_1^2}B^2\left(C\ln r - \frac{1}{r^2} + D\right) + (1-\chi)\frac{\ln[r(1-\eta)]}{\ln\eta}, \tag{3.44}$$

with

$$C = \frac{(1-\eta^2)(1-\eta)^2}{\eta^2\ln\eta} \tag{3.45a}$$

and

$$D = (1-\eta^2)\left[1 + \frac{1-\eta^2}{\eta^2}\frac{\ln(1-\eta)}{\ln\eta}\right]. \tag{3.45b}$$

Unlike velocity and temperature fields, the density field in the steady base state cannot be determined analytically. We derive the equation for the steady state mass density and solve it using numerical methods. From there, we derive the steady state density field.

The non-dimensionalization adapted here is based on the mass per unit length of the fluid in the annular region (denoted in non-dimensional terms by M). In the non-dimensional terms, the base-state density is

$$\rho_0(r) = \frac{1}{2\pi r}\frac{dM}{dr}. \tag{3.46}$$

Also, in the base state, the $r-$momentum equation can be written as

$$\begin{aligned} -\frac{\rho_0 v_0^2}{r} &= -\frac{Re_1^2}{Ma^2}\left[T_0\frac{d\rho_0}{dr} + \rho_0\frac{dT_0}{dr}\right] \\ \Rightarrow \frac{Ma^2}{Re_1^2}\frac{v_0^2}{rT_0} &= \frac{1}{\rho_0}\frac{d\rho_0}{dr} + \frac{1}{T_0}\frac{dT_0}{dr}. \end{aligned} \tag{3.47}$$

From Eqn.(3.46),

$$\frac{d\rho_0}{dr} = \frac{1}{2\pi}\left[\frac{1}{r}\frac{d^2M}{dr^2} - \frac{1}{r^2}\frac{dM}{dr}\right], \tag{3.48}$$

using Eqn.(3.46) in Eqn.(3.48) ⇒

$$\frac{d^2M}{dr^2}+\left(\frac{1}{T_0}\frac{dT_0}{dr}-\frac{Ma^2}{Re_1^2}\frac{v_0^2}{rT_0}-\frac{1}{r}\right)\frac{dM}{dr}=0. \tag{3.49}$$

We need two boundary conditions to solve for $M(r)$. From the definition of $M(r)$,

$$M=2\pi\int_{\frac{\eta}{1-\eta}}^{r}\rho_0(s)sds. \tag{3.50}$$

we obtain the required boundary conditions. The boundary condition at $r=\frac{\eta}{1-\eta}$ follows from the above integral Eqn.(3.48):

$$M\left(r=\frac{\eta}{1-\eta}\right)=0. \tag{3.51}$$

To get the second boundary condition, recall from table -3.1 that M was non-dimensionalized by M_t, total mass per unit length of fluid in the annulus, whereas the density was non-dimensionalized using the average density. When $r=\frac{1}{1-\eta}$, the whole of mass in the annular region is covered. So, we can directly write,

$$\begin{aligned}M\left(r=\frac{1}{1-\eta}\right)&=\pi\left[\left(\frac{\eta}{1-\eta}\right)^2-\left(\frac{1}{1-\eta}\right)^2\right]\\ \Rightarrow M\left(r=\frac{1}{1-\eta}\right)&=\pi\frac{(1+\eta)}{(1-\eta)}.\end{aligned} \tag{3.52}$$

To get the base state density, we first solve Eqn. (3.49) subject to Eqn. (3.51) and Eqn. (3.52). The method used to solve this differential equation is higher order compact finite difference method as described in Lele [22] and Zhang et al. [43]. From M, we can easily find the steady state density field by Eqn. (3.46).

We now compare the results of these solutions obtained analytically and with higher order compact finite difference methods to the base state obtained by time marching. The length of the computational domain was kept to be $\pi/2$ with periodic boundaries in the axial direction. This particular length was chosen in order to ensure that we get the base state consistent with our assumptions that $u_0=w_0=0$. The base states for different Mach (Ma) numbers at Prandtl (Pr)$=1$ and different Prandtl (Pr) numbers at Mach (Ma) $=1$ are compared for various inner Reynolds numbers (Re_1) in Fig. - (3.2) and (3.3).

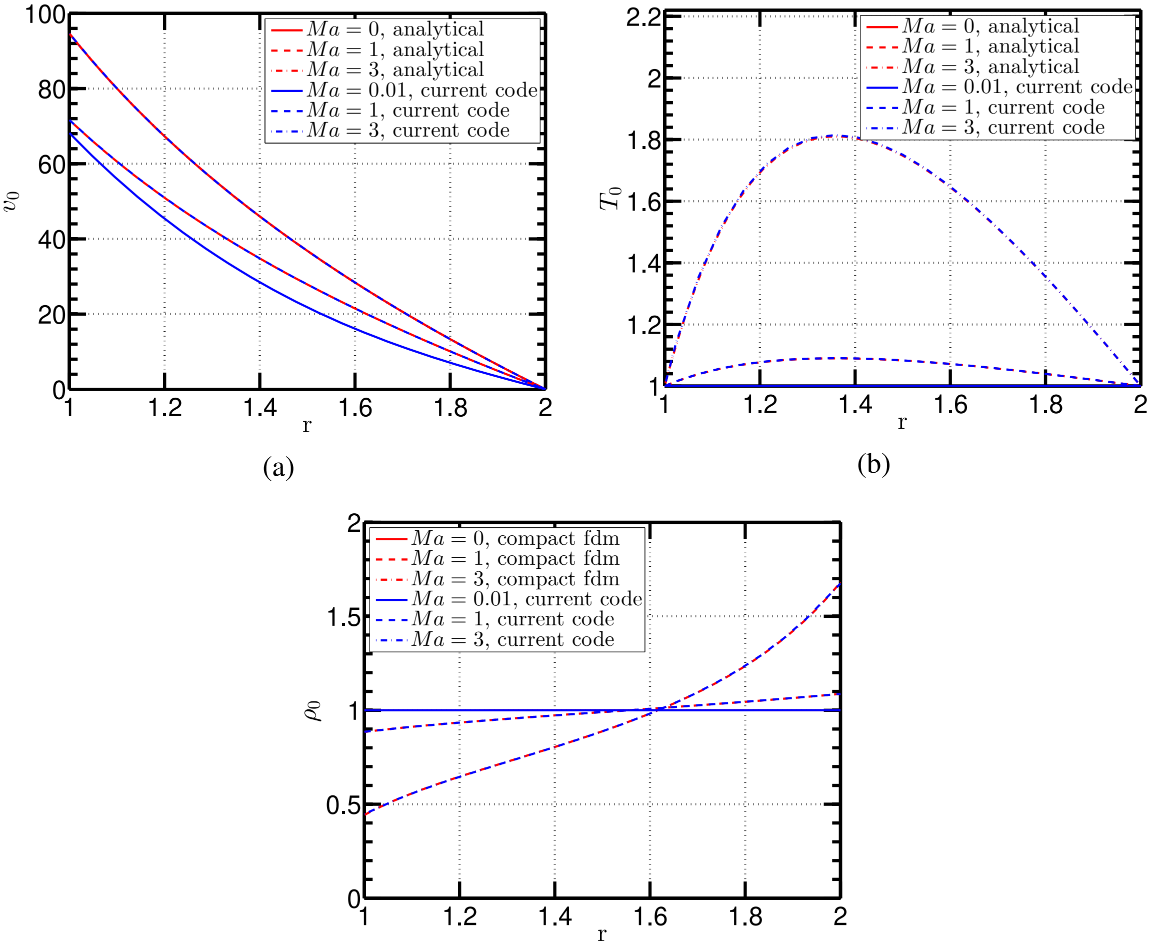

(a)

(b)

(c)

Fig. 3.2 Base state for $Pr = 1$, $Re_2 = 0$, $Re_1 =$ close to critical, varying Ma: (a)v_0 versus r, (b)T_0 vs r, (c) ρ_0 vs r.

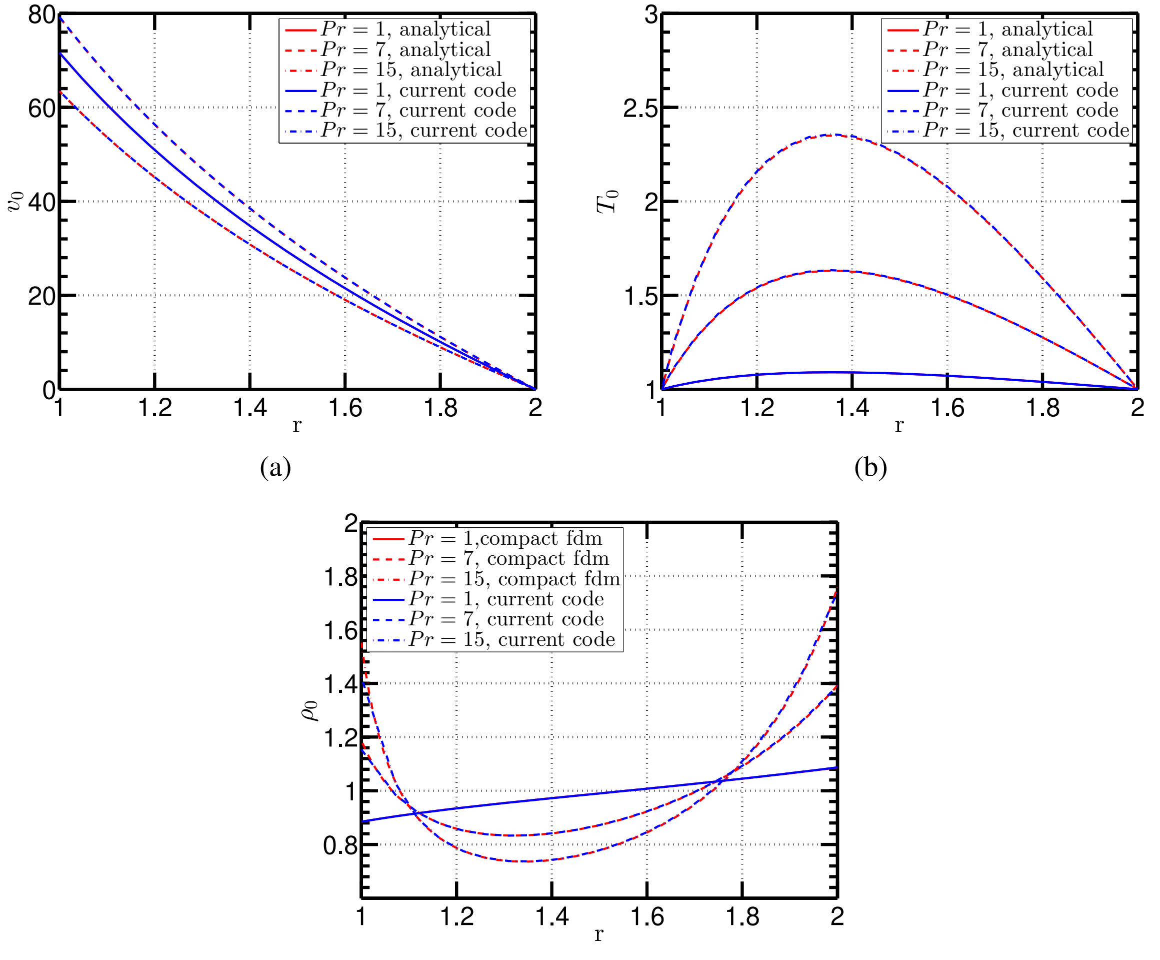

(a)

(b)

(c)

Fig. 3.3 Base state for $Ma = 1$, $Re_2 = 0$, $Re_1 =$ close to critical, varying Pr: (a)v_0 versus r, (b)T_0 vs r, (c) ρ_0 vs r.

3.5.1 Observations and Interpretation

At higher Ma, the variations in the density profile can be quite large at moderate Pr, see Fig. 3.2c and Fig. 3.3c. This again justifies the choice of the average density over density at the inner wall as a characteristic quantity to non-dimensionalize density. Also, in the low Ma limit, the constant temperature and density profiles are recovered (Fig.3.2c), corresponding to the incompressible case. With increasing Ma, the contribution of the viscous dissipation term in the energy equation becomes more and more significant, reflected in the hump of the temperature profile, see Fig. 3.2b.

It is evident from the Fig 3.3b, the gradients in temperature increase with increasing Pr for a given Ma number. This can be understood from the energy equation (Eqn. (3.24)). The thermal diffusivity $\hat{\kappa}$ is inversely proportional to Pr. Increasing Pr causes increase in ∇T. Because of high temperature gradients, the material expands locally and causes a depletion in the local density which is also evident from the density plots in Fig. 3.3c. With increasing Pr, the density gradients also increase and there is a minima in the density profile for higher Pr. Because of the centrifugal force, the effective gravity points in the radially outward direction. For higher Pr, near the inner wall there is an unstable density gradient, while near the outer wall, a stable stratification corresponding to a positive density gradient exists. This stable stratification can support gravity waves.

3.6 Effect of Variable Transport Coefficients

The first bifurcation from the circular Couette flow (CCF) when the inner cylinder is rotating and the outer one is stationary is known to be axisymmetric Taylor vortex flow (TVF). The aim of this section is to quantify the bifurcation from the CCF to TVF and examine the effects of variable transport coefficients on the onset of the well-known Taylor vortex flow (TVF).

We use the Sutherland's law to describe the temperature dependence of viscosity (see Eqn. (3.55)). Thermal conductivity is related to viscosity via the Prandtl number. We find that inclusion of variable viscosity and thermal conductivity increases the critical Reynolds number beyond which axisymmetric Taylor rolls set in. For quantitative comparison we plot some relevant quantity such as circulation versus the inner Reynolds number and get the canonical pitchfork bifurcation.

3.6.1 Average Kinetic Energies

To check grid independence, average total kinetic energy versus time are plotted, see Fig. 3.4. To define averages, we follow Harada [17] again.

As discussed in Harada [17], we can define averages as given in Eq. (3.53).

$$\langle \phi \rangle = 2\pi \int_{\frac{\eta}{1-\eta}}^{\frac{1}{1-\eta}} \int_0^{L_z} \phi r dr dz \tag{3.53}$$

$$E_u = \langle \frac{1}{2} \rho u^2 \rangle, \tag{3.54a}$$

$$E_v = \langle \frac{1}{2} \rho v^2 \rangle, \tag{3.54b}$$

$$E_w = \langle \frac{1}{2} \rho w^2 \rangle, \tag{3.54c}$$

and

$$KE = E_u + E_v + E_w. \tag{3.54d}$$

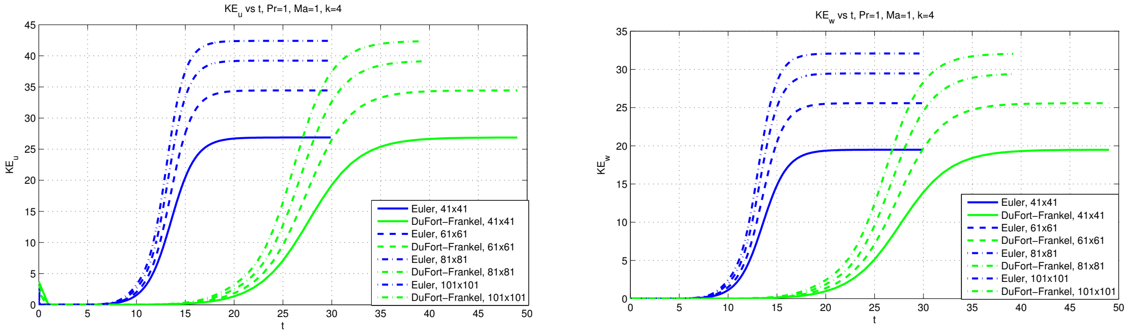

Fig. 3.4 Checking grid independence: $Re_1 = 75$, $k = 4$, $Ma = 1$, $Pr = 1$: (a) KE_u versus t and (b) KE_w versus t.

There are three important conclusions that we shall draw from figure (3.4):

1. Euler and DuFort-Frankel leapfrog type schemes relax to the same steady state energy for a given grid size.
2. Euler time integration relaxes to the steady state earlier than DuFort-Frankel leapfrog type scheme. But the trade-off here is in terms of the time step. We can afford a slightly higher time step for the DuFort-Frankel leapfrog type scheme, but it takes longer time to approach to the steady state. On the other hand, Euler time integration approaches the steady state earlier but we have to go in smaller time steps.
3. As the grid size is increased, the difference between the steady state kinetic energies decreases.

In present calculations, we use a grid-size of 101×101. For results at higher Re_1 in Section 3.7, we use a coarser grid of 41×41 in order to gain speed in terms of computational time, as well as to avoid numerical instabilities.

3.6.2 Sutherland's Law of Shear Viscosity

According to Sutherland's law the variation of viscosity with temperature is described by the following relation, see Sutherland [38].

$$\mu(T) = \frac{T^{\frac{3}{2}}(1+C)}{(T+C)}, \tag{3.55}$$

where $C = 0.5$ throughout this thesis.

3.6.3 Circulation of a Two-roll Structure - Comparison

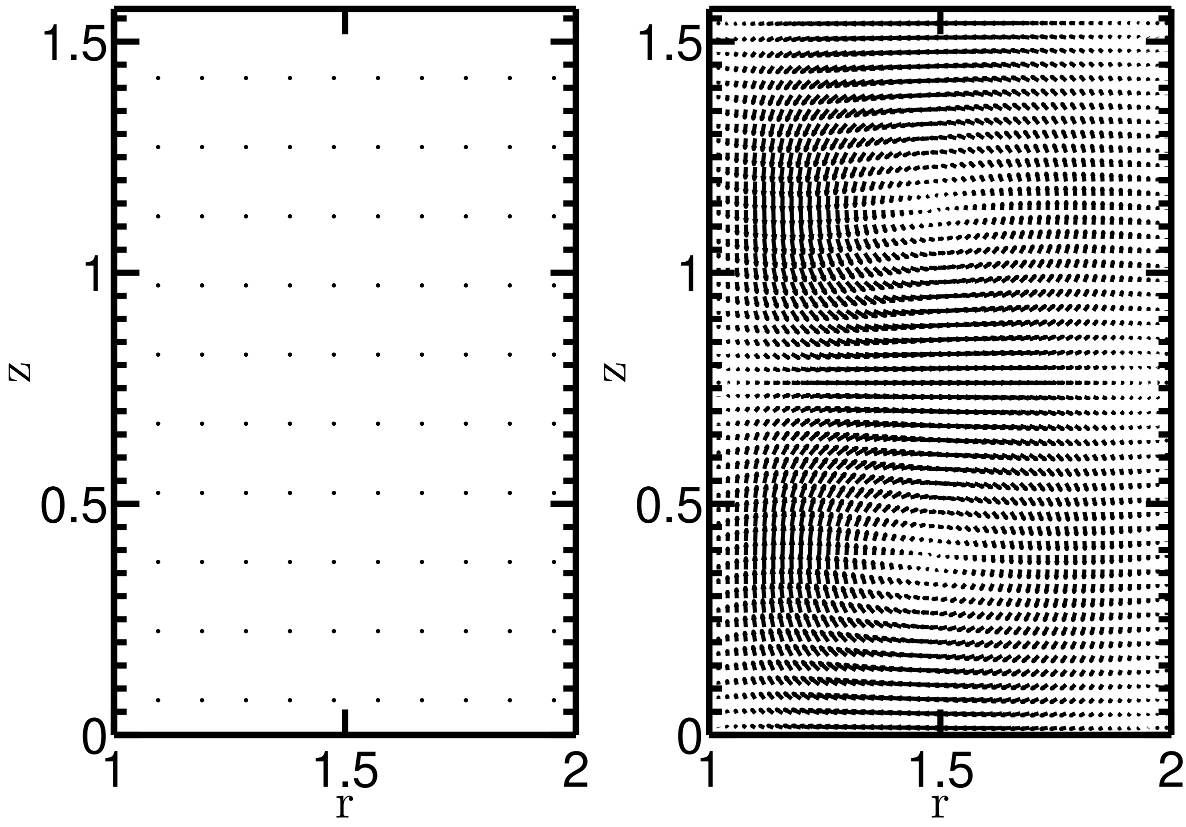

(a) (b)

Fig. 3.5 Velocity vector plots in the (r,z) plane for CCF and TVF: $k = 2\pi/h = 4$, $Ma = 1$ and $Pr = 1$: (a) $Re_1 = 71(< Re_c)$ and (b) $Re_1 = 75(> Re_c)$.

Figure 3.5 shows typical velocity vector plots in the (r,z) plane before and after bifurcation. Figure 3.5a corresponds to the base state circular Couette flow (CCF) while Fig. 3.5b corresponds to the Taylor-vortex flow (TVF).

We choose our computational domain to be of appropriate length in order to accommodate two rolls having opposite sense of circulation. So, while calculating circulation, we assume only two rolls are present that are symmetric about the mid-plane. This assumption is rather restrictive, for if we double the length of the computational domain with the same periodic boundaries in the axial direction, we will get four rolls at the same Reynolds number and not two. The remedy for this restriction is presented at the end of this section. For now, it suffices to assume that there are only two rolls that are symmetric about the mid-plane.

In order to calculate the circulation of a single Taylor roll in a domain of length l, we first need the center of the roll. Because we have assumed that there are only two rolls present,we fix the centers of the rolls are at $z = l/4$ and $z = 3l/4$. The coordinates of the centers of the rolls on the computational grid can now be easily found.

For the purpose of plotting the bifurcation diagram, we will calculate the circulation about the upper roll. Because of symmetry, the circulation of the lower roll will be negative of that of the upper roll.

The procedure is as follows:

1. Isolate the center of the upper roll.
2. Define several rectangular loops around the center.
3. For each loop, calculate the quantity

$$\Gamma_c = \oint \underline{u} \cdot \underline{dl} \tag{3.56}$$

4. If N is the number of loops, the average circulation (henceforth called just circulation for brevity)

$$C = \frac{\Sigma(\Gamma_c)}{N} \tag{3.57}$$

5. Plot circulation (C) versus Re_1 for the constant and variable viscosity cases, see Fig. 3.6.

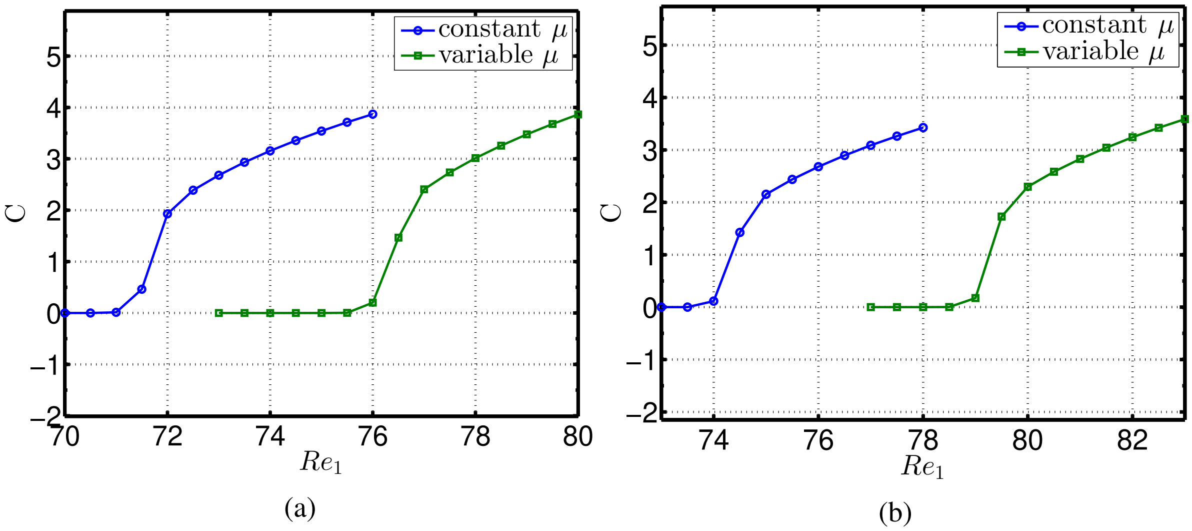

(a)

(b)

Fig. 3.6 Average circulation versus Re_1 with $Ma = 1$ and $Pr = 1$ for constant and variable viscosity for different heights ($= 2\pi/k$) of the computational domain: (a) $k = 3.1729$ and (b) $k = 4$.

3.6.4 Radial Average of Radial Velocity versus z - Comparison

Another metric to quantify bifurcation can be the maximum of the r-averaged radial velocity. We take the average with respect to r at a given z and get a number. We plot these r-averaged values of the radial velocity versus z. In the base state, when the circular Couette flow is present, $u_0 = 0$. Hence the radial average of the base-state radial velocity is zero. However, when the flow bifurcates to TVF, radial velocity is obviously non-zero, due to presence of Taylor rolls. The axial variation of the radial a average of u is shown in Fig. 3.7. For lower Re_1, in the circular Couette regime, Fig. 3.7 shows no variation in axial direction, giving a constant line at $< u >_r = 0$.

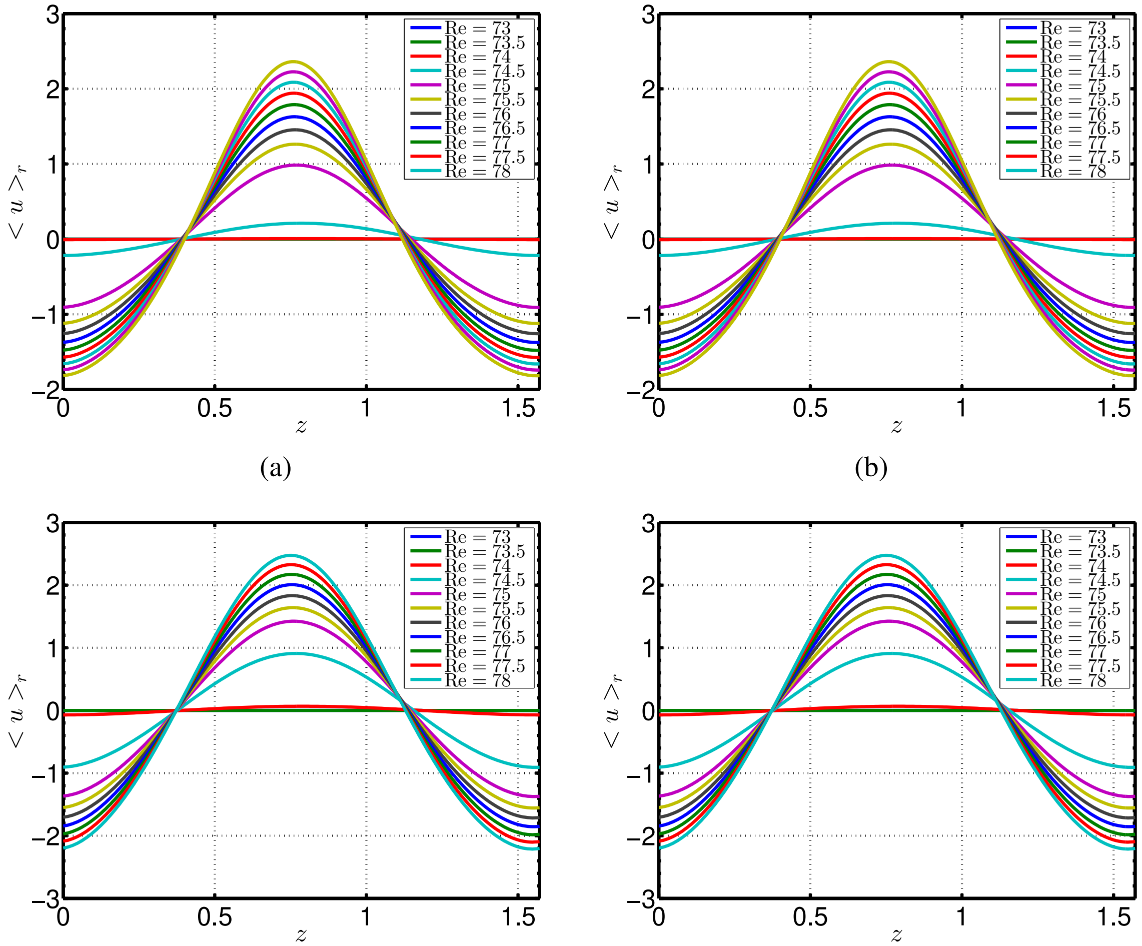

(a) (b)

(c) (d)

Fig. 3.7 r-averaged values of the radial velocity versus z: (a) $k = 3.1729$, constant μ, (b) $k = 3.1729$, variable μ,(c) $k = 4$, constant μ, (d) $k = 4$, variable μ.

However, at higher Re_1, TVF appears. A schematic of how $< u >_r$ varies with axial height is given in Fig. 3.8. The black colored arrows denote the flow while the red lines indicate different axial locations. Initially, $< u >_r$ increases from a negative to a positive value with increasing z and then decreases to a negative value with increasing z as shown in Fig. 3.8. The zero-crossings of the axial profile of $< u >_r$ correspond to the centers of the Taylor rolls. The actual axial profiles of $< u >_r$ are plotted in Fig. 3.7, with different values of k and Re_1 for both constant and variable viscosity cases.

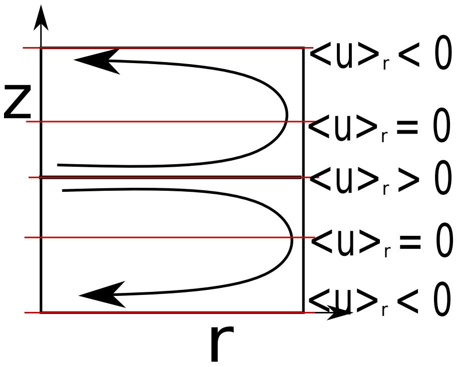

Fig. 3.8 Schematic of the axial profile of $< u >_r$

We define Δu to be the maximum value for each curve (Fig. 3.7) and plot Δu vs Re_1 to get the bifurcation diagram shown in Fig. 3.9. It is clear that the onset of bifurcation in Fig. 3.9 is almost same as that predicted via circulation in Fig. 3.6.

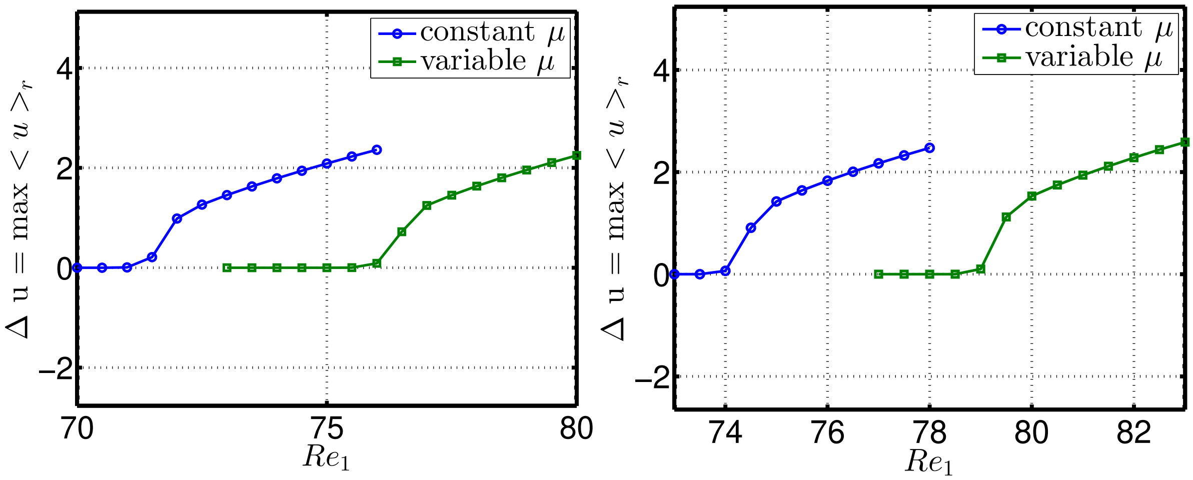

(a) (b)

Fig. 3.9 r-averaged u vs Re_1 comparison for constant and variable viscosity for different heights $(= 2\pi/k)$ of the computational domain with $Ma = 1$, $Pr = 1$, (a) $k = 3.1729$ and (b) $k = 4$.

3.6.5 Specific Angular Momentum

Consider a blob of fluid of volume dV, at radius r; its moment of inertia is

$$\mathscr{I} \sim (dm)r^2.$$

Its angular momentum is $\mathscr{L} \sim (\rho(r)dV)r^2\left(\frac{v}{r}\right)$, where v is the azimuthal velocity, i.e.,

$$\mathscr{L} \sim (\rho(r)dV)rv,$$

Therefore the specific angular momentum $\mathscr{L}_s$ is

$$\mathscr{L}_s \sim \rho(r)vr. \tag{3.58}$$

We will plot contours of $\mathscr{L}_s$, to get insight into how angular momentum changes. It also tells us whether we are above or below the Rayleigh line, respecting the inviscid instability criterion due to Rayleigh [33].

3.6.6 Local Mach Number

We define the local speed of sound as follows:

$$cs_{local} = \sqrt{\frac{\gamma R}{M_g} T_{local}} \tag{3.59}$$

where

- R is the universal gas constant = 8.314 J/mol-K,
- M_g is the molecular weight of the gas, taken here to be air ≈ 28.8 g/mol $\approx 28.8 \times 10^{-3}$ kg/mol,
- T_{local} is the dimensional temperature at a point, in K.

To get the dimensional temperature, we simply multiply the non-dimensional temperature by the temperature at the inner wall $T|_{R_1}$, assumed to be the room temperature, $300K$.

$$T^* = (T)T|_{R_1} \tag{3.60}$$

where T is the dimensionless temperature at the concerned point.
The local Mach number Ma_{local} is defined as:

$$Ma_{local} = \frac{v}{cs_{local}} \tag{3.61}$$

where v is the azimuthal velocity in dimensional form. The units of velocity are $\mu_R^*/(\rho_R^* d)$. To extract the velocity scale, we do the following calculation. The non-dimensional isothermal speed of sound is

$$c_s^2 = (c_p - c_v)(\rho_R^*)^2 T_R^* d^2/(\mu_R^*)^2 \tag{3.62a}$$

and

$$c_s = Re_1/Ma, \tag{3.62b}$$

where Re_1 is as defined as $Re_1 = \frac{\Omega_1 R_1 \rho_R^* d}{\mu_R^*}$. For a given Re_1 and Ma, Eqn. (3.62b) determines the dimensionless isothermal speed of sound. T^*, the dimensional temperature can be calculated using Eqn. (3.60) and $c_p - c_v$ is known for a given compressible gas. Hence, inverting Eqn. (3.62a) gives us the velocity scale.

$$\begin{aligned} &\mu_R^*/(\rho_R^* d) \\ &= \sqrt{(c_p - c_v)T^*}/c_s \\ &= (\sqrt{(c_p - c_v)T^*})Ma/Re_1 \end{aligned} \tag{3.63}$$

Here, we take $c_p = 1005 J/kg - K \Rightarrow c_v = c_p/\gamma = 603 J/kg - K$
$\Rightarrow (c_p - c_v) = 402 J/kg - K$.
Therefore,

$$\begin{aligned} &\mu_R^*/(\rho_R^* d) \\ &= (\sqrt{(c_p - c_v)T^*})Ma/Re_1 \\ &= (\sqrt{402 \times 300})Ma/Re_1 \\ &= (347.275)Ma/Re_1 \end{aligned} \tag{3.64}$$

We multiply the nondimensional azimuthal velocity by the above expression to get the dimensional azimuthal velocity and substitute in Eqn. (3.61) to obtain the local Mach number.

3.6.7 Procedure to Analyze Bifurcation

The cartoon in Fig. 3.10 summarizes the procedure to analyze the bifurcation from the featureless circular Couette flow (CCF) to the Taylor-vortex-flow (TVF). The linear stability analysis yields the neutral stability curve which qualitatively looks as the black curve in Fig. 3.10, see Welsh et al. [41] for details. In Fig. 3.10, $k = \frac{2\pi}{\lambda}$ where λ is the wavelength of the fastest growing mode. To observe the bifurcation as we increase the Re_1, we keep the height of the computational domain constant at some λ, making k constant. We then vary Re_1 and plot different fields such as the velocity plot, temperature, density and specific angular momentum contours. Next, we keep Re_1 constant and vary k in the direction of the red arrow as shown. We again plot different quantities to see the transition from the TVF to CCF with increasing k. The red arrows in Fig. 3.10 mark the two paths described above.

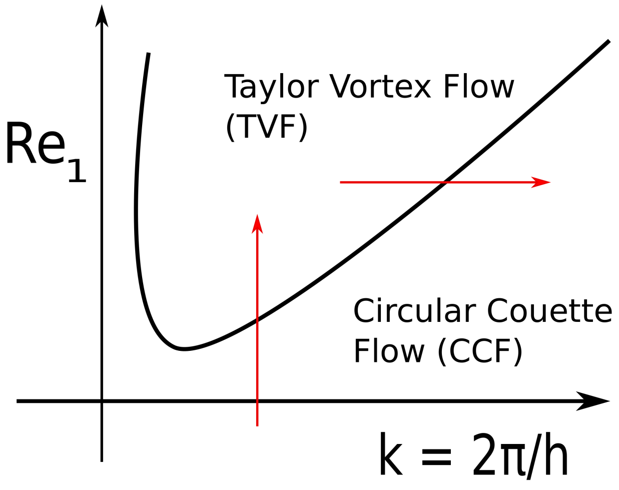

Fig. 3.10 Cartoon of the procedure.

3.6.8 Typical Fields Before and After Bifurcation - Varying Re_1 at $k = 4$

Here, we follow the vertical red-line in Fig. 3.10 to analyze bifurcation structure. We plot contours of ρ, T and specific angular momentum $\mathscr{L}_s$ at different Re_1, with k being set equal to 4 (i.e., $\Gamma = h/d = \pi/2$ and the Mach number $Ma = 1$. The results for the (i) constant viscosity and (ii) variable viscosity models are shown in Fig. 3.11 and Fig. 3.12, respectively. The top panels in each figure represent CCF whereas the bottom panels display TVF.

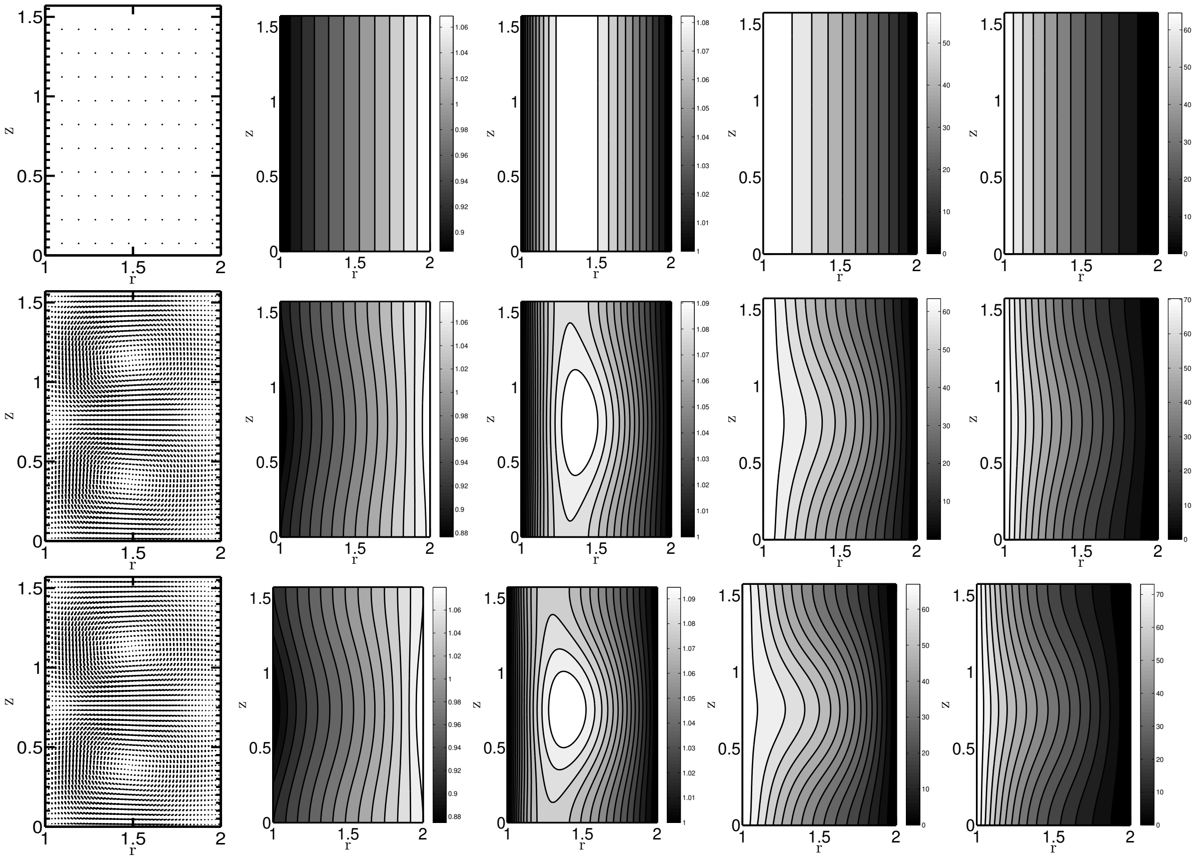

(a) (b) (c) (d) (e)

Fig. 3.11 Constant viscosity: First panel: $Re_1 = 71$, Second panel: $Re_1 = 75$, Third panel: $Re_1 = 78$. (a) velocity plot, (b) ρ, (c) T, (d) $\mathscr{L}_s$, (e) azimuthal velocity (v).

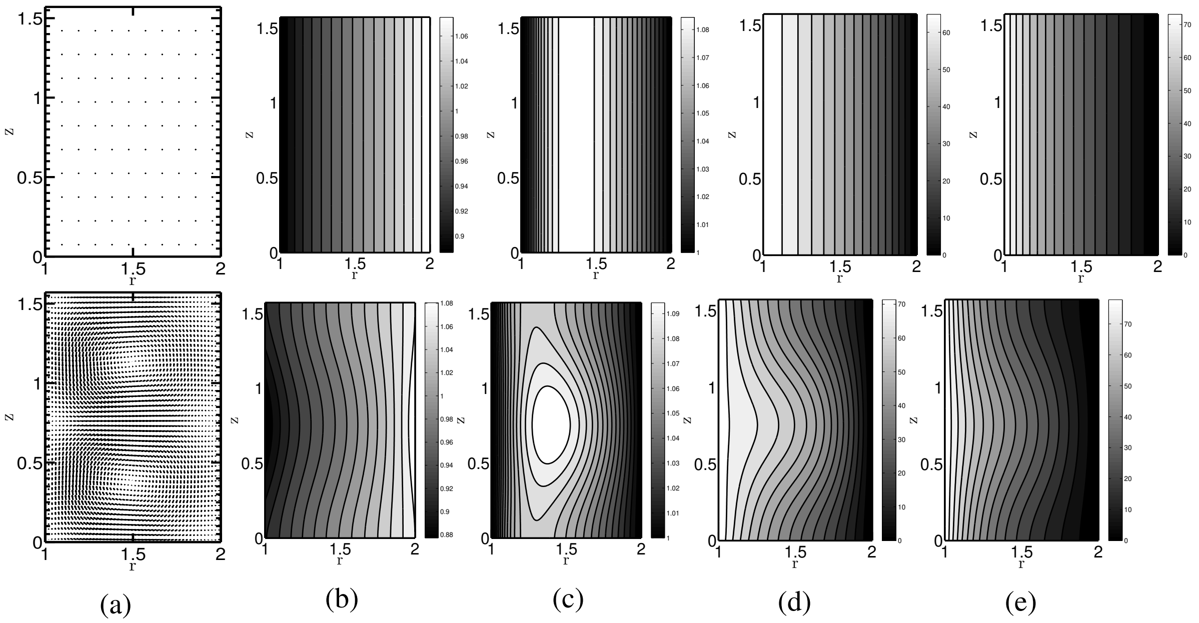

Fig. 3.12 Variable viscosity: First panel: $Re_1 = 78$, Second panel: $Re_1 = 83$. (a) velocity plot, (b) ρ contours, (c) T contours, (d) $\mathscr{L}_s$ contours, (e) azimuthal velocity (v) contours.

3.6.9 Varying Height of the Computational Domain, at $Re_1 = 100$

Here, we follow the horizontal red-line in Fig. 3.10 to analyze bifurcation scheme. We plot velocity plot, ρ, T , $\mathscr{L}_s$, v and local Ma contours respectively for the varying height of the computational domain. The results for the (i)constant viscosity and (ii)variable viscosity models are shown in Fig. 3.13 and Fig. 3.14, respectively. Recall that the aspect-ratio Γ is given by $\Gamma = 2\pi/k$.

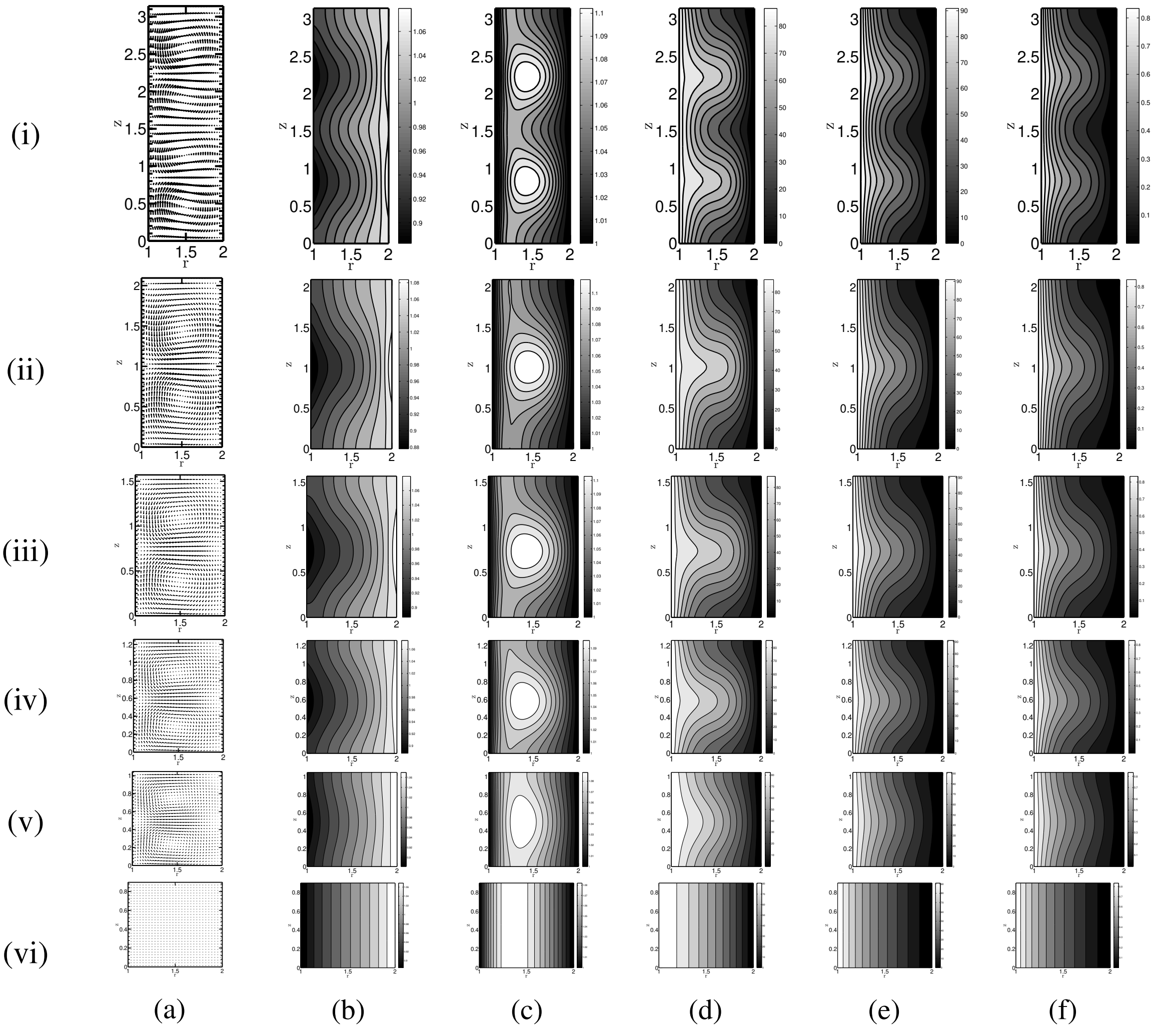

Fig. 3.13 $Re_1 = 100, Re_2 = 0$, constant viscosity, (i) $k = 2$, (ii) $k = 3$, (iii) $k = 4$, (iv) $k = 5$, (v) $k = 6$, (vi) $k = 7$, (a) velocity plot, (b) ρ contours, (c) T contours, (d) $\mathscr{L}_s$ contours, (e) azimuthal velocity v contours (f) local Ma contours.

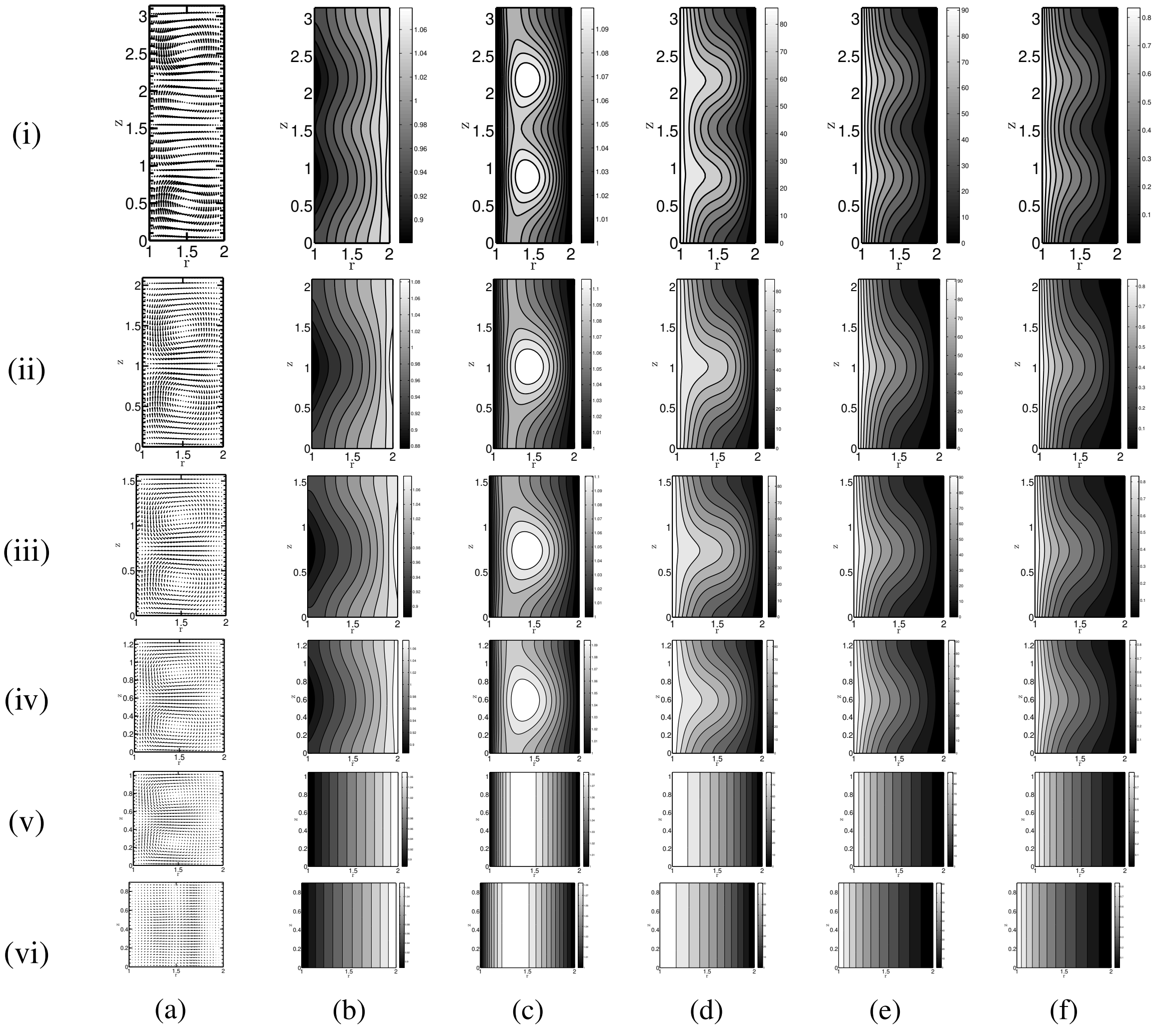

Fig. 3.14 $Re_1 = 100, Re_2 = 0$, variable viscosity, (i) $k = 2$, (ii) $k = 3$, (iii) $k = 4$, (iv) $k = 5$, (v) $k = 6$, (vi) $k = 7$. (a) velocity plot, (b) ρ contours, (c) T contours, (d) $\mathscr{L}_s$ contours, (e) azimuthal velocity v contours (f) local Ma contours.

Comparing Fig. 3.13 and Fig. 3.14, we find that the critical k for transition from the TVF to CCF **decreases** for the variable viscosity case. The flow patterns, however, look similar for both cases.

3.7 Results at Higher Reynolds Numbers

As the Re_1 is increased in the numerical experiments, it was observed that the Taylor vortex flow bifurcates to a traveling wave. In the standard Taylor-Couette experiments, it is well known that the Taylor vortex flow bifurcates to wavy vortex flow. In the wavy vortex flow, waves develop on the Taylor vortices in the ϕ direction and the whole structure starts rotating in the ϕ direction at some speed. However, because the current code imposes **axisymmetry**, the flow is seen to bifurcate to an axisymmetric wave traveling in the negative z-direction. The oscillations are evident from the KE_u and KE_w versus t graphs. In this section, we show various fields as a function of time as well as corresponding kinetic energy graphs over a range of Reynolds numbers. To extract the dominant frequencies and amplitudes of the traveling waves, we take the fast Fourier transform (FFT). Once the dominant dimensionless frequencies are extracted, we plot them against Re_1 to see the effect of increasing Re_1.

3.7.1 $Re_1 = 190$

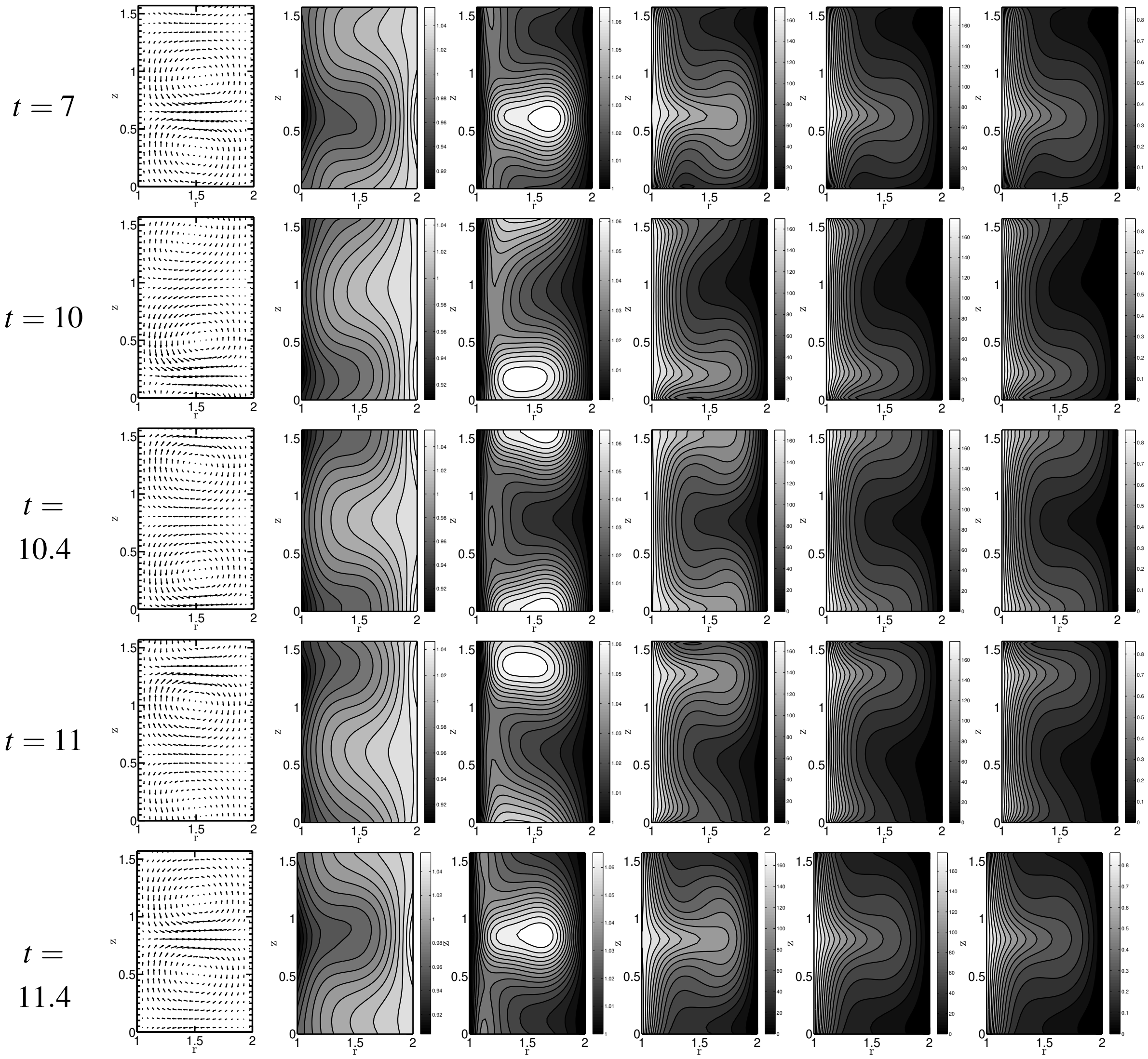

(a) (b) (c) (d) (e) (f)

Fig. 3.15 $Re_1 = 190, Re_2 = 0$, $k = 4$, traveling wave: (a) velocity plot, (b) ρ contours, (c) T contours, (d) $\mathscr{L}_s$ contours, (e) azimuthal velocity v contours (f) local Ma contours.

Some snapshots for traveling-wave at different times are displayed in Fig. 3.15. The oscillations in time are also evident from the kinetic energy versus time plots in Fig. 3.16.

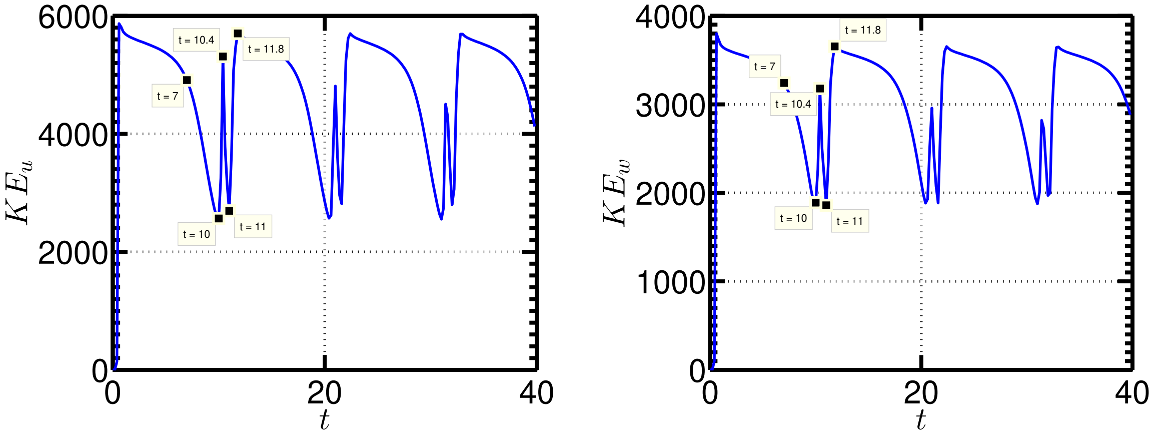

(a) (b)

Fig. 3.16 Time series for kinetic energies, $Re_1 = 190$, traveling wave: (a) KE_u and (b) KE_w. Fig. 3.15 shows snapshots of the flow at the marked points.

In order to extract dominant dimensionless frequencies, fast Fourier transform (FFT) was performed. Mean kinetic energies were subtracted and one-sided amplitudes were plotted in the frequency domain. A clear peak can be seen in Fig. 3.17. A curious observation is that the sub-dominant frequency also has a significant amplitude in comparison with the dominant one.

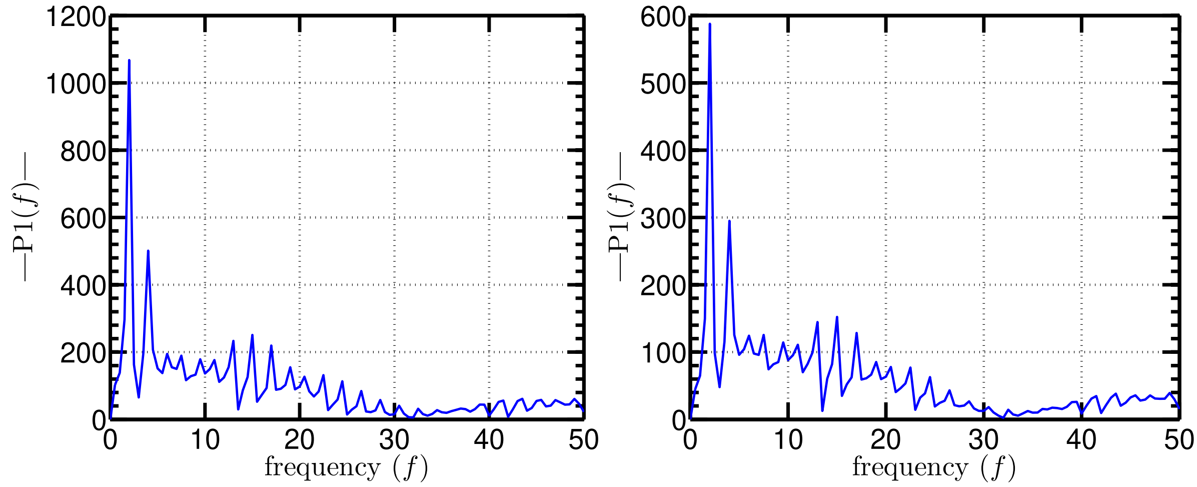

(a) (b)

Fig. 3.17 $Re_1 = 190$, traveling wave, single-sided amplitude spectrum for: (a) KE_u and (b) KE_w.

3.7.2 $Re_1 = 210$

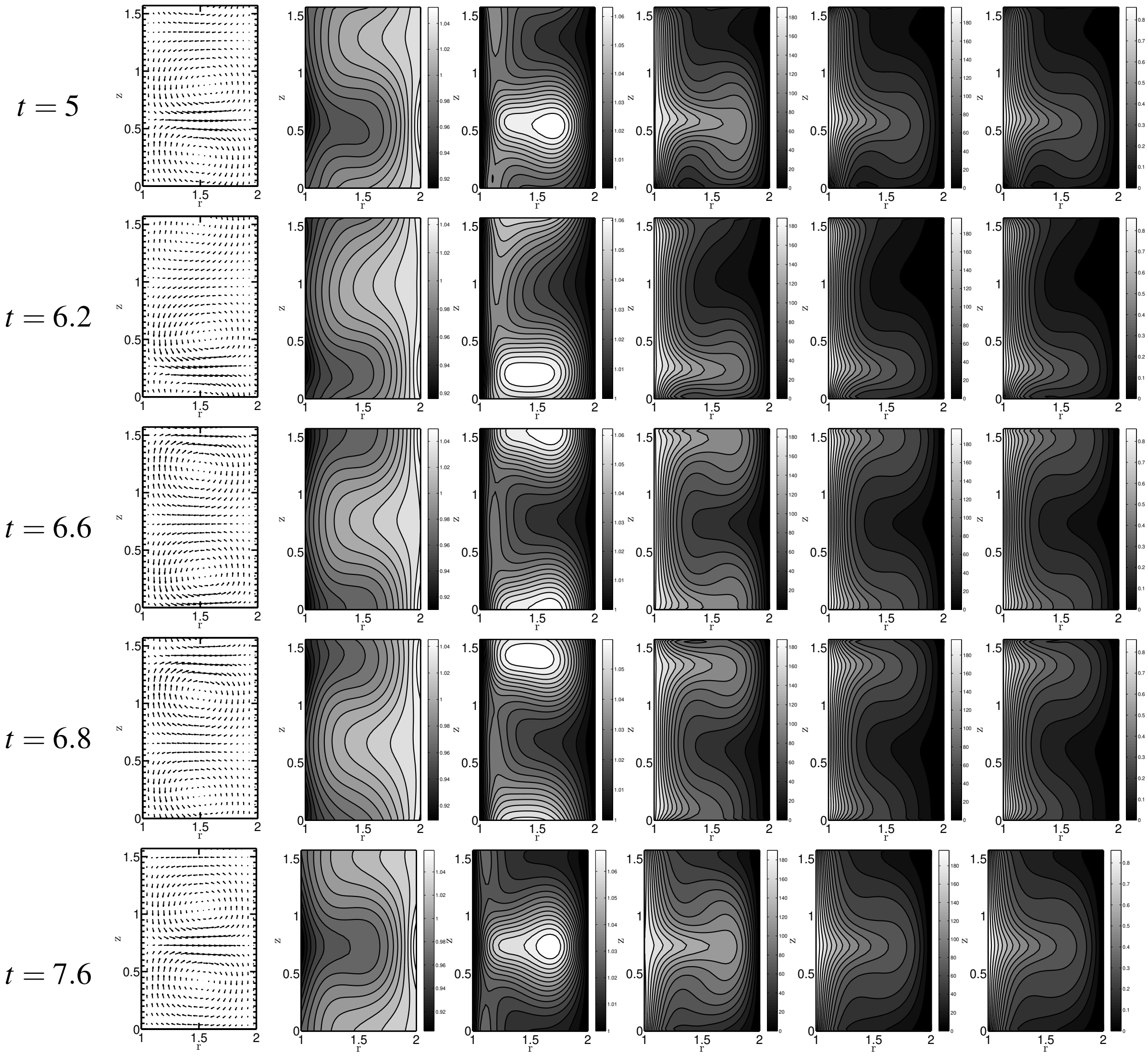

(a) (b) (c) (d) (e) (f)

Fig. 3.18 $Re_1 = 210, Re_2 = 0$, $k = 4$, traveling wave: (a) velocity plot, (b) ρ contours, (c) T contours, (d) $\mathscr{L}_s$ contours, (e) azimuthal velocity v contours (f) local Ma contours.

Fig. 3.18 shows a time-sequence of snapshots of traveling wave at $Re_1 = 210$. The oscillations in time are also evident from the kinetic energy versus time plots in Fig. 3.19.

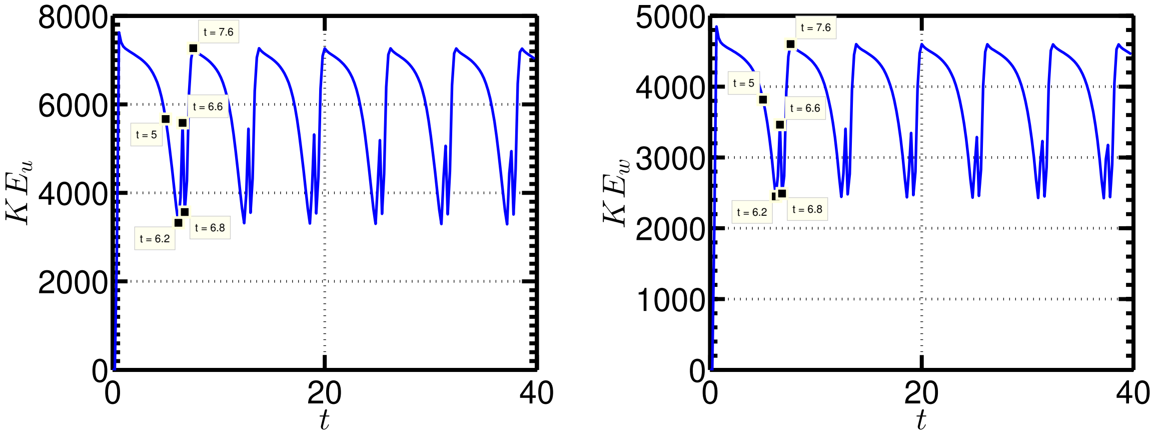

(a) (b)

Fig. 3.19 Time series for kinetic energies, $Re_1 = 210$, traveling wave: (a) KE_u and (b) KE_w. Fig. 3.18 shows snapshots of the flow at the marked points.

In order to extract dominant dimensionless frequencies, fast Fourier transform (FFT) was performed. Mean kinetic energies were subtracted and one-sided amplitudes were plotted in the frequency domain. A clear peak can be seen in Fig. 3.20. Here, the second dominant frequency has comparable amplitude with the dominant one.

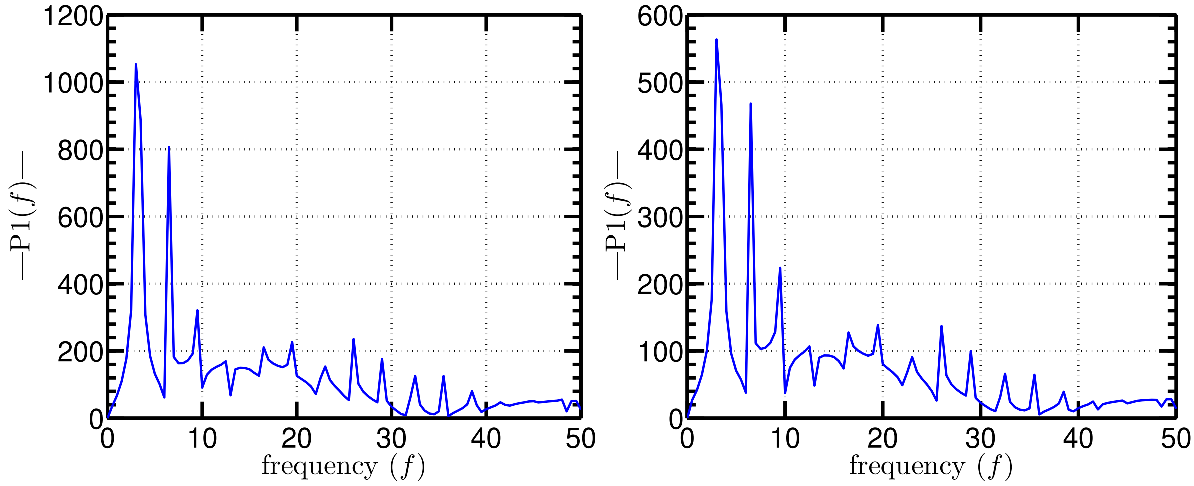

(a) (b)

Fig. 3.20 $Re_1 = 210$, traveling wave, single-sided amplitude spectrum for: (a) KE_u and (b) KE_w.

3.7.3 $Re_1 = 230$

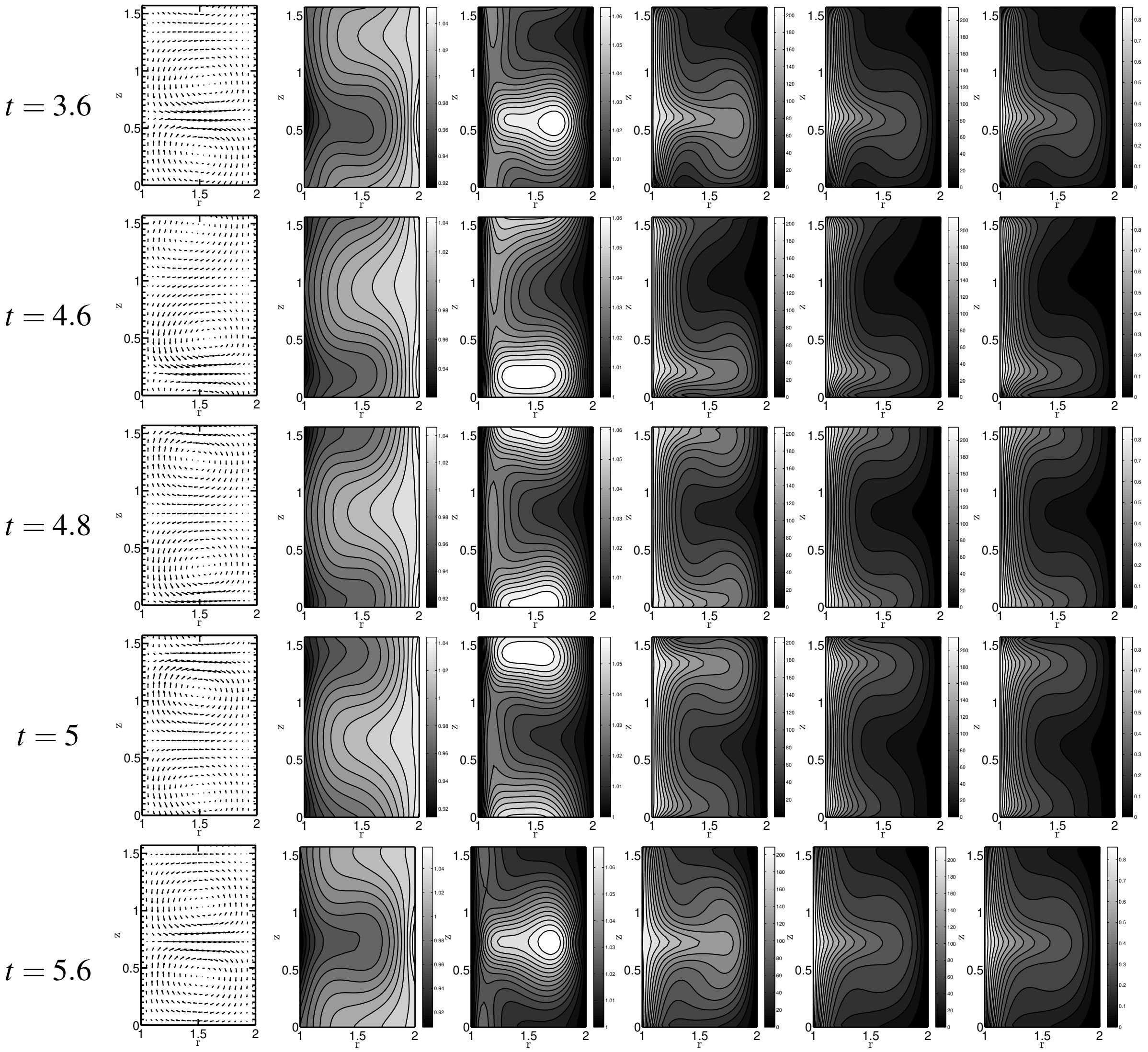

(a) (b) (c) (d) (e) (f)

Fig. 3.21 $Re_1 = 230, Re_2 = 0$, $k = 4$, traveling wave: (a) velocity plot, (b) ρ contours, (c) T contours, (d) $\mathscr{L}_s$ contours, (e) azimuthal velocity v contours (f) local Ma contours.

Fig. 3.21 shows a time-sequence of snapshots at $Re_1 = 230$. The oscillations in time are also evident from the kinetic energy versus time plots in Fig. 3.22.

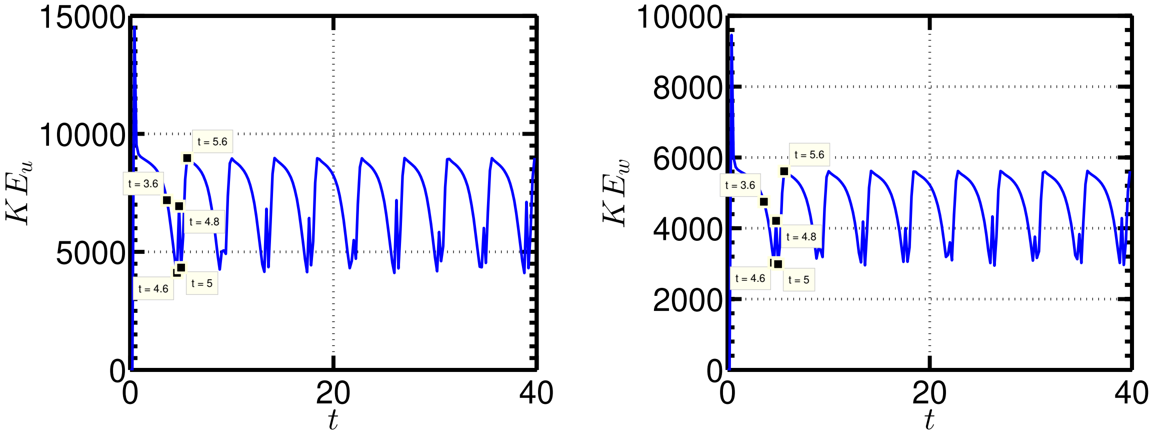

(a) (b)

Fig. 3.22 Time series for kinetic energies, $Re_1 = 230$, traveling wave: (a) KE_u and (b) KE_w. Fig. 3.21 shows snapshots of the flow at the marked points.

In order to extract dominant dimensionless frequencies, fast Fourier transform (FFT) was performed. Mean kinetic energies were subtracted and one-sided amplitudes were plotted in the frequency domain.

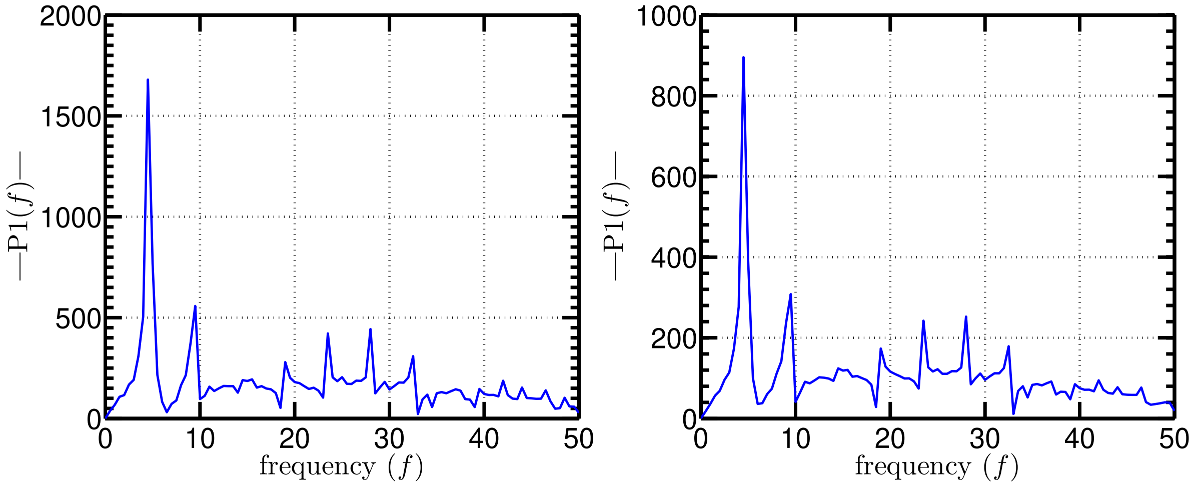

(a) (b)

Fig. 3.23 $Re_1 = 230$, traveling wave, single-sided amplitude spectrum for: (a) KE_u and (b) KE_w.

Two distinct peaks can be seen in Fig. 3.23.

3.7.4 $Re_1 = 250$

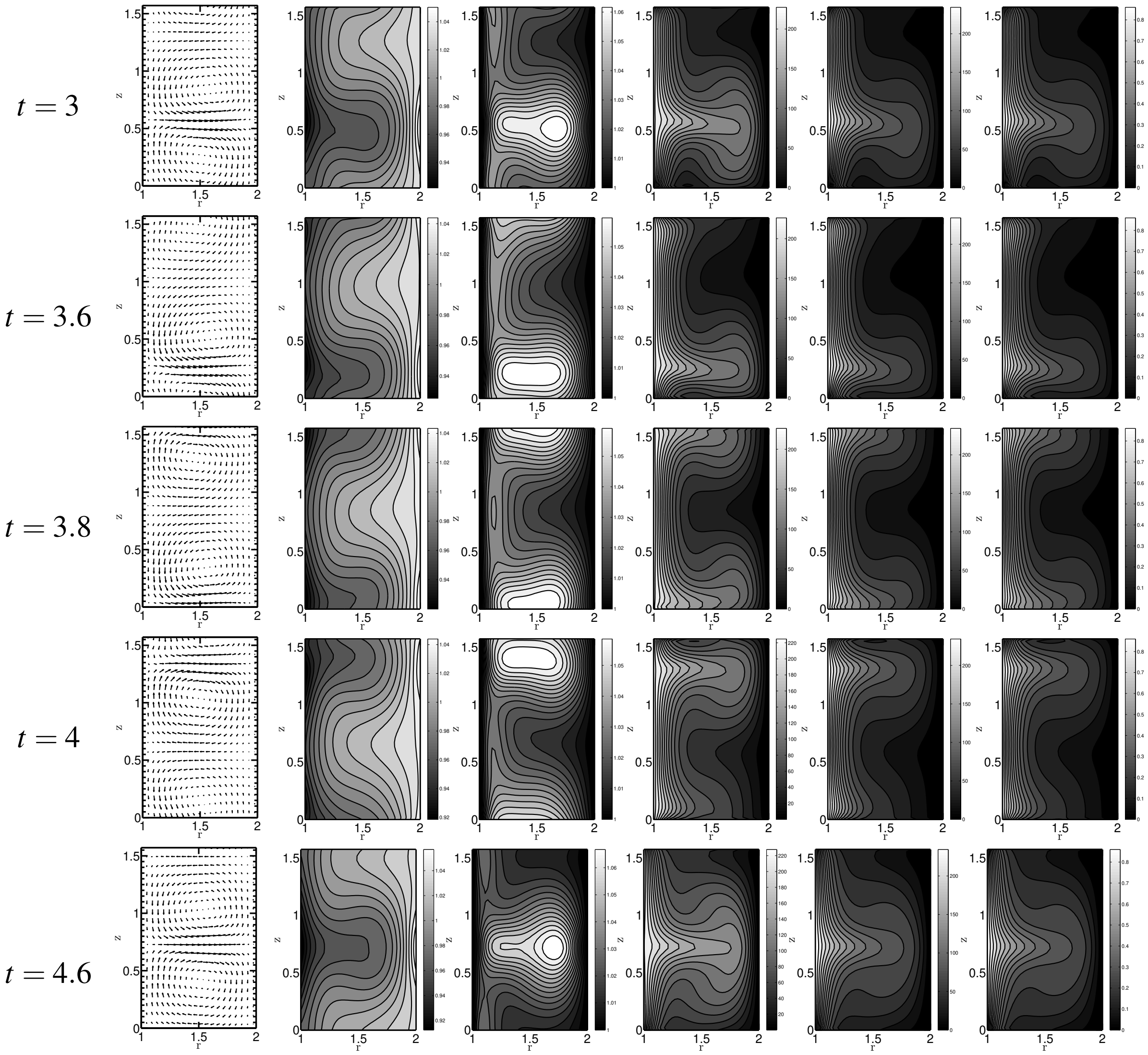

(a) (b) (c) (d) (e) (f)

Fig. 3.24 $Re_1 = 250, Re_2 = 0$, $k = 4$, traveling wave: (a) velocity plot, (b) ρ contours, (c) T contours, (d) $\mathscr{L}_s$ contours, (e) azimuthal velocity v contours (f) local Ma contours.

Figure 3.24 shows a time-sequence of snapshots at $Re_1 = 250$. The oscillations in time are also evident from the kinetic energy versus time plots in Fig. 3.25.

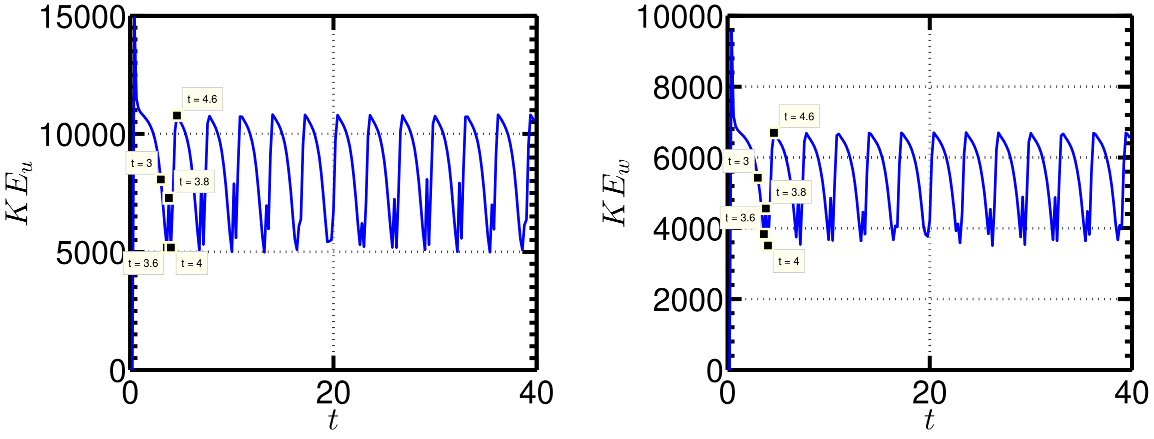

(a) (b)

Fig. 3.25 Time series for kinetic energies, $Re_1 = 250$, traveling wave: (a) KE_u and (b) KE_w. Fig. 3.24 shows snapshots of the flow at the marked points.

In order to extract dominant dimensionless frequencies, fast Fourier transform (FFT) was performed. Mean kinetic energies were subtracted and one-sided amplitudes were plotted in the frequency domain. A clear peak can be seen in Fig. 3.26.

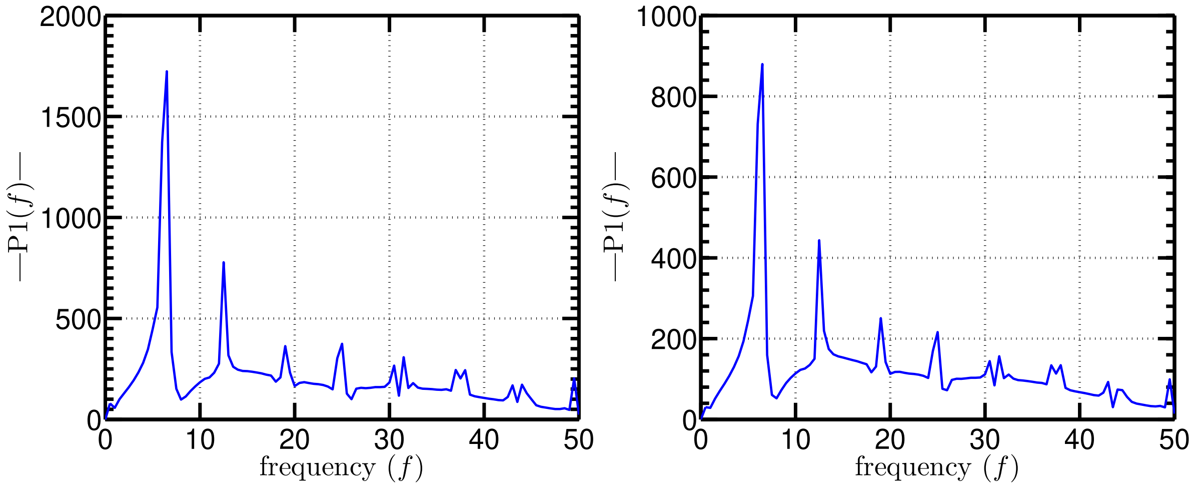

(a) (b)

Fig. 3.26 $Re_1 = 250$, traveling wave, single-sided amplitude spectrum for: (a) KE_u and (b) KE_w.

3.7.5 $Re_1 = 270$

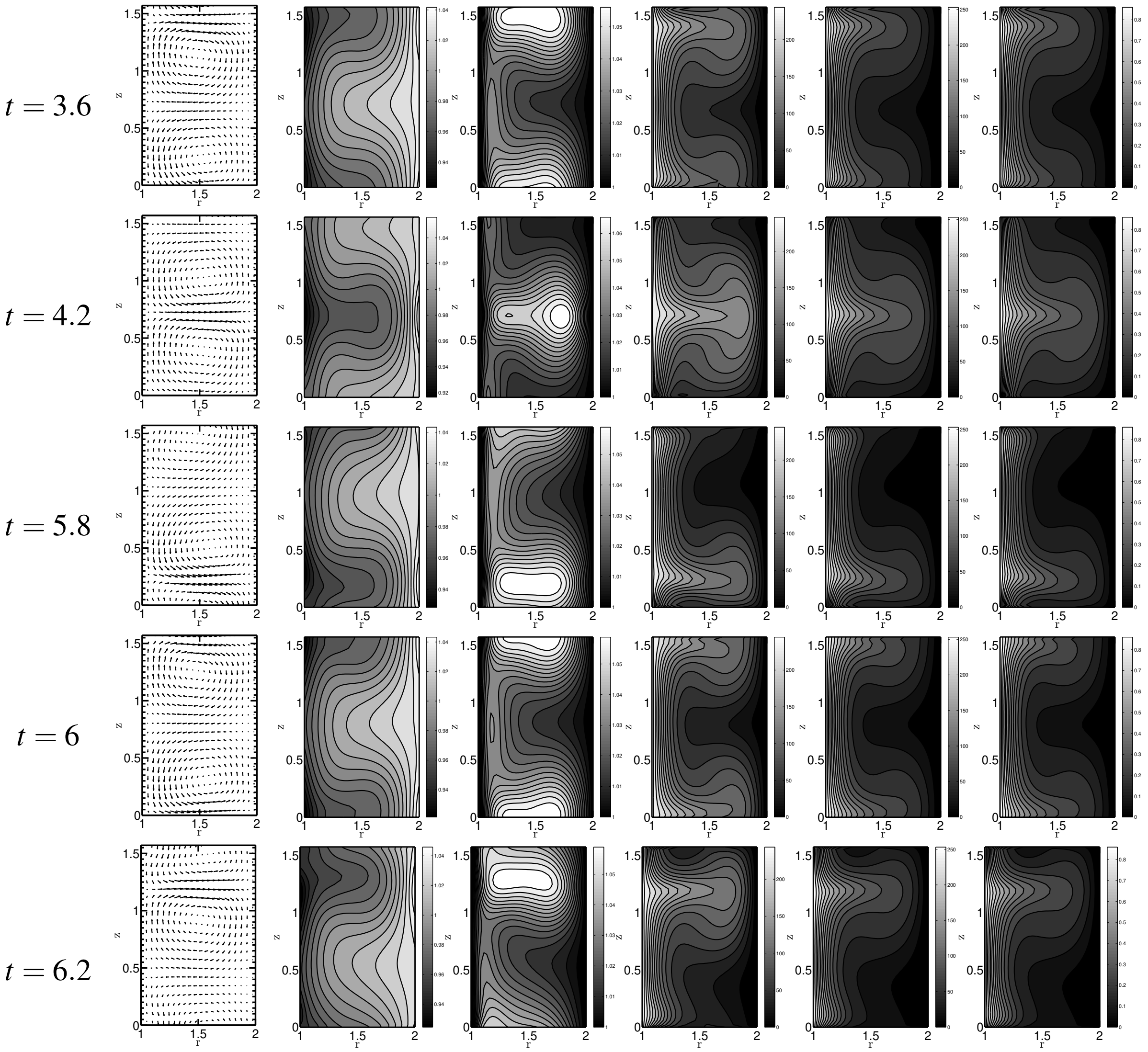

(a) velocity (b) (c) (d) (e) (f)

Fig. 3.27 $Re_1 = 270, Re_2 = 0$, $k = 4$, traveling wave: (a) velocity plot, (b) ρ contours, (c) T contours, (d) $\mathscr{L}_s$ contours, (e) azimuthal velocity v contours (f) local Ma contours.

A time-sequence of snapshots of the traveling wave is shown in Fig. 3.27. The oscillations in time are also evident from the kinetic energy versus time plots in Fig. 3.28.

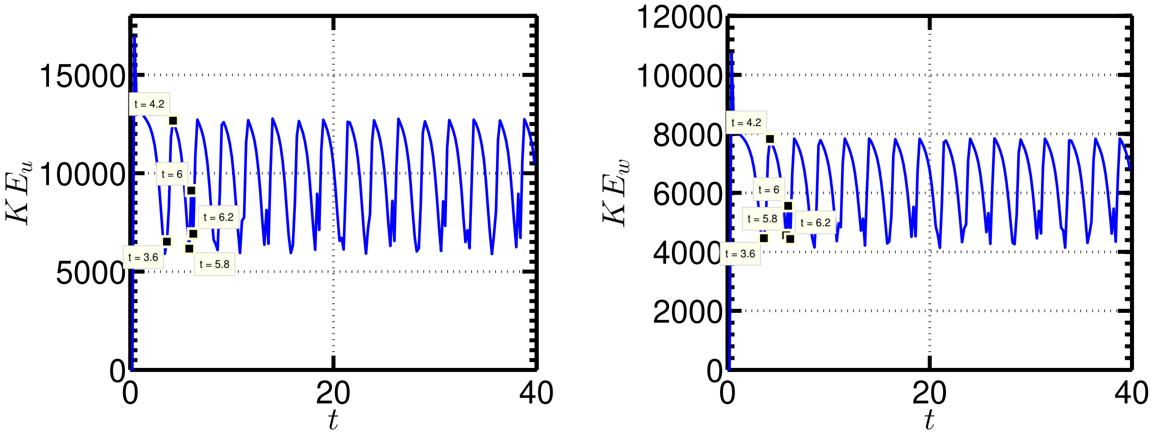

(a) (b)

Fig. 3.28 Time series for kinetic energies, $Re_1 = 270$, traveling wave: (a) KE_u and (b) KE_w. Fig. 3.27 shows snapshots of the flow at the marked points.

In order to extract dominant dimensionless frequencies, fast Fourier transform (FFT) was performed. Mean kinetic energies were subtracted and one-sided amplitudes were plotted in the frequency domain. A clear peak can be seen in Fig. 3.29. The amplitudes of the second dominant frequency are almost insignificant than the dominant one.

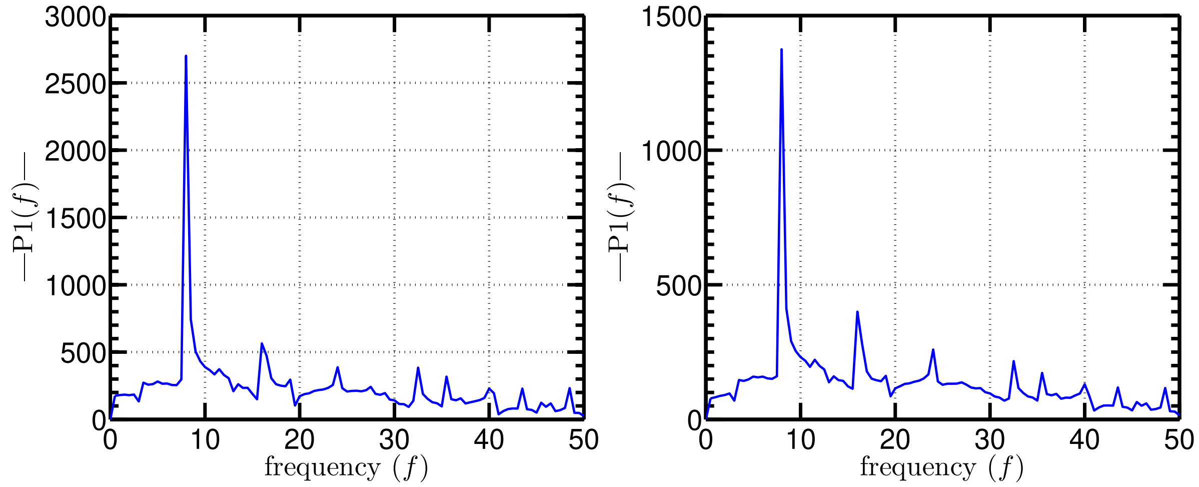

(a) (b)

Fig. 3.29 $Re_1 = 270$, traveling wave, single-sided amplitude spectrum for: (a) KE_u and (b) KE_w.

3.7.6 Plotting Dominant Frequencies and Amplitudes against Re_1

In this section, we plot the dominant as well as second-dominant frequencies and amplitudes obtained from the power spectrum data. We also convert the dimensionless frequencies from viscous time-scale to the inertial time scale in order to gain insight about their variation with the velocity of the inner cylinder. Results of this section are given in table - (3.2) and (3.3) and plotted in Fig. 3.30 and Fig. 3.31.

Re_1	f_{max}	$(P1(f))_{max}$ for KE_u	$(P1(f))_{max}$ for KE_w
190	2	1067.8	587.8004
210	3	1052.7	563.3510
230	4.5	1680.1	895.5590
250	6.5	1723.7	879.7941
270	7.5	2701.3	1374.8

Table 3.2 Higeher Re_1: dominant frequencies and amplitudes

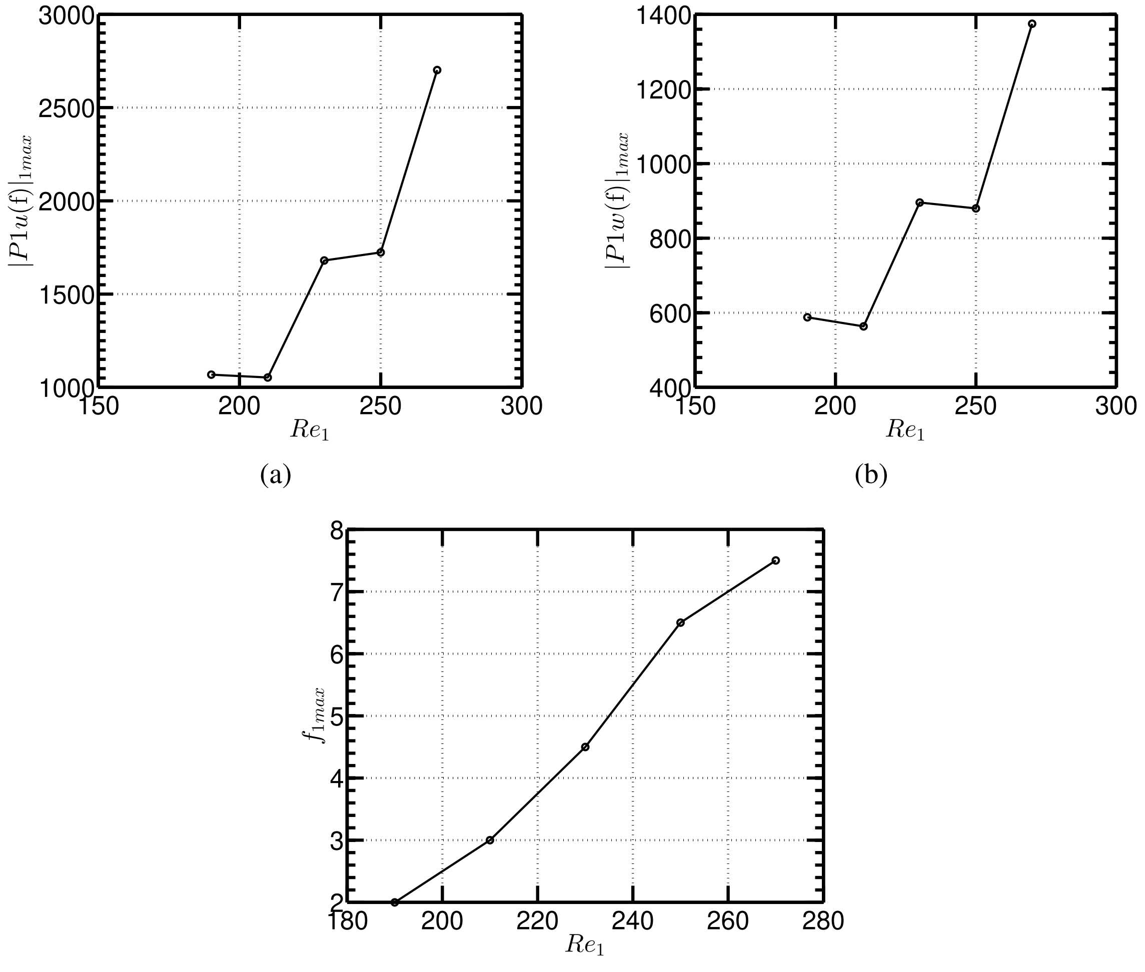

(a) (b)

(c)

Fig. 3.30 Dominant Amplitudes (a,b) and Frequencies (c) for KE_u and KE_w versus Re_1: (a) Dominant amplitude versus Re_1 for Ke_u, (b) Dominant amplitude versus Re_1 for Ke_w, (c) Dominant frequency versus Re_1.

We also summarize the second dominant frequencies and corresponding amplitudes for KE_u and KE_w

Re_1	f_{2max}	$(P1(f))_{2max}$ for KE_u	$(P1(f))_{2max}$ for KE_w
190	4	501.2369	294.8943
210	6.5	806.4684	467.9420
230	9.5	557.7179	308.3439
250	12.5	778.1974	443.4739
270	16	564.8850	400.1247

Table 3.3 Higeher Re_1: second dominant frequencies and amplitudes

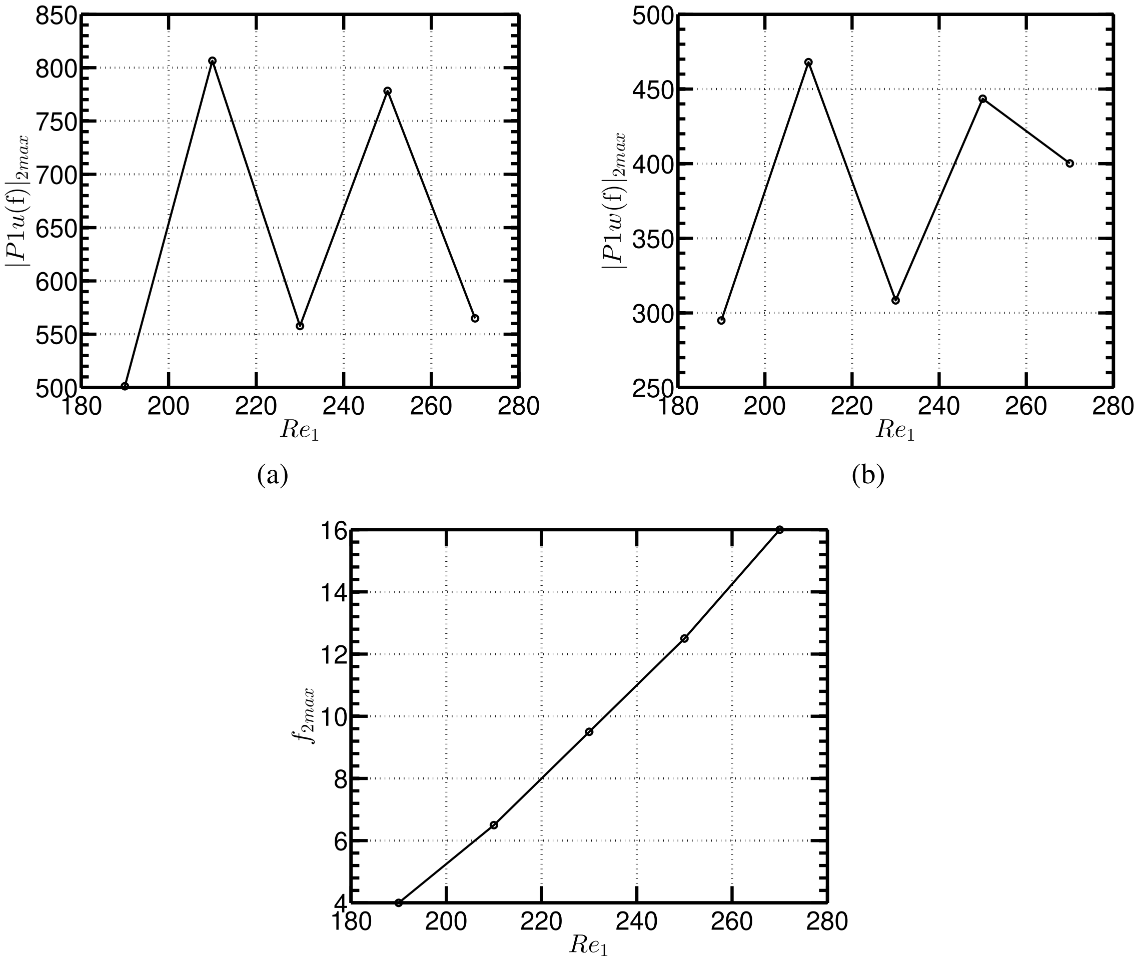

(a) (b)

(c)

Fig. 3.31 Second dominant Amplitudes (a,b) and Frequencies (c) for KE_u and KE_w versus Re_1: (a) Second dominant amplitude versus Re_1 for Ke_u, (b) Second dominant amplitude versus Re_1 for Ke_w, (c) Second dominant frequency versus Re_1.

In Fig. 3.30 and Fig. 3.31, the frequencies are on the viscous time-scale, owing to our choice of characteristic time-scale for non-dimensional time. In order to convert the frequencies on the inertial time-scale, based on the rotation of the inner cylinder, we do a simple calculation. In what follows, let $f_{viscous}$ be dimensionless frequency on the viscous time-scale, $f_{inertial}$ be the dimensionless frequency on the inertial time-scale and f^* be the dimensional frequency.

$$f^* = f\frac{\mu^*}{\rho^* d} \tag{3.65}$$

$$\begin{aligned} f_{inertial} &= f^*/\Omega_1 \\ &= f\frac{\mu^*}{\rho^* d\Omega_1} \\ &= \frac{f}{Re_1}\left(\frac{1-\eta}{\eta}\right) \end{aligned} \tag{3.66}$$

We plot the first and second dominant frequencies versus Re_1 in Fig. 3.32 in order to understand how frequencies vary with the rotation rate of the inner cylinder.

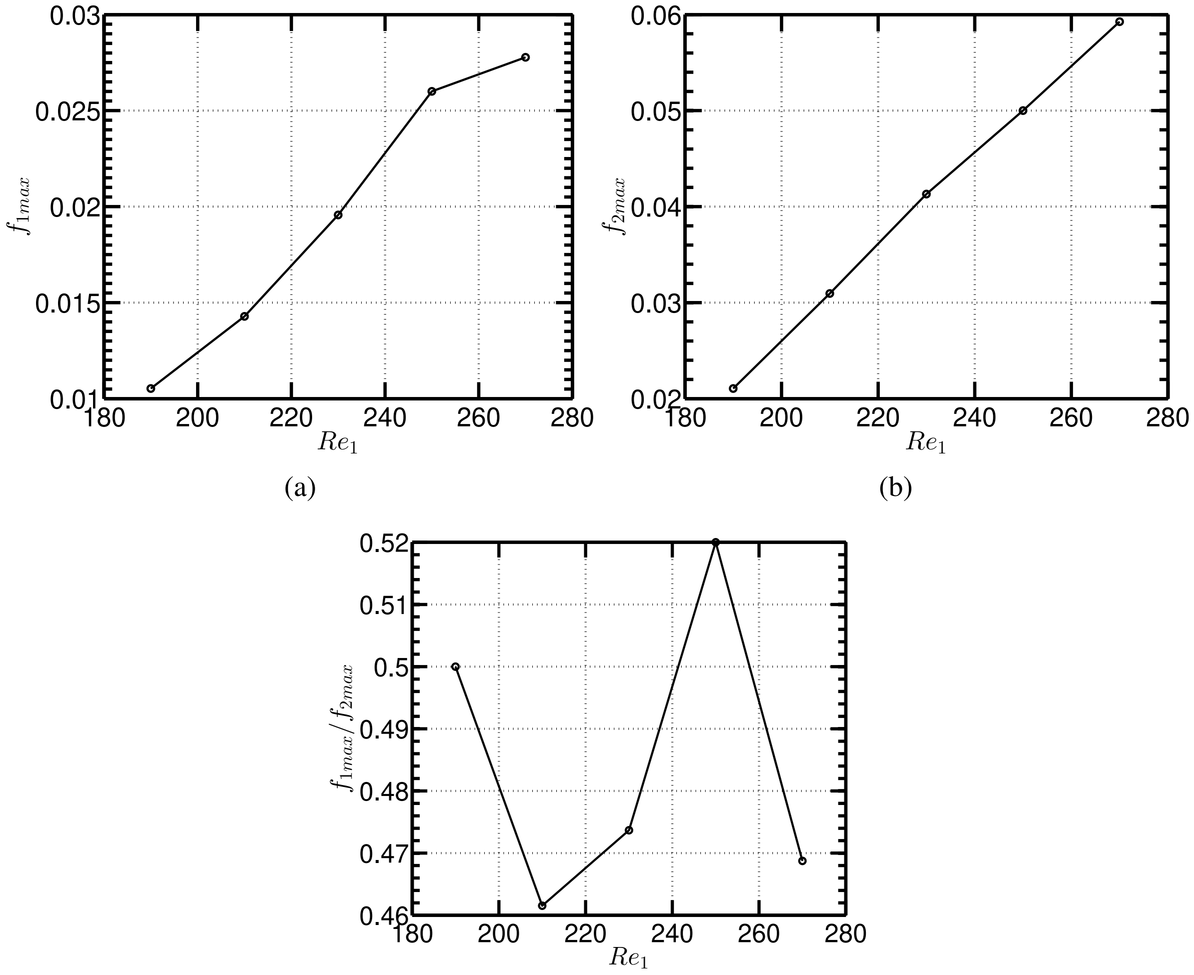

(a) (b)

(c)

Fig. 3.32 (a) First dominant frequency versus Re_1, (b) second-dominant frequency versus Re_1 and (c) ratio of f_{1max} and f_{2max} versus Re_1 on inertial time-scale.

From Fig. 3.32c, the ratio of the first and second dominant frequencies appears to be 0.5 with some tolerance.

3.8 Summary and Conclusion

The chapter began with writing dimensionless equations and boundary conditions for the Taylor-Couette flow. Characteristic quantities for nondimentionalization are so chosen that numerical results can be compared with experiments [Welsh et al. [41]]. Another verification of the code is presented by matching the analytically known base state with the one obtained from long-time marching.

The effect of variable viscosity on the onset of Taylor vortex flow is examined. The variation of viscosity as a function of temperature is described by the well known Sutherland's law of shear viscosity. To quantify the bifurcation from the Couette flow to the Taylor vortex flow, average circulation of the upper roll is plotted against the Reynolds number. The procedure to calculate the average circulation is also described. Another bifurcating quantity is the maximum radially averaged radial velocity when plotted against axial distance, denoted by Δu. Δu versus Re_1 is plotted to quantify the onset of bifurcation, where Re_1 is the Reynolds number based on the rotation of the inner cylinder. It is observed that the critical Re_1 **increases** in the case of variable viscosity, which implies variable viscosity **stabilizes** the flow. Typical fields such as velocity plot and contours of density, temperature, specific angular momentum and azimuthal velocity are plotted as Re_1 is varied. It is seen that before bifurcation, there are no axial gradients in the contours of the above quantities, whereas after the flow bifurcates to the Taylor vortex flow, axial gradients start to develop. The same exercise is repeated keeping Re_1 fixed and changing the height of the computational domain.

At higher Reynolds numbers, a new interesting behavior is revealed. An axisymmetric wave traveling in the negative z direction is observed. Numerical experiments were done for a range of Re_1. The average kinetic energies based on radial and axial velocities are plotted which show oscillations in time. In order to extract the dominant frequencies, a fast Fourier transform (FFT) is done. The dominant frequencies and amplitudes were extracted and plotted against Re_1 to see the effect of increasing Re_1. It was found that although the dominant frequency increases with increasing Re_1, it is **not** a linear function of Re_1.

Chapter 4

Finite-Size Effects and Anomalous Modes

"In my case, most things of lasting value came from doing things that I was not supposed to do."
- Predrag Cvitanović.

4.1 Introduction

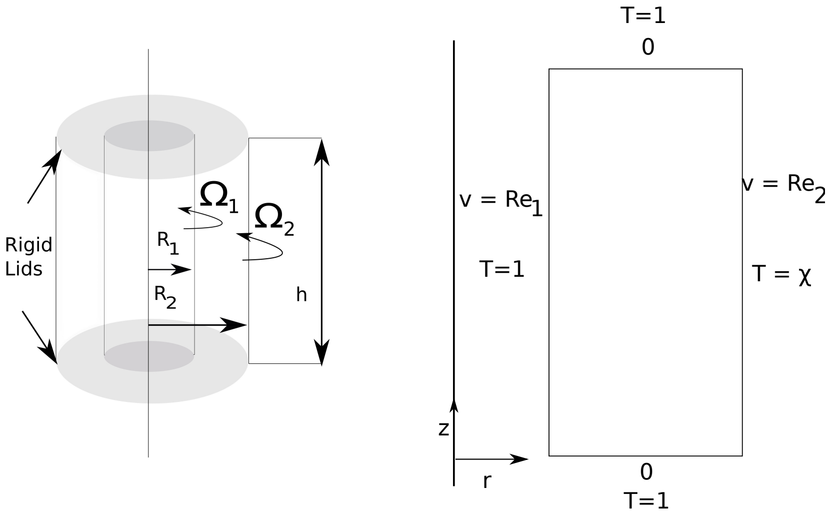

(a) (b)

Fig. 4.1 (a) Finite-cylinders geometry and (b)dimensionless boundary conditions for TCF with rigid lids at top and bottom.

Figure 4.1 shows the geometry and the dimensionless boundary conditions for a finite-cylinder case for TCF. In a finite sized container, because of no-slip boundary conditions, the velocity near the top and bottom walls drops to zero. The centrifugal force is weak in comparison with that at the mid-height. Hence, the flow near the top and bottom is expected to be radially inwards while at the mid-plane, the flow is expected to be radially outwards. This is indeed what is observed in experiments and numerics. Figure 4.2 shows a schematic of the mid-plane symmetric Taylor-vortex mode that is normally observed in TCF.

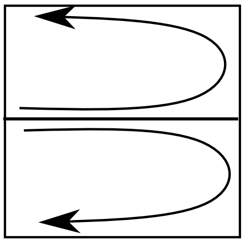

Fig. 4.2 Mid-plane symmetric Taylor-vortex mode.

However, many experimental and numerical investigations have shown the existence of so called “anomalous modes”[Benjamin [4]]. Anomalous modes is a general term. It includes modes which are symmetric about the mid-plane but have the opposite sense of rotation, i.e., the flow is radially outwards near the top and bottom walls. Also, there is a possibility of odd numbered rolls, which break the mid-plane symmetry. In the small aspect ratio limit ($\Gamma = h/d \sim 1$, h being the length of the cylinder and d being the gap width $d = R_2 - R_1$), a single-cell mode has been observed. For the incompressible TCF, a lot of work has been done on finite size effects.

Benjamin [4] first coined the term “anomalous modes” when he studied the finite-size TCF experimentally and theoretically. Mullin [28], Benjamin [4] and Benjamin and Mullin [3] investigated anomalous modes for a range of parameters. Schaeffer [34] proposed a reduced order model to explain the hysteresis phenomena observed in Benjamin’s experiments. He used a homotopy parameter τ which connected the boundary conditions of the periodic domain modeling infinite cylinders ($\tau = 0$) used by theoreticians and the finite domain with stationary top and bottom lids ($\tau = 1$) that mimics experiments. Cliffe [7] and Cliffe and Mullin [8] used finite element method in combination with numerical bifurcation techniques to track the bifurcation diagrams and confirmed the experimental as well as theoretical predictions by previous papers. These calculations also revealed that the term ‘single-cell modes’ is actually a misnomer. For the case of so called ‘single-cell modes’, there actually exist two rolls which are not mid-plane symmetric, one of the rolls is bigger and is located near the top or the bottom wall and there exists another roll of the opposite circulation, but it is weaker in comparison to the bigger roll. This has been confirmed by Cliffe and Mullin [8] in numerics. However, in experiments, because the smaller roll is weaker, it is generally not observed. An experimentalist finds only the bigger roll - hence the term ‘single-cell mode’. Similarly for anomalous modes that are mirror symmetric about the mid-plane, there exist two weaker rolls near the top and bottom walls which are difficult to observe in experiments.

Figure 4.3 shows a schematic of the flow-directions in the anomalous modes. Bolder arrows represent stronger rolls, while weaker rolls can be seen near the top and/or bottom walls.

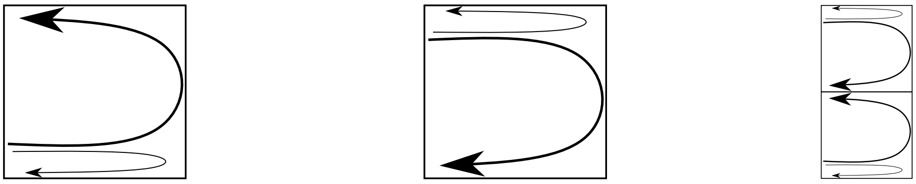

Fig. 4.3 A schematic of anomalous modes.

Later experiments by Mullin [29] observed mutations in the finite Taylor-Couette problem where he observed the cusp catastrophe in the $\Gamma - Re_1$ plane. A few words about catastrophe theory, in particular the cusp catastrophe are in order.

Catastrophe theory is a branch of mathematics which deals with bifurcation theory's applications in the study of dynamical systems. Its origin can be traced back to the French mathematician René Thom in the 1960's. British mathematician Christopher Zeeman popularized catastrophe theory in the 1970's and also made several fundamental contributions. It is well-known from the bifurcation theory that near the critical points of a given nonlinear dynamical system, small changes in the control parameter can cause huge 'qualitative' changes in the behavior of the system. For example, equilibria can appear or disappear or they can change their nature from an attractor to a repeller. These sudden changes in behavior are ubiquitous in scientific problems. Catastrophe theory uncovers the underlying 'geometry' of these sudden events in a larger parameter space.

In his article, Zeeman [42] writes, *"...the underlying forces in nature can be described by smooth surfaces of equilibrium; it is when the equilibrium breaks down that catastrophes occur. The problem for catastrophe theory is therefore to describe the shapes of all possible equilibrium surfaces. Thom has solved this problem in terms of a few archetypal forms, which he calls the elementary catastrophes."*

One of these so called 'elementary catastrophes' is the cusp catastrophe that is of relevance to this chapter. The cusp catastrophe is common in many scientific investigations and occurs when the equilibrium surface folds back on itself when two control parameters are varied. A schematic of the cusp catastrophe is reproduced in Fig. 4.4 from Benjamin [4]'s theoretical paper on anomalous modes in the TCF.

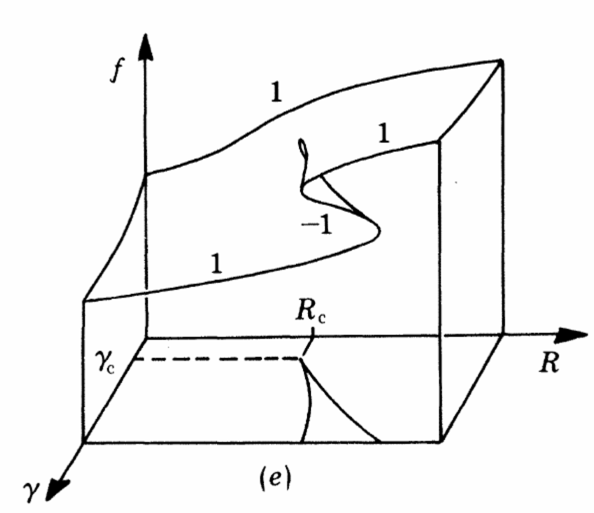

Fig. 4.4 A schematic of the cusp catastrophe taken from Benjamin [4].

In Fig. 4.4, f is the concerned equilibrium quantity while R and γ are two control parameters. As is quintessential of the cusp catastrophe, equilibrium surface of f is seen to fold back on itself. The labels 1 and -1 denote the stability of the equilibrium, 1 being stable and -1 being unstable. When the surface is projected onto the (R,γ) plane, two distinct lines separate the plane. It is also clear that these two lines meet at a 'cusp', giving the catastrophe its name. The cusp point is marked by the critical values of R and γ, denoted in Fig. 4.4 by R_c and γ_c, respectively. Outside the cusp region, there exists only one equilibrium solution while as one crosses the border and enters into the cusp region, three equilibrium solutions suddenly appear. Two of the three solutions are stable while one is unstable. Therefore, inside the cusp region, multiple stable equilibria can exist. Also, one can observe the typical hysteresis associated with such situations.

In the present problem R is equivalent to the inner Reynolds number Re_1 while γ is equivalent to the aspect ratio Γ, which act as control parameters. The equilibrium surface f can be a metric that quantifies the bifurcation from the mid-plane symmetric Taylor-vortex mode to the asymmetric single-cell mode.

Coming back to the work of Mullin [29], he examined the hysteresis in four different cases: $4 \to 6$, $6 \to 8$, $8 \to 10$ and $10 \to 12$, where $4 \to 6$ denotes a hysteresis between 4 and 6-rolled structures and so on. Pfister et al. [32] performed a numerical and experimental study of the finite size Taylor-Couette problem for a range of Γ from 0.3 to 1.4. They also found a satisfactorily good agreement between numerics and experiments.

4.2 Breaking Mid-plane Symmetry: Single-Cell Modes

In this work, we have uncovered single-cell modes at small Γ for the finite-size compressible Taylor-Couette problem. However, realizing these modes numerically is not trivial. The numerical studies mentioned above have considered only steady state solutions via continuation. To realize **anomalous** modes experimentally or numerically, one has to resort to some trickery. Here, for the first time to the best of our knowledge, we have numerically realized single-cell modes for a compressible gas undergoing TCF.

To access the single-cell mode branches, we have used a forcing in the temperature boundary conditions. Initially, to break the mid-plane symmetry of the flow, we change the boundary conditions forcefully by demanding temperature to be $1+\varepsilon$ at the top wall and $1-\varepsilon$ at the bottom wall; ε is chosen to be 10^{-1}. This yields the single-cell mode, depending on the sign of ε. Once the single-cell mode is realized, the forcing is switched off. For some values of Re_1, this solution survives, while for others, it snaps back to the mid-plane symmetric, two-rolled structure.

4.2.1 Numerical Method

Numerical method was as described in Section 2.3 of Chapter 2 with no-slip boundary conditions at the cylinder walls, top and bottom lids. Dirichlet boundary condition for temperature was used at all walls. Because this chapter deals with low aspect ratios, the grid-size was fixed at 21×21. Time stepping was done with a dimensionless time-step of $\Delta t = 10^{-5}$.

4.2.2 Temperature Boundary Condition Trick

The temperature boundary condition trick is described below.

- A small temperature gradient is switched on.
- $T = 1+\varepsilon$ and $T = 1-\varepsilon$ at the top and bottom walls respectively.
- The outer wall has a linear temperature profile.
- The magnitude of ε was chosen to be 10^{-1}.
- This realizes the single-cell mode, depending on the sign of ε.
- After the steady state was achieved, the temperature gradient was switched off by putting $\varepsilon = 0.0$.

- It was observed that the anomalous single cell survives for some Re_1 and for others, the flow goes back to the Taylor vortex flow.

Figure 4.5 shows evidence of single-cell modes (or, asymmetric two-roll mode) in compressible TCF. Two solutions shown in Fig. 4.5a and 4.5b can be obtained from each other via reflection about the mid-plane ($z = 1/2$).

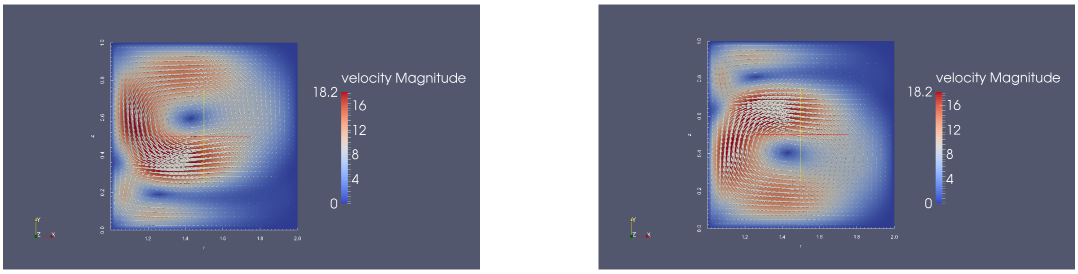

(a) (b)

Fig. 4.5 Single-cell modes, $Re_1 = 180$, $Ma = 1$, $Pr = 1$, $\Gamma = 1$: (a) $\varepsilon = 0.1$, (b) $\varepsilon = -0.1$.

Figures 4.9 and 4.7 show time snapshots of the velocity field showing the transient process of manifesting single-cell modes using the temperature-boundary-condition trick for positive and negative ε, respectively.

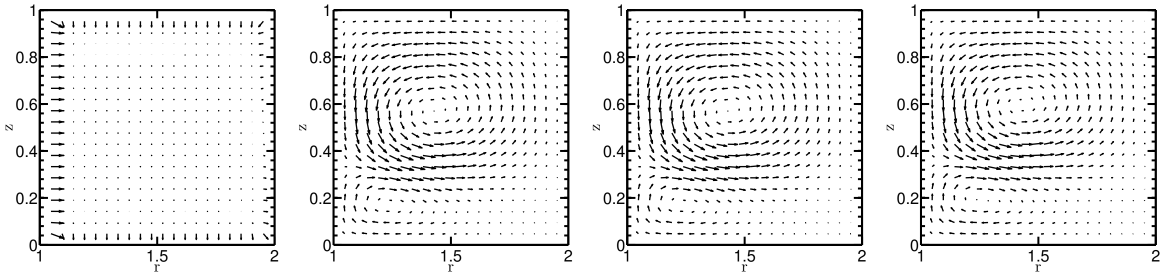

(a) (b) (c) (d)

Fig. 4.6 Temperature Boundary condition trick, $\varepsilon = 0.1$: $Re_1 = 180$, $Ma = 1$, $Pr = 1$, $\Gamma = 1$ (a) $t = 0$: temperature gradient switched on, (b) $t = 8$: single-cell mode settles, (c) $t = 16$: temperature gradient switched off, (d) $t = 24$: single-cell mode survives.

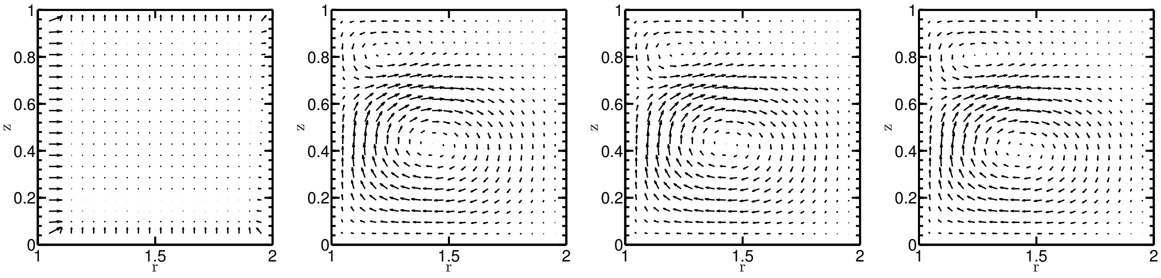

(a) (b) (c) (d)

Fig. 4.7 Temperature Boundary condition trick, $\varepsilon = -0.1$: $Re_1 = 180$ (a) $t = 0$: temperature gradient switched on, (b) $t = 8$: single-cell mode settles, (c) $t = 16$: temperature gradient switched off, (d) $t = 24$: single-cell mode survives.

4.2.3 Other ways of Manifesting Single-cell Modes

Apart from forcefully breaking the mid-plane symmetry by giving an artificial temperature gradient and then switching it off, single-cell modes can be realized in multiple ways as described below.

1. - One of the ways to generate the single-cell mode numerically is to use abrupt changes in the aspect ratio ($\Gamma = h/d$). For example, at $\Gamma = 1$, to generate the mode corresponding to the upper branch of the bifurcation diagram, start with $\Gamma = 1$ impulsively at a given Re_1, say $Re_1 = 200$. After the mid-plane symmetric two-cell structure appears, make an abrupt change in the aspect ratio from 1 to 0.9. This will make the single-cell mode appear at $\Gamma = 0.9$, $Re_1 = 200$. After the steady state for the single-cell mode at $\Gamma = 0.9$ is reached, switch back to $\Gamma = 1.0$ without changing the Reynolds number. It is observed in the numerical experiments that this procedure gives rise to a single-cell structure corresponding to the upper branch.
   - To generate the single-cell structure corresponding to the lower branch, begin with $\Gamma = 1.1$ and $Re_1 = 200$ impulsively. After the mid-plane symmetric two-cell structure appears, make an abrupt change in the aspect ratio from 1.1 to 1. This will make the single-cell mode corresponding to the lower branch of the bifurcation diagram appear at $\Gamma = 1$ and $Re_1 = 200$.
2. Another way of manifesting the single-cell mode is to use the Schaeffer's homotopy parameter τ, see Schaeffer [34]. The boundary conditions can be written as given in Eqn. (4.1). Radial velocity:

$$(1-\tau)\frac{\partial u}{\partial z} \pm \tau u = 0, \tag{4.1a}$$

axial velocity:

$$(1-\tau)\frac{\partial w}{\partial z} \pm \tau w = 0 \tag{4.1b}$$

at $z = 0$ and $z = h$, $R_1 \leq r \leq R_2$.

When $\tau = 0$, we have periodic boundary conditions and when $\tau = 1$ we have the Dirichlet boundary conditions corresponding to top and bottom lids. To generate a single-cell mode at $\Gamma = 1.0$ and $Re_1 = 200$, begin with $\Gamma = 1$ and $Re_1 = 80$ (i.e. well before the bifurcation) and periodic boundary conditions, i.e. $\tau = 0$. Once the Taylor vortex flow (TVF) is established, abruptly change to $Re_1 = 200$ and $\tau = 0$. One can also do an abrupt change in Re_1 and smoothly vary τ from 1 to 0 over time. This results in one of the single-cell modes. In the numerical experiments so far, only the mode corresponding to the lower branch of the bifurcation diagram has been observed.

4.3 Quantification of Bifurcation from a Two-roll to a Single-roll Structure

Single-cell modes (or, more precisely, 'asymmetric' 2-cell modes) are manifested using the temperature boundary condition trick described in Section 4.2.2. Once a single-cell mode is generated, we let the mode become steady before reducing Re_1. Re_1 was reduced by 0.5 after every 8 dimensionless time units.

As can be seen from Fig. 4.5, the single-cell mode breaks the mid-plane symmetry. In order to quantify the bifurcation from the two-roll to the single-roll structure, we use the axial velocity at the mid-plane and mid-height as the bifurcation parameter. If the mode is mid-plane symmetric, i.e., if the symmetric two-roll structure is present, the axial velocity at the mid-plane and mid-height will be zero, owing to symmetry. On the other hand, if it is not mid-pane symmetric the axial velocity at the mid-plane and mid-height will be evidently non-zero. Hence this single parameter alone is enough to quantify the bifurcation we are interested in. This choice is motivated by the one made by Pfister et al. [32].

Some bifurcation diagrams for various values of Γ are shown in Fig. 4.8. The bifurcation diagrams were generated using the temperature boundary condition trick described in Section 4.2.2. All results presented here are for $Ma = 1$ and $Pr = 1$.

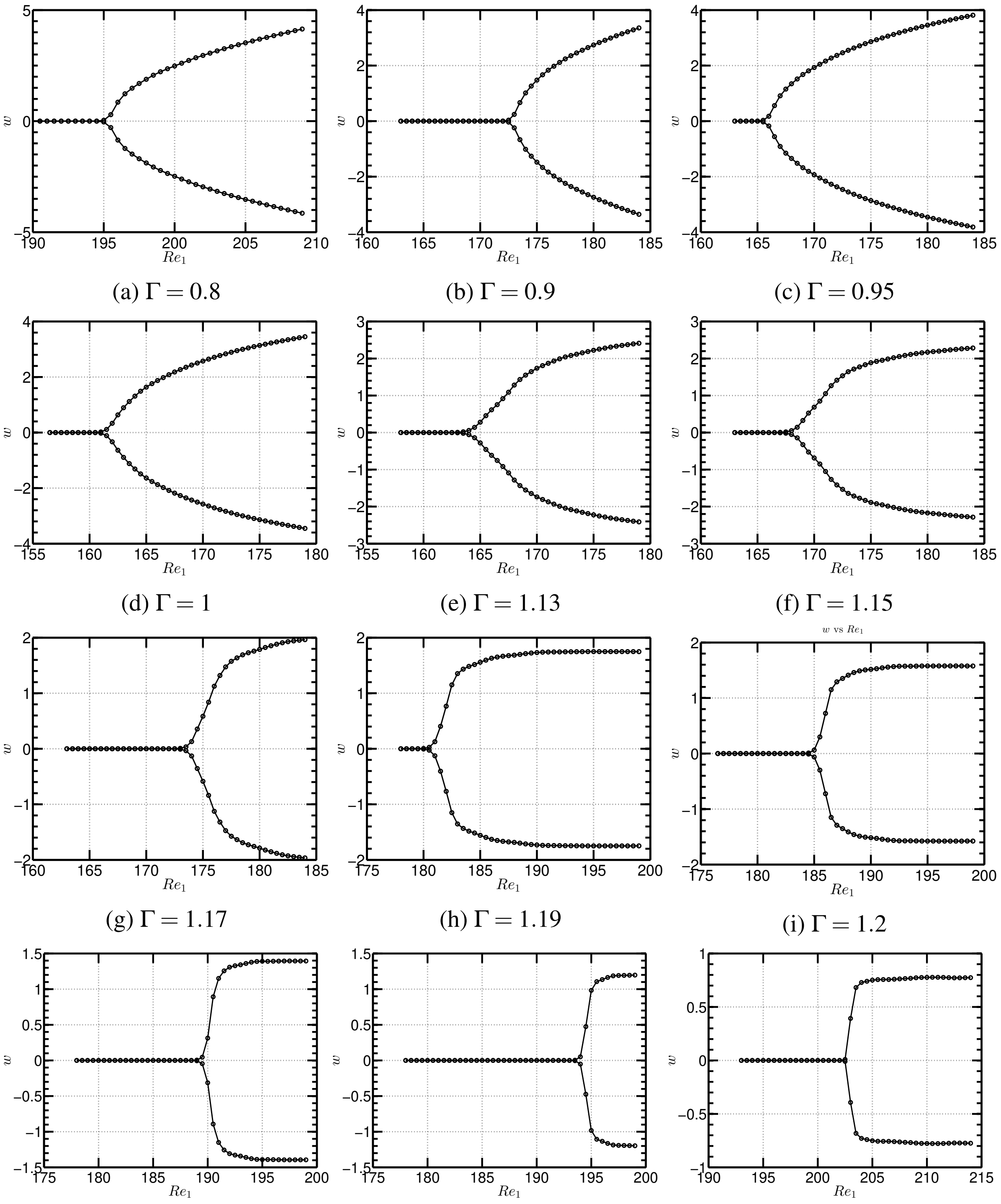

(a) $\Gamma = 0.8$ (b) $\Gamma = 0.9$ (c) $\Gamma = 0.95$

(d) $\Gamma = 1$ (e) $\Gamma = 1.13$ (f) $\Gamma = 1.15$

(g) $\Gamma = 1.17$ (h) $\Gamma = 1.19$ (i) $\Gamma = 1.2$

(j) $\Gamma = 1.21$ (k) $\Gamma = 1.22$ (l) $\Gamma = 1.24$

Fig. 4.8 Bifurcation diagrams: w at mid-plane, mid-height versus Re_1 for different Γ; $Ma = 1$, $Pr = 1$.

In order to visualize the solutions, we plot three sample figures from the upper branch for $\Gamma = 1$ at $Re_1 = 158$, $Re_1 = 170$ and $Re_1 = 175$.

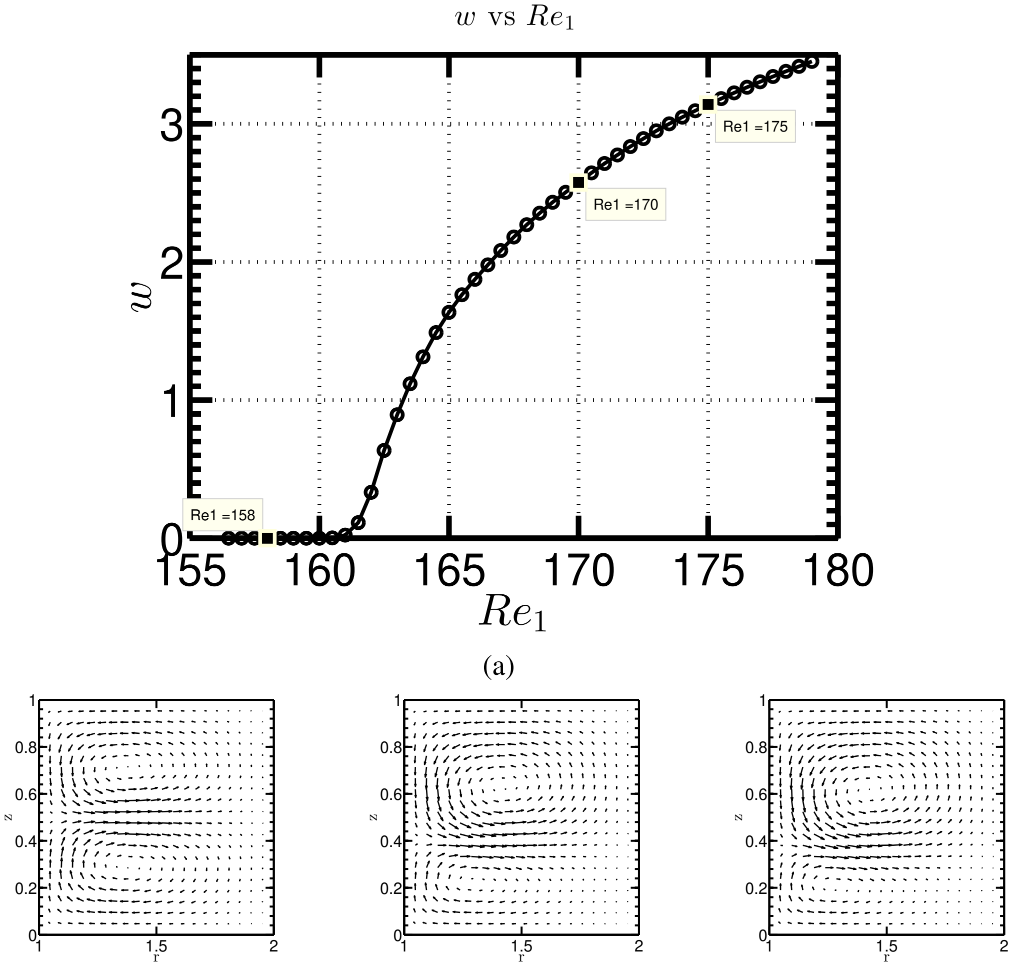

(a)

(b) (c) (d)

Fig. 4.9 Transition from symmetric 2-roll (Panel (b)) to 1-roll (asymmetric 2-roll) solutions (Panel (c) and (d)): (a) Upper branch of the bifurcation diagram of Fig. 4.8d. Velocity plots at points marked in Fig. 4.9a: (b) $Re_1 = 158$, (c) $Re_1 = 170$, (d) $Re_1 = 175$ at $\varepsilon = 0.1$, $Ma = 1$, $Pr = 1$, $\Gamma = 1$.

From Fig. 4.9, we see that the single-roll for a higher Re_1 is bigger. On the other hand, at $Re_1 = 158$, the single-cell mode does not survive and we get a mid-plane symmetric Taylor-vortex mode.

4.3.1 Comparison Between Single-cell Modes Obtained from Different Procedures at $\Gamma = 1$

The bifurcation diagram can again be generated by reducing Re_1 once a single-cell mode has been achieved. The bifurcation diagram generated by method 1 described in Section 4.2.3 superimposed on top of the one generated by the temperature gradient trick is shown in Fig. 4.10. A good match can be seen as shown in Fig. 4.10.

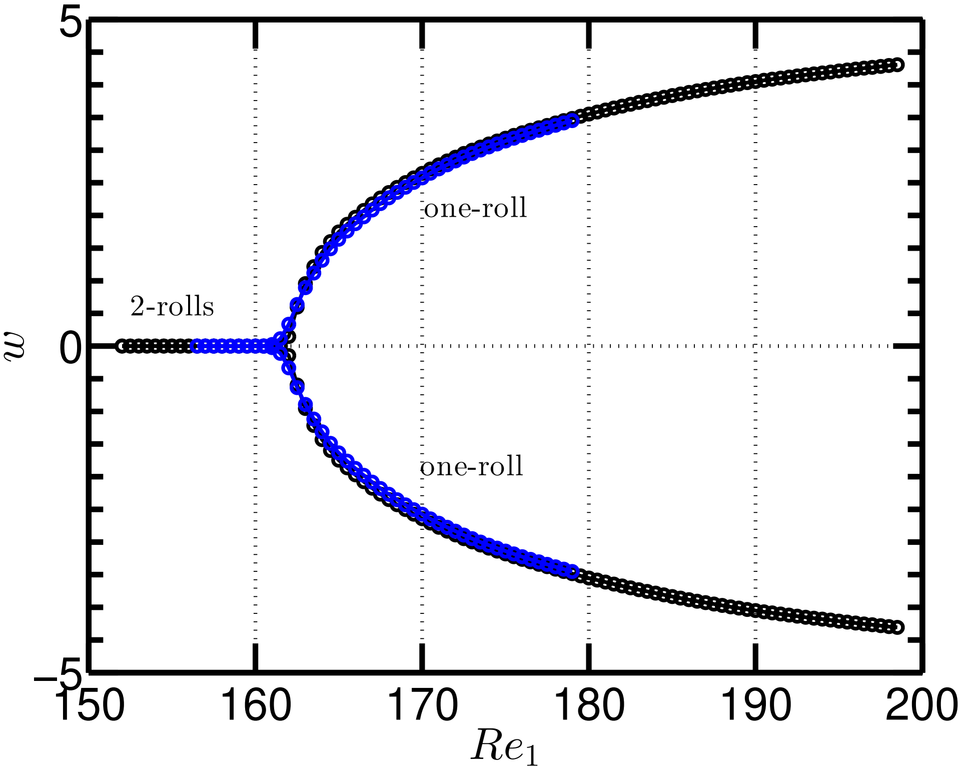

Fig. 4.10 Comparison between bifurcation diagrams generated by different methods with $\Gamma = 1$, $Ma = 1$, $Pr = 1$: (i) blue circles- using the temperature gradient trick and (ii) black circles- abrupt change in Γ.

4.3.2 Uncovering the Bifurcation Scenario in the (Re_1, Γ) Plane

As can be observed in the above Fig. 4.8a - Fig. 4.8c, the critical Re_1 first decreases with increasing aspect ratio (Γ). After $\Gamma = 1$, the branch connecting single-cell mode branches to the symmetric Taylor-roll branch consists of transient points. The flow represented by these points is in fact not steady. To exemplify, let us take a look at Fig. 4.8e. If one stops reducing the Re_1 in the transient code at $Re_1 = 167$, the transient flow will settle down to the symmetric Taylor-vortex mode. In the language of bifurcation theory, the bifurcation becomes 'subcritical'.

This method is not able to find the critical Re_1 for the subcritical bifurcation, as one cannot manifest an unstable branch in a time marching code. Therefore, for a subcritical bifurcation, one has to guess the critical point. However, the trend is evident that after $\Gamma = 1$, the critical Re_1 increases with increasing Γ. Fig. 4.11 shows the qualitative behavior in the (Re_1, Γ) plane.

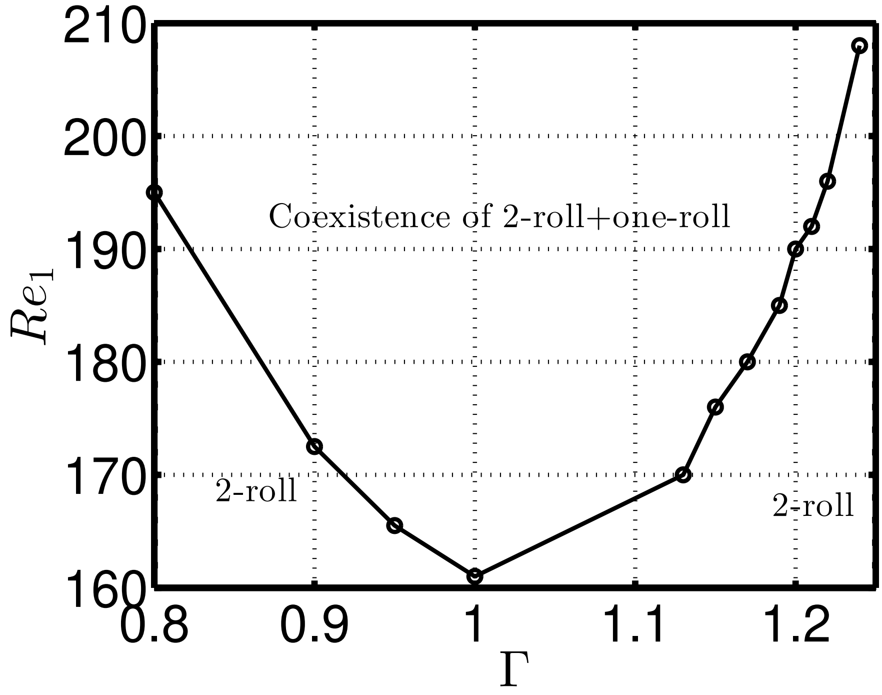

Fig. 4.11 Qualitative phase diagram in the (Re_1, Γ) plane.

4.3.3 Discussion on Single-cell Modes

“There is one feature I notice that is generally missing in cargo cult science. . . . It’s a kind of scientific integrity, a principle of scientific thought that corresponds to a kind of utter honesty — a kind of leaning over backwards. For example, if you’re doing an experiment, you should report everything that you think might make it invalid — not only what you think is right about it; other causes that could possibly explain your results; and things you thought of that you’ve eliminated by some other experiment, and how they worked — to make sure the other fellow can tell they have been eliminated.” - Richard Feynman.

There are several points that need to be addressed. With current results, we can only make a qualitative discussion, speculations and/or educated conjectures. As suggested by studies of Benjamin and Mullin [3] and Pfister et al. [32], the qualitative nature of the bifurcation diagram should change from supercritical to subcritical. From Fig. 4.8, it looks like at lower values of Γ ($\Gamma \leq 1$), the bifurcation is supercritical and after that, the bifurcation starts becoming subcritical. However, this does not seem to be true about current results. The reasons for our doubts are as follows:

1. If one does not use any trick and simply continues increasing Re_1 at a given Γ, it has been observed that one remains on the central TVF branch even when at values of Re_1 where single-cell modes survive. For example, at $\Gamma = 1$, let us say that one begins at $Re_1 = 158$, waits for the TVF to set in and then increment Re_1 to 158.5, waits again for the solution to stabilize and keeps moving on the Re_1 axis. As would appear from the 4.8d, as one goes to $Re_1 > 160$, the solution would have gone to one of the upper- or lower-branch single-cell modes. However, in our simulations, we observed the the solution stays on the main symmetric Taylor-vortex branch.

2. If it were a supercritical pitchfork bifurcation, at $\Gamma = 1$ and $Re_1 > 162$, the Taylor-vortex branch should have become linearly unstable. Hence, even for small perturbations in terms of magnitude of ε should have 'pushed' the mid-plane symmetric solution to one of the single-cell solutions depending on the sign of ε. However, we observed that in order to realize a single-cell mode the magnitude of ε has to be $> 10^{-6}$. We performed numerical experiments for various values of $|\varepsilon|$, namely, $|\varepsilon| = 10^{-1}, 10^{-2}, 10^{-3}, 10^{-4}, 10^{-5}, 10^{-6}$ and 10^{-8} for $\Gamma = 1$. It was observed that for $|\varepsilon| = 10^{-8}$, the solution stayed on the main mid-plane symmetric branch. Also, for $|\varepsilon| = 10^{-1}, 10^{-2}, 10^{-3}, 10^{-4}, 10^{-5}$ and 10^{-6}, we observed the same steady single-cell mode. This observation suggests that single-cell modes obtained in current results are in fact 'finite-amplitude' solutions and at least for the range of Re_1 considered here, the single-cell mode branches are disconnected from the mid-plane symmetric branch.

For the reasons mentioned above, in this case we do not think that for lower values of Γ the bifurcation is supercritical pitchfork. A pertinent question immediately arises concerning the nature of the bifurcation. We speculate that the bifurcation is actually subcritical with two connected or disconnected branches. Figure 4.12 shows a schematic of subcritical bifurcations, with connected and disconnected branches, respectively.

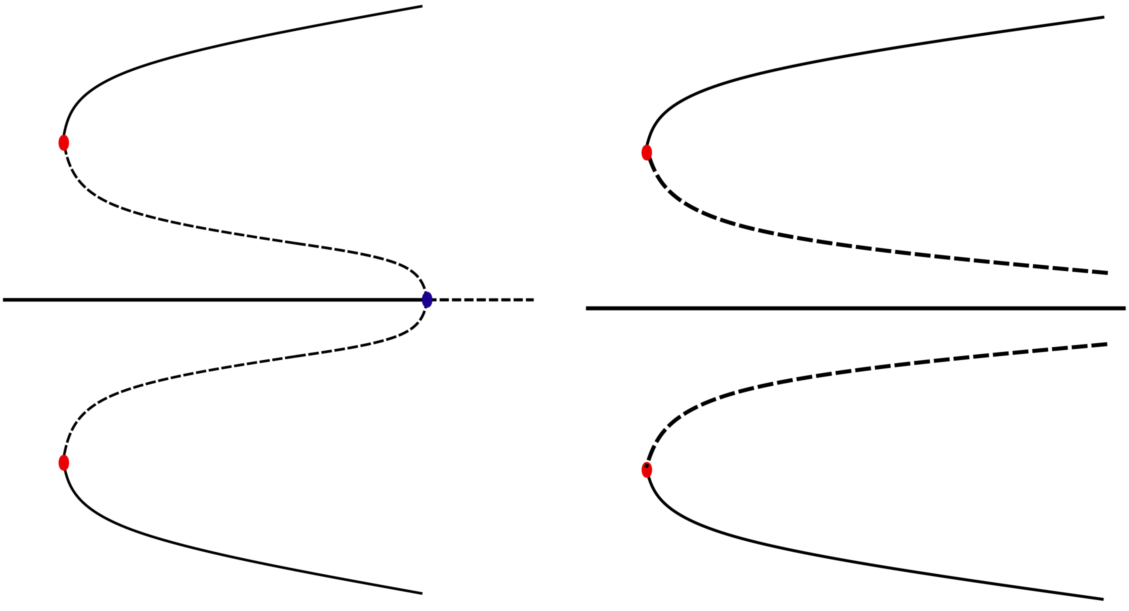

(a) (b)

Fig. 4.12 (a) Subcritical bifurcation and (b) subcritical bifurcation from infinity.

In Fig. 4.12, solid lines represent stable branches while dashed lines represent unstable branches. As shown in Fig. 4.12a, the red nodes correspond to saddle-node bifurcations where stable and unstable branches meet. The blue circle in Fig. 4.12a represents the critical point where two unstable branches bifurcate from a stable branch in a subcritical pitchfork bifurcation. If the blue circle is pushed to infinity, we get a case shown in Fig. 4.12b. In literature, this is referred to as ‘bifurcation from infinity’. At higher values of Γ, for example, $\Gamma = 1.24$, our conjecture is that the single-cell mode branches have completely disconnected from the main Taylor-vortex branch. At lower Γ, however, the scenario can be as shown in 4.12a or 4.12b, with the red nodes arbitrarily close to the main mid-plane symmetric mode branch. As we increase Γ the red nodes might go away from the main branch resulting in completely disconnected single-cell mode branches.

To definitively answer what is happening in our current results, a good continuation routine is needed. With a continuation code, one can track stable as well as unstable branches and that would make the bifurcation scenario clearer.

Another check would be to continue our results which are at $Ma = 1$ to $Ma \sim 0$ to check their connection to single-cell modes in the incompressible TCF. The qualitative phase diagram shown in Fig. 4.11 is a locus of limit-points. In the incompressible case, there are supercritical, subcritical zones along with the locus of limit points, for example see Cliffe [7] and Pfister et al. [32]. We guess that these branches in the (Re_1, Γ) plane can be recovered by continuing current results to $Ma \sim 0$.

4.4 Changing Γ at a Given Re_1

When we keep Re_1 constant and vary Γ, we observe catastrophic transitions regarding number of rolls. To read more about the catastrophe theory, see Strogatz [37] and Golubitsky et al. [13]. The catastrophic jumps are evident if one plots the average kinetic energy based on the radial velocity vs. time. We define average kinetic energies as discussed in Harada [17] and Section 3.6.1. The following procedure was used:

- At every value of Γ, the flow was allowed to settle before going to a new aspect ratio.
- The aspect ratio was changed by 0.1 after every 3×10^5 time steps, i.e., 6 dimensionless time units.
- The aspect ratio was increased from 3.1 to 6.1 from $t = 0$ to $t = 200$ and was decreased back to 3.1 from $t = 200$ to $t = 400$.

We now keep the Re_1 fixed and vary Γ from $\Gamma = 3.1$ to $\Gamma = 6.1$ and then come back to $\Gamma = 3.1$. We do this numerical experiment for four different values of Re_1.

4.4.1 Changing Γ at $Re_1 = 100$

The velocity field is plotted in Fig. 4.13 for the increasing Γ phase and Fig. 4.14 for the decreasing Γ phase:

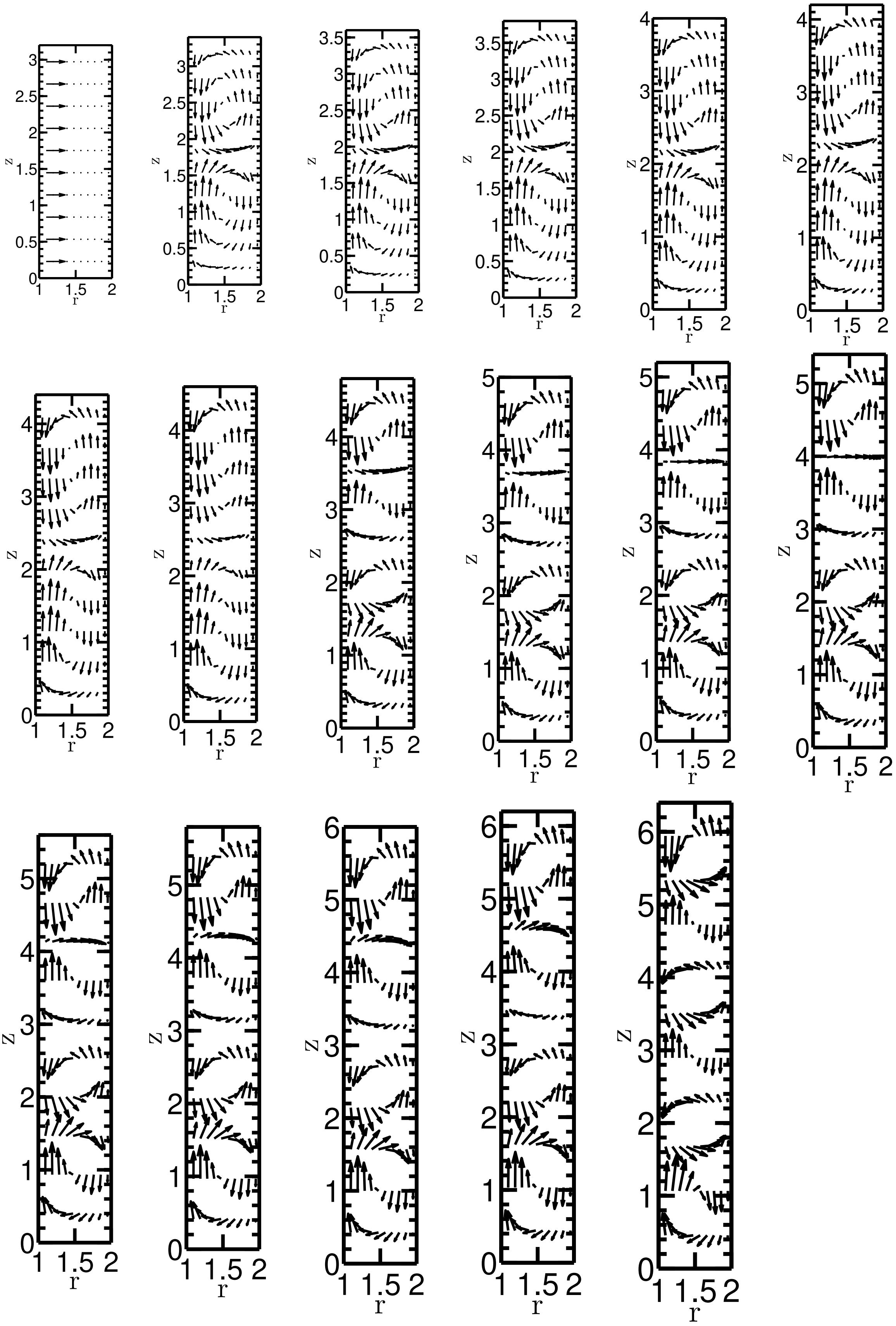

Fig. 4.13 Velocity vector plots in (r,z) plane at $Re_1 = 100$, $Re_2 = 0$, $Ma = 1$, $Pr = 1$, increasing Γ from 3.1 to 6.1.

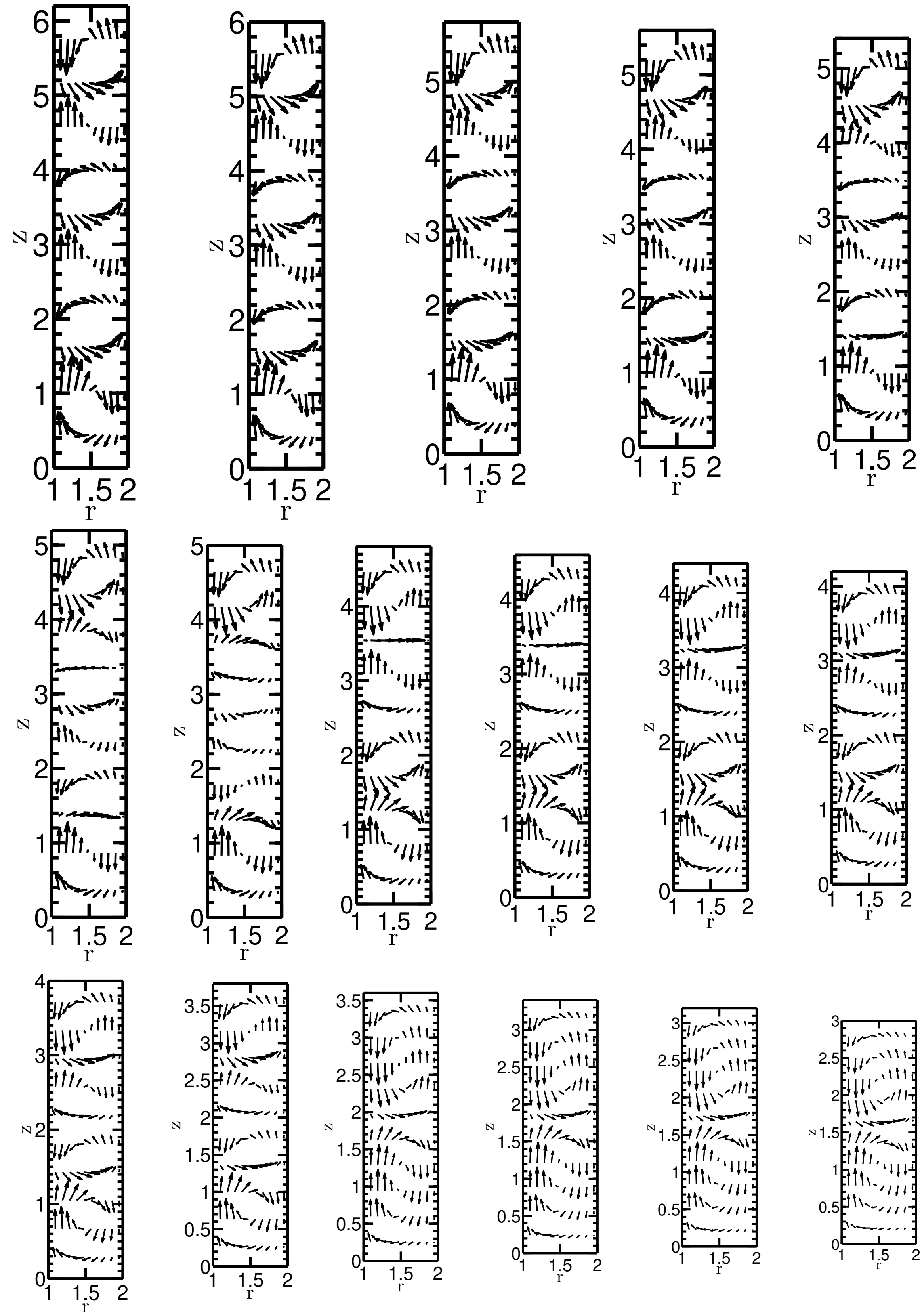

Fig. 4.14 Velocity vector plots in (r,z) plane at $Re_1 = 100$, $Re_2 = 0$, $Ma = 1$, $Pr = 1$, decreasing Γ from 6.1 to 3.1.

From Fig. 4.13, it is clear that the **two-cell** flow jumps to the **four-cell** configuration at around $\Gamma = 4.5$. As the aspect ratio is increased (Fig. 4.13), the **four-cell** flow jumps to the **six-cell** flow at around $\Gamma = 6.1$. While reducing the aspect ratio(Fig. 4.14), the **six-cell** configuration collapses to a **four-cell** configuration around $\Gamma = 5$ which then later jumps back to the original **two-cell** flow around $\Gamma = 3.6$.

Hence, the hysteresis between states with 2, 4 and 6 rolls is seen in when Γ is varied. Hence for a given Re_1, a schematic of the bifurcation diagram with varying Γ could be of the form shown in Fig. 4.15.

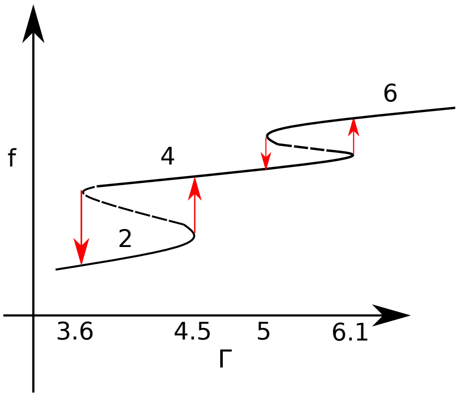

Fig. 4.15 A schematic of hysteresis seen in the bifurcation diagram at $Re_1 = 100$.

In Fig. 4.15, f can be a metric to quantify the hysteresis, for example, if f is the number of rolls, the curves will become straight horizontal lines and instead of a snaking structure, we will observe step changes. Solid lines represent stable solutions while dashed lines represent unstable solutions in Fig. 4.15.

In Fig. 4.16, KE_u versus t and KE_w versus t show distinct jumps when the flow configuration changes. This figure is in qualitative agreement with the postulated schematic in Fig. 4.15.

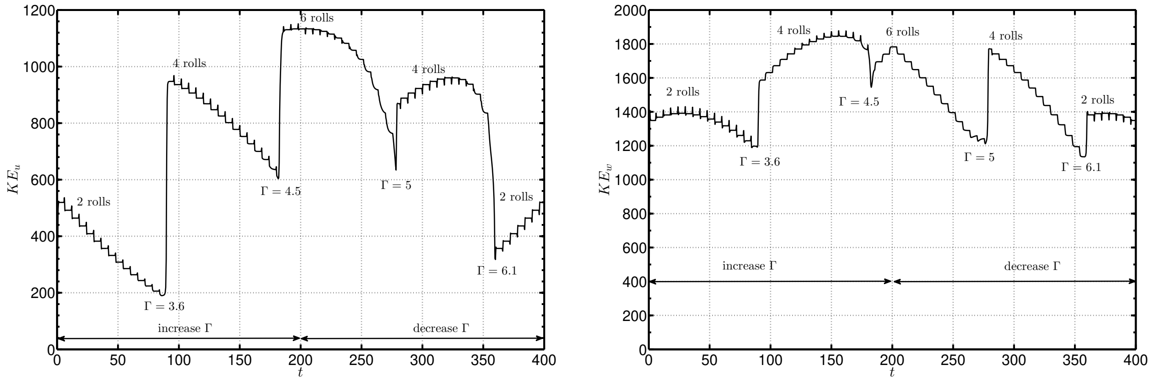

(a) (b)

Fig. 4.16 $Re_1 = 100$, $Re_2 = 0$, $Ma = 1$, $Pr = 1$, vary Γ, time series for (a) KE_u and (b) KE_w.

4.4.2 Changing Γ at $Re_1 = 125$

The velocity field looks according to figures (4.17) while increasing Γ and (4.18) while decreasing Γ:

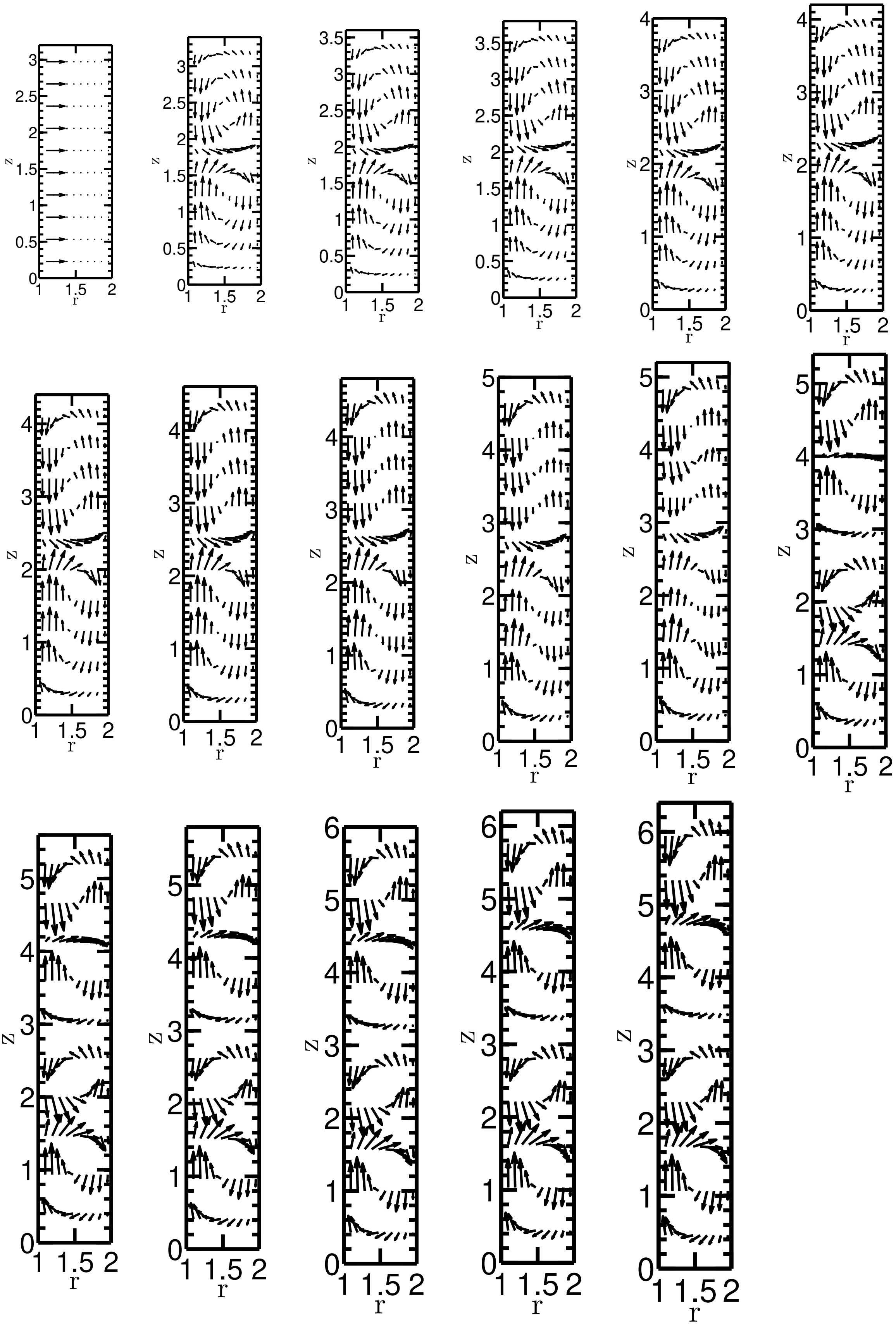

Fig. 4.17 Velocity vector plots in (r, z) plane at $Re_1 = 125$, $Re_2 = 0$, $Ma = 1$, $Pr = 1$, increasing Γ from 3.1 to 6.1.

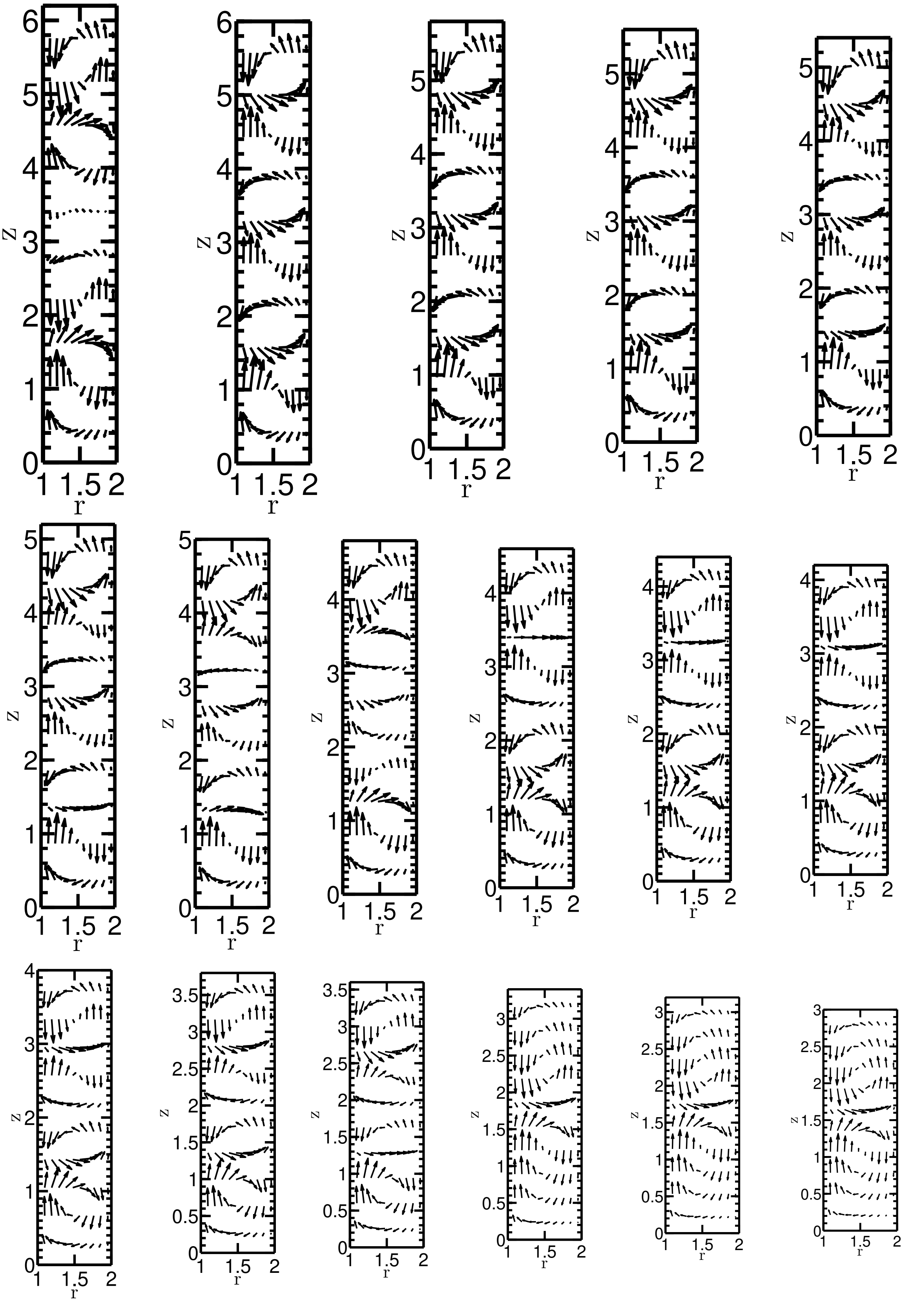

Fig. 4.18 Velocity vector plots in (r,z) plane at $Re_1 = 125$, $Re_2 = 0$, $Ma = 1$, $Pr = 1$, decreasing Γ from 6.1 to 3.1.

At $Re_1 = 125$, the qualitative behavior remains similar to that at $Re_1 = 100$. As we increase Γ from 3.1 to 6.1 (Fig. 4.17), we see a $2 \rightarrow 4 \rightarrow 6$-roll transition, while coming back from 6.1 to 3 (Fig. 4.18), we observe the flow collapsing from $6 \rightarrow 4 \rightarrow 2$ rolled structure.

In Fig. 4.19, KE_u versus t and KE_w versus t show distinct jumps when the flow configuration changes.

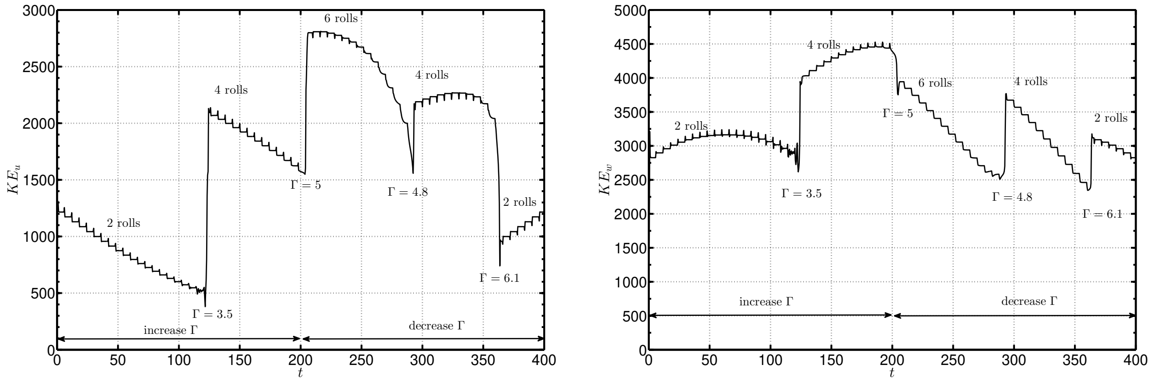

(a) (b)

Fig. 4.19 $Re_1 = 125$, $Re_2 = 0$, $Ma = 1$, $Pr = 1$, vary Γ, time series for (a) KE_u and (b) KE_w.

A schematic of the hysteresis along with the transition values of Γ is shown in Fig. 4.20. Notice in Fig. 4.20 that the transition points have moved from their previous values at $Re_1 = 100$ (Fig. 4.15).

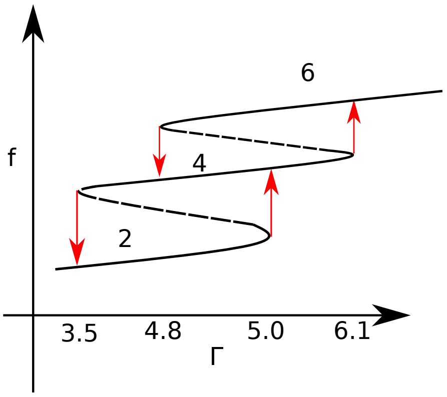

Fig. 4.20 A schematic of hysteresis seen in the bifurcation diagram at $Re_1 = 125$.

4.4.3 Changing Γ at $Re_1 = 150$

The velocity vector plots are as shown in figures (4.21) while increasing Γ and (4.22) while decreasing Γ:

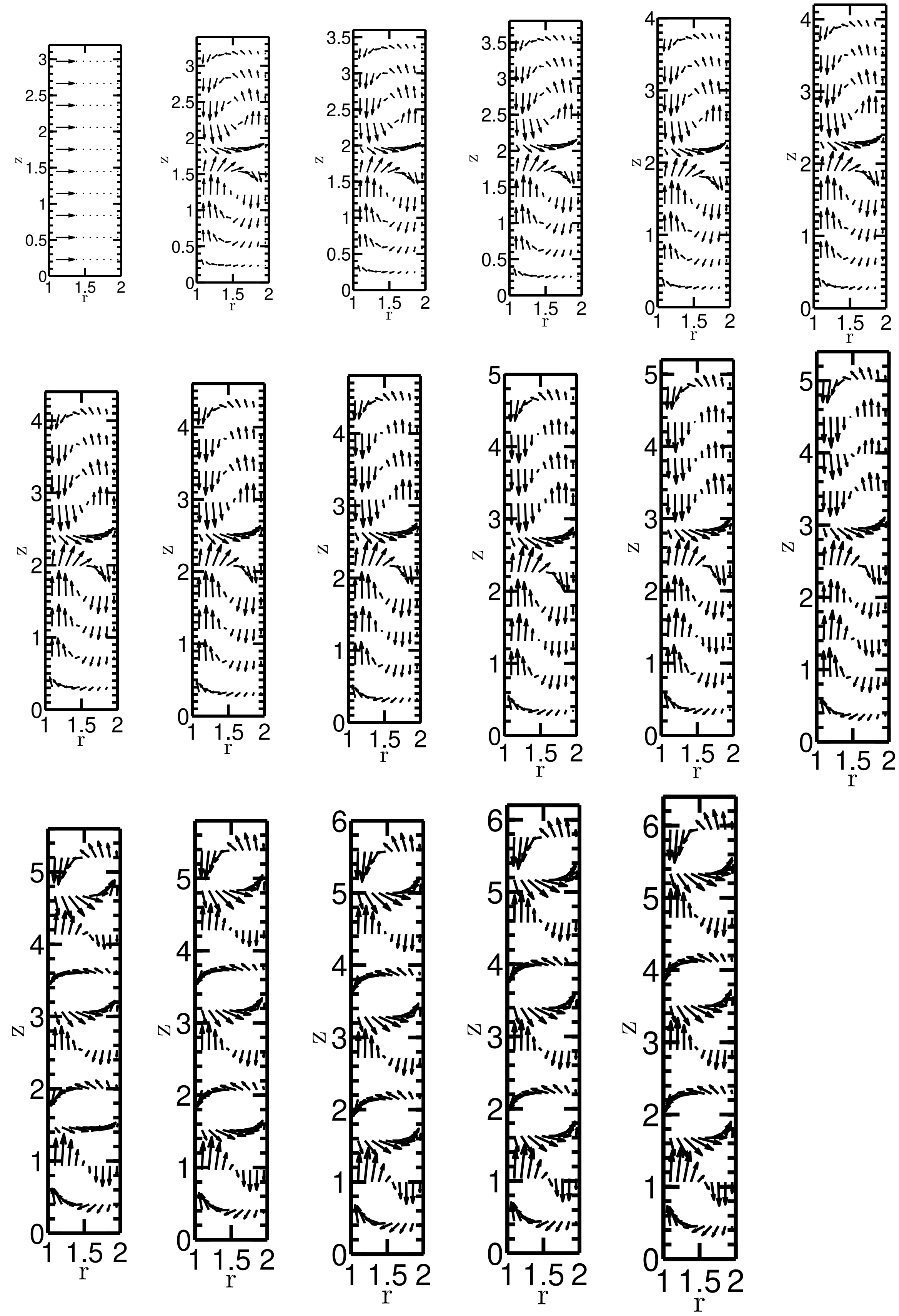

Fig. 4.21 Velocity vector plots in (r,z) plane at $Re_1 = 150$, $Re_2 = 0$, $Ma = 1$, $Pr = 1$, increasing Γ from 3.1 to 6.1.

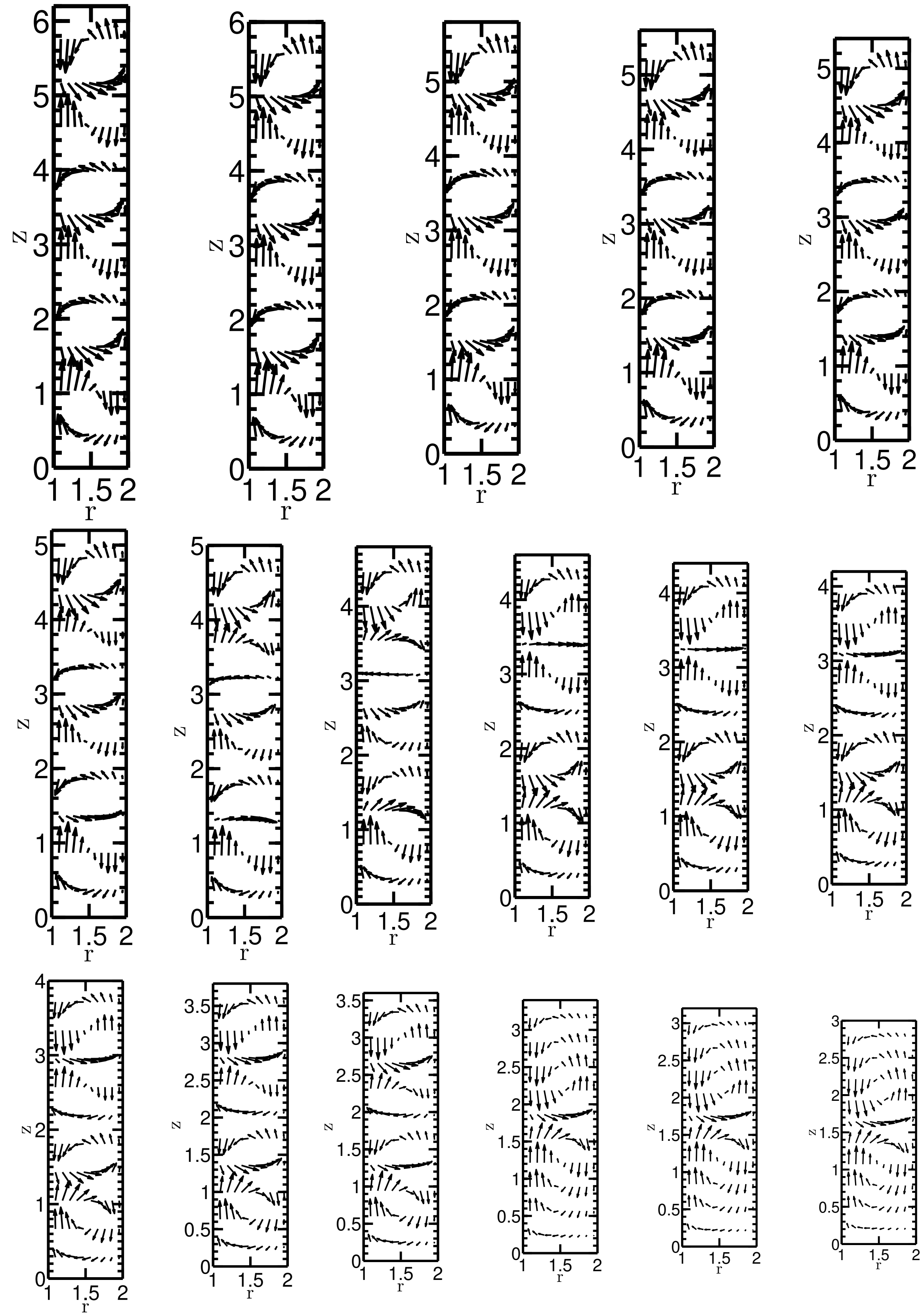

Fig. 4.22 Velocity vector plots in (r, z) plane at $Re_1 = 150$, $Re_2 = 0$, $Ma = 1$, $Pr = 1$, increasing Γ from 6.1 to 3.1.

At $Re_1 = 150$, the qualitative behavior changes from that at $Re_1 = 100$. From Fig. 4.21 and Fig. 4.22, it is clear that the **2-cell** flow jumps to the **6-cell** configuration at around $\Gamma = 5.5$. On the other hand, while reducing the Γ (Fig. 4.22), the **6-cell** first collapses to a **4-cell** configuration at $\Gamma \sim 4.6$ which then later jumps back to the original **2-cell** flow.

In Fig. 4.23, KE_u versus t and KE_w versus t show distinct jumps when the flow configuration changes.

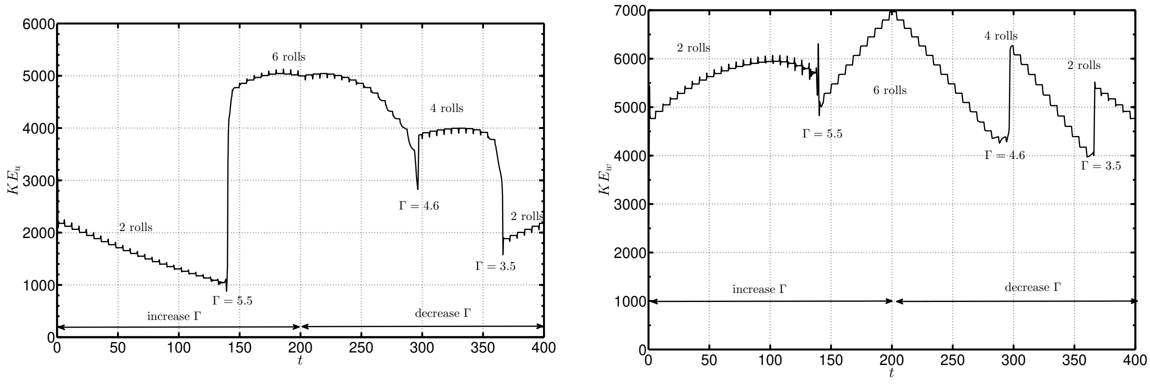

(a) (b)

Fig. 4.23 $Re_1 = 150$, $Re_2 = 0$, $Ma = 1$, $Pr = 1$, vary Γ, time series for (a) KE_u and (b) KE_w.

A corresponding schematic of the hysteresis along with the transition values of Γ is shown in Fig. 4.24. Notice in Fig. 4.24, the $2 \rightarrow 6$-roll transition point is at a higher Γ than the $4 \rightarrow 6$-roll transition point. Hence only $2 \rightarrow 6$ is observed.

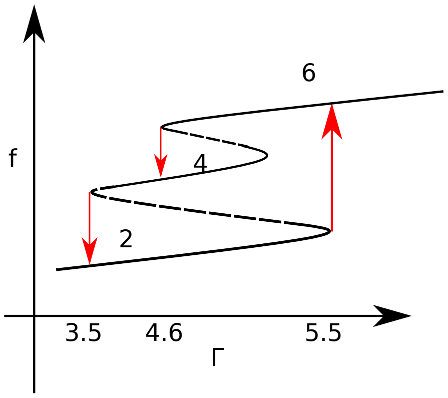

Fig. 4.24 A schematic of hysteresis seen in the bifurcation diagram at $Re_1 = 150$.

4.4.4 Changing Γ at $Re_1 = 200$

The velocity field looks as per Fig. 4.25 while increasing Γ and Fig. 4.26 while decreasing Γ.

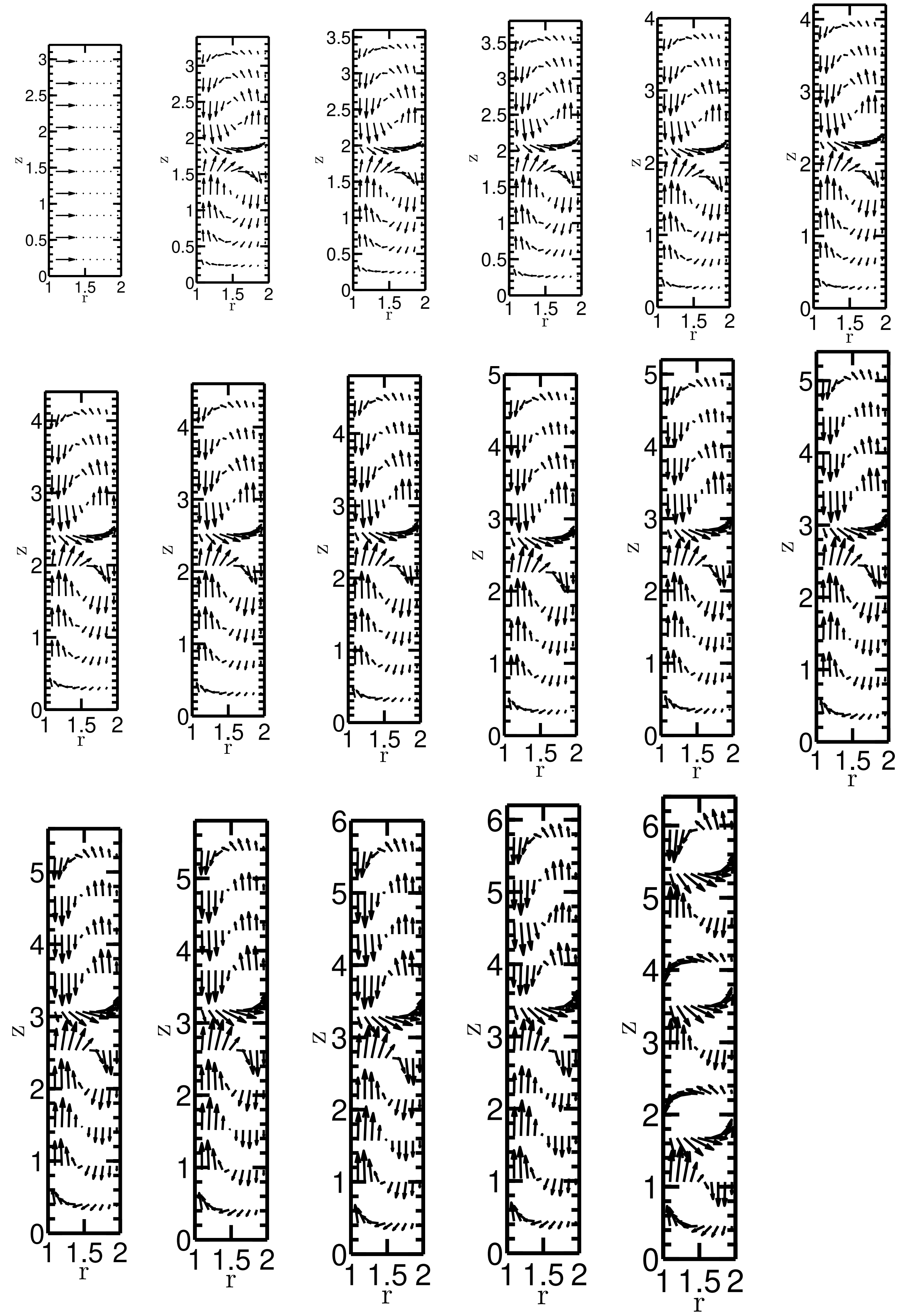

Fig. 4.25 Velocity vector plots in (r,z) plane at $Re_1 = 200$, $Re_2 = 0$, $Ma = 1$, $Pr = 1$, increasing Γ from 3.1 to 6.1.

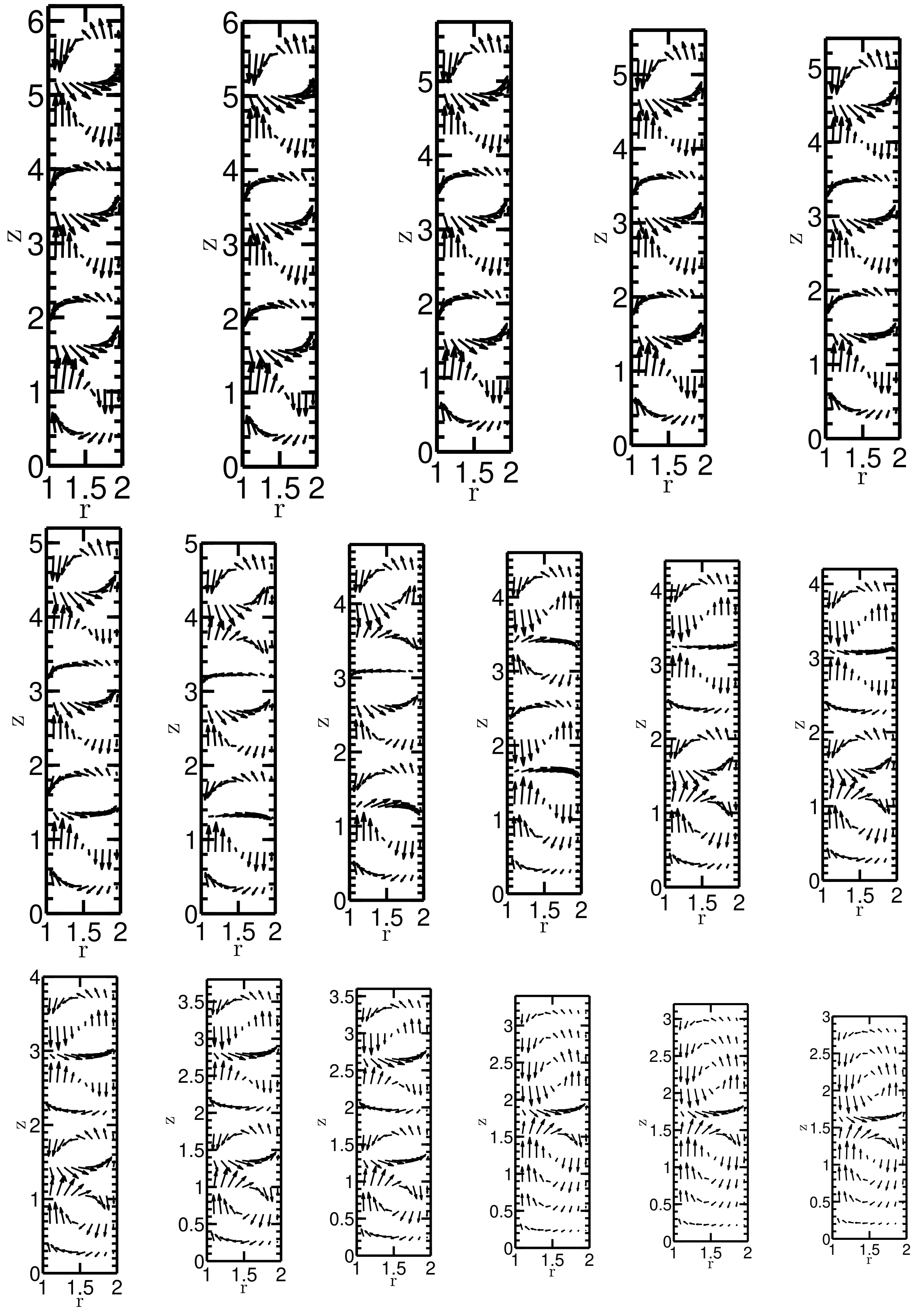

Fig. 4.26 Velocity vector plots in (r,z) plane at $Re_1 = 200$, $Re_2 = 0$, $Ma = 1$, $Pr = 1$, decreasing Γ from 6.1 to 3.1.

At $Re_1 = 200$ the behavior remains qualitatively similar to the one at $Re_1 = 150$. As we increase Γ from 3.1 to 6.1 (Fig. 4.25), we see a $2 \rightarrow 6$-roll transition at $\Gamma \sim 6.1$, while coming back from 6.1 to 3 (Fig. 4.26), we see the flow collapse from $6 \rightarrow 4 \rightarrow 2$ rolled structure.

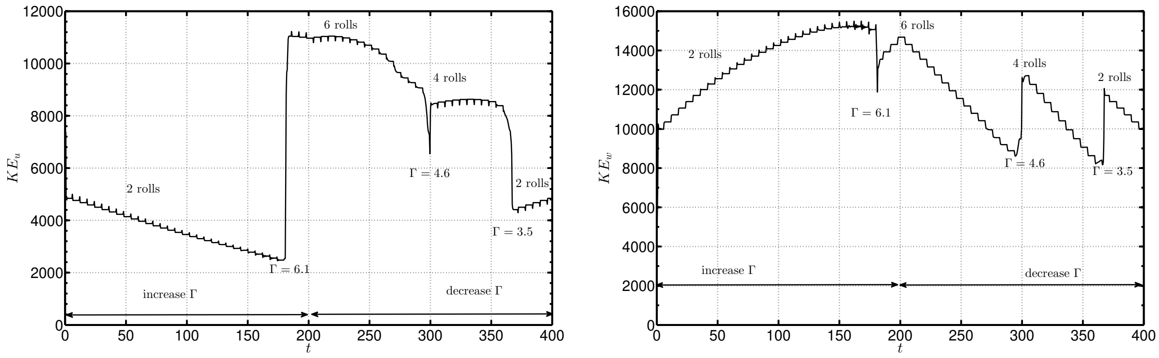

(a) (b)

Fig. 4.27 $Re_1 = 200$, $Re_2 = 0$, $Ma = 1$, $Pr = 1$, vary Γ, time series for (a) KE_u and (b) KE_w.

Steps in the kinetic energy vs. time graphs in Fig. 4.27 imply the change in the aspect ratio. Initially KE_u decreases as the two-rolled structure becomes elongated. The first jump in the average kinetic energy based on the radial velocity implies the transition from two rolls to six rolls. This increase is also intuitive because when the structure changes from two to six rolls, more part of the flow has radial velocity. The second jump marks the transition while coming back from $\Gamma = 6.1$ from six-rolls to four-rolls. Finally, the third jump corresponds to the transition from the four-rolled structure to the two-rolled structure. Again, the decrease in the kinetic energy can also be intuitively explained by the same reasoning.

A schematic of the hysteresis along with the transition values of Γ is shown in Fig. 4.28. f can be a metric quantifying the transitions. Solid lines represent stable solutions while dashed lines represent unstable solutions. Notice in Fig. 4.28, the $2 \rightarrow 6$-roll transition point is at a higher Γ than the $4 \rightarrow 6$-roll transition point. Hence only $2 \rightarrow 6$ is observed while increasing Γ.

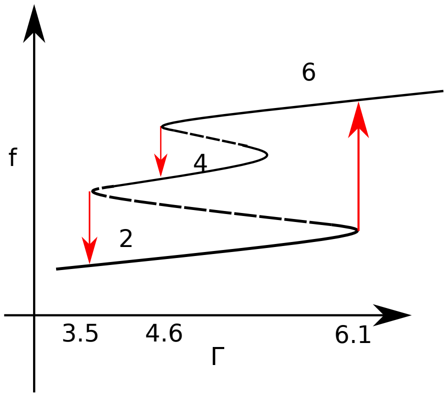

Fig. 4.28 A schematic of hysteresis seen in the bifurcation diagram at $Re_1 = 200$.

4.5 Summary and Conclusion

This chapter began with describing the finite-size counterpart of the compressible TCF. The geometry and dimensionless boundary conditions were as shown in Fig. 4.1. A brief review of work done on anomalous modes in the incompressible finite-size TCF was presented. The cusp catastrophe was introduced in Section 4.1. Some methods of obtaining single-cell modes in low-aspect-ratio ($\Gamma = h/d \sim 1$) cases are described in Section 4.2. Bifurcation diagrams obtained from two different methods are compared in Fig. 4.10 and were found to be in agreement.

To the best of our knowledge, single-cell modes were obtained in the compressible TCF for the first time. The mid-plane, mid-height axial velocity was chosen as the bifurcation parameter to quantify the bifurcation from the mid-plane symmetric Taylor-Vortex flow to asymmetric single-cell modes. The bifurcation diagram of the mid-plane, mid-height axial velocity vs. Re_1 is plotted for different $\Gamma \sim 1$ in Fig. 4.8. Discussion and some conjectures about the bifurcation scenario were presented. A qualitative picture in the (Re_1, Γ) plane is given in Fig. 4.11.

For a constant Re_1, Γ is increased from 3.1 to 6.1 and then decreased from 6.1 to 3.1 for four different Re_1, namely, $Re_1 = 100, 125, 150, 200$. Clear hysteresis is seen in all four cases and is evident from the jumps in the kinetic energy versus time plots. However, the qualitative nature of the hysteresis is seen to be different. For $Re_1 = 100$ and 125, while increasing Γ a $2 \rightarrow 4 \rightarrow 6$-roll transition is seen and while decreasing Γ, $6 \rightarrow 4 \rightarrow 2$-roll jumps are observed. On the other hand, for $Re_1 = 150$ and 200, although the $2 \rightarrow 6$-roll transition is seen while increasing Γ, jumps from $6 \rightarrow 4 \rightarrow 2$ rolls are observed while decreasing Γ. This suggests a complicated nature of the catastrophe in the (Re_1, Γ) plane.

Schematics of the hysteresis for four different values of Re_1 ($Re_1 = 100, 125, 150, 200$) are summarized in Fig. 4.29.

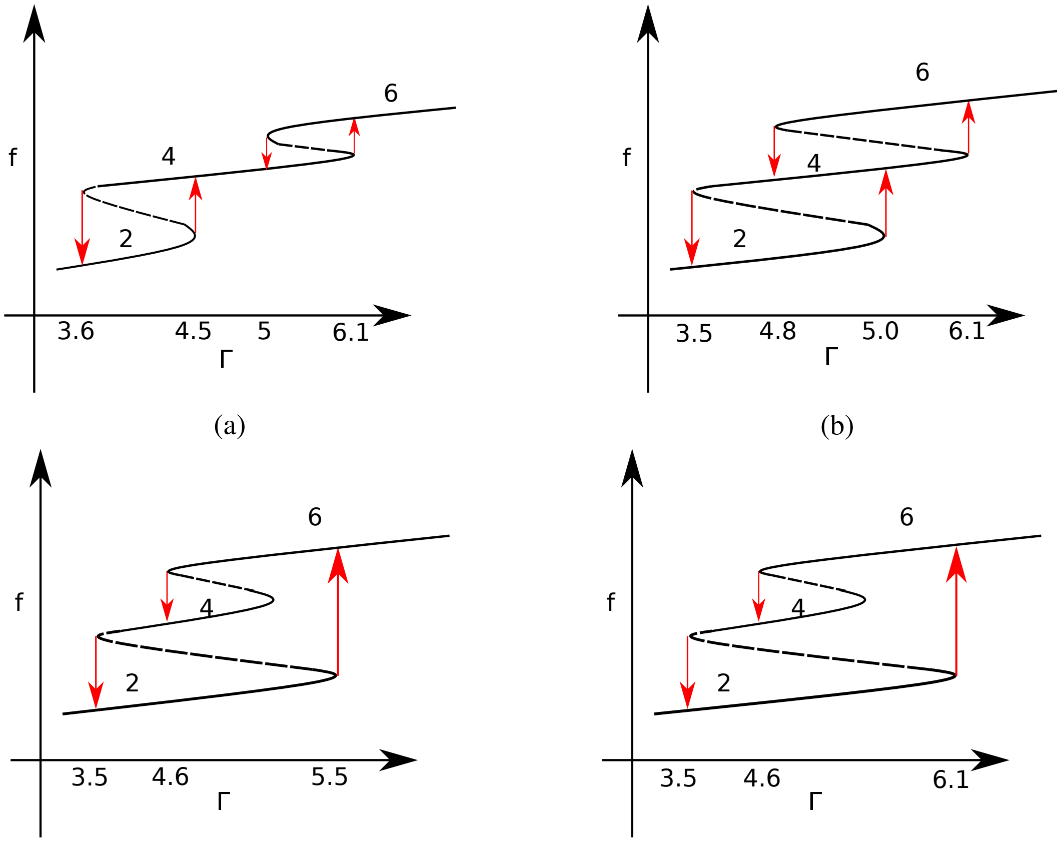
6
f
4
2
3.6
4.5
5
6.1
Γ
6
f
4
2
3.5
4.8
5.0
6.1
Γ
6
f
4
2
3.5
4.6
5.5
Γ
6
f
4
2
3.5
4.6
6.1
Γ

(a) (b)

(c) (d)

Fig. 4.29 Schematics of hysteresis for (a) $Re_1 = 100$, (b) $Re_1 = 125$, (c) $Re_1 = 150$, (d) $Re_1 = 200$.

Chapter 5

Summary and Outlook

“This work contains many things which are new and interesting. Unfortunately, everything that is new is not interesting, and everything which is interesting, is not new.” - Lev Landau.

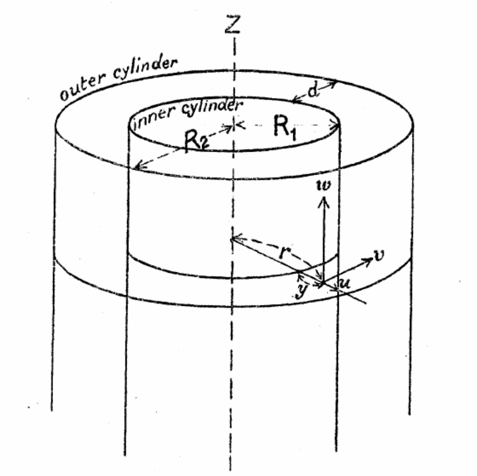

Fig. 5.1 Geometry of the Taylor-Couette setup, Taylor [39].

Taylor-Couette flow is the annular flow between two concentric, differentially rotating cylinders. Figure 5.1 shows the geometry of the setup and is taken from Taylor [39]. Chapter1 began with a brief history of the Taylor-Couette problem. Rayleigh’s inviscid instability criterion was derived by giving an energy argument. A short review of work done so far in the compressible Taylor-Couette problem was presented at the end of Chapter 1.

In chapter 2, a finite difference code is developed to solve axisymmetric Navier-Stokes equations in cylindrical geometry. In order to validate the code, results are obtained for particular cases of thermally and mechanically driven flows and compared with Harada [17]. Axial and radial profiles of different velocities were found to be in agreement with Harada [17]. Temperature and azimuthal velocity contours were also found to be in good agreement, except for one case (Case - 3, Table 2.2). This inconsistency is probably because of a printing mistake. Physical interpretation was given in order to explain numerical results for both thermally and mechanically driven flows.

5.1 Pattern Formation in Compressible TCF with Periodic Boundary Conditions

Chapter 3 began with writing dimensionless equations and boundary conditions for the compressible Taylor-Couette flow. Characteristic quantities for non-dimentionalization are so chosen that numerical results can be compared with experiments [Welsh et al. [41]]. Another verification of the code was presented by matching the analytically known base state of compressible TCF with the one obtained from long-time marching of compressible Navier-Stokes equations.

The effect of variable viscosity on the onset of Taylor vortex flow was then investigated. The variation of viscosity as a function of temperature was described by the well-known Sutherland's law of shear viscosity. To quantify the bifurcation from the circular Couette flow (CCF) to the Taylor vortex flow (TVF), average circulation of the upper roll was plotted against the Reynolds number as shown in Fig. 5.2. The procedure to calculate the average circulation was also described. It was observed that the critical Re_1 increases in the case of variable viscosity, which implies variable viscosity stabilizes the compressible TCF.

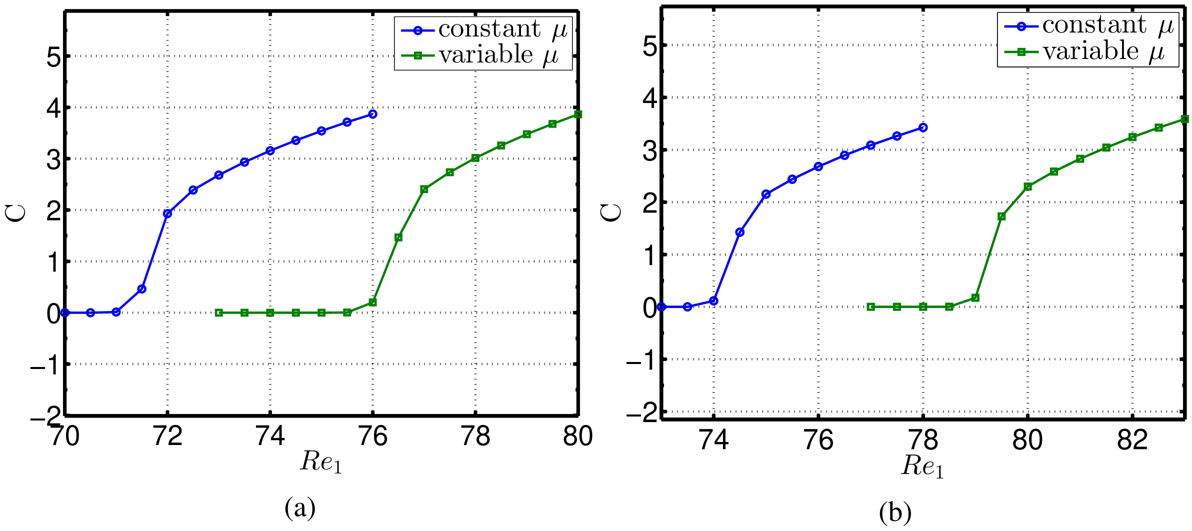

(a)

(b)

Fig. 5.2 Average circulation versus Re_1 with $Ma = 1$ and $Pr = 1$ for constant and variable viscosity for different heights $(= 2\pi/k)$ of the computational domain: (a) $k = 3.1729$ and (b) $k = 4$.

Typical fields such as the velocity vector and contours of density, temperature, specific angular momentum and azimuthal velocity in the (r,z) plane were plotted as Re_1 was varied. As expected, before bifurcation, there were no axial gradients in the contours of the above quantities, whereas after the flow bifurcated to the TVF, axial gradients started to develop. The same exercise was repeated keeping Re_1 fixed and changing the height of the computational domain.

At higher values of Re_1, a secondary bifurcation was found. The TVF was seen to bifurcate to a traveling wave in the negative z-direction, when axisymmetry was imposed, see Fig. 5.3.

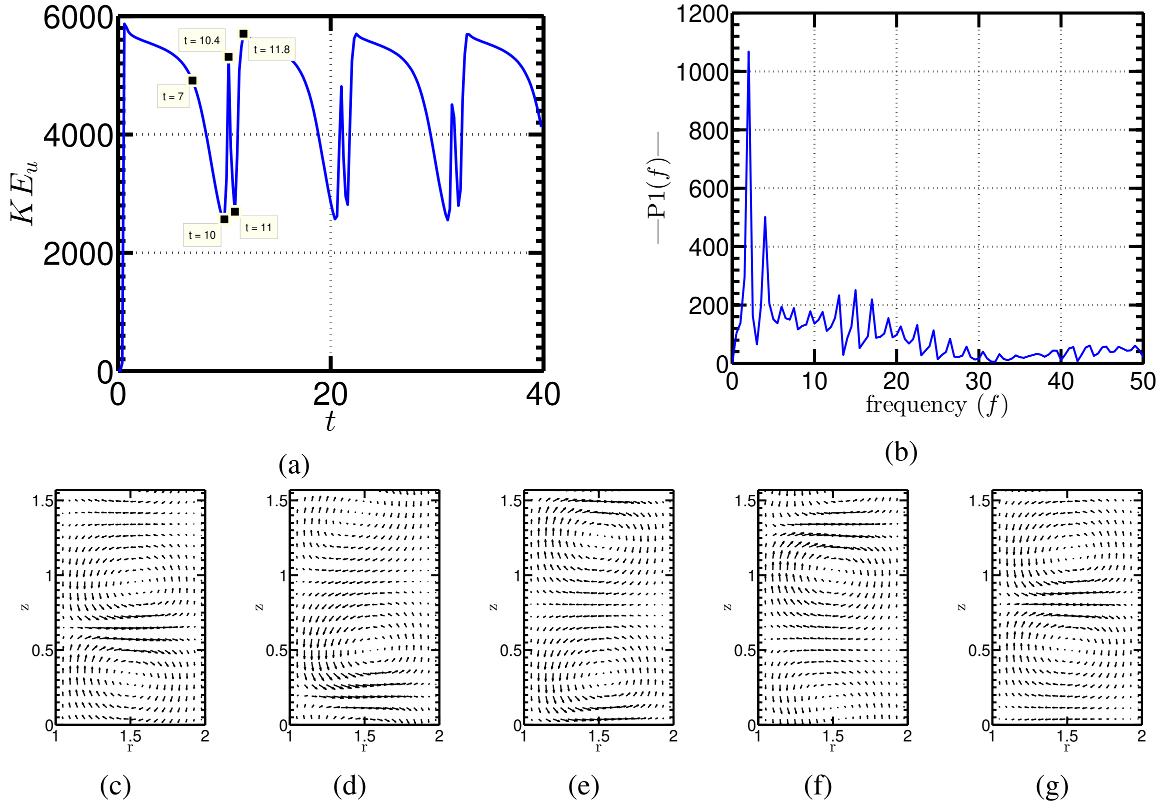

(a)

(b)

(c) (d) (e) (f) (g)

Fig. 5.3 Traveling wave at $Re_1 = 190$, $Re_2 = 0$, $Ma = 1$, $Pr = 1$, $k = 2\pi/h = 4$: (a) Time series for kinetic energy KE_u, (b) single-sided amplitude spectrum for KE_u. Figures 5.3c-5.3g show snapshots of the velocity vector plots at points marked in Fig. 5.3a. Velocity vector plots at (c) $t = 7$, (d) $t = 10$, (e) $t = 10.4$, (f) $t = 11$, (g) $t = 11.8$.

In order to extract dominant dimensionless frequencies, fast Fourier transform (FFT) was performed. Mean kinetic energies were subtracted and one-sided amplitudes were plotted in the frequency domain. Dominant frequency of the traveling wave was extracted via the fast Fourier transform (FFT). This exercise was repeated for a range of Re_1 and dimensionless dominant as well as second-dominant frequencies were plotted against the inner Reynolds number (Re_1). Dimensionless frequencies converted and plotted against Re_1 on the inertial time-scale.

5.2 Finite-size Effects in Compressible TCF

Chapter 4 focused on studying the finite-size effects, in particular the so called 'anomalous modes' [Benjamin [4]] in the compressible TCF. When top and bottom walls are present, the finiteness of cylinders is characterized by the aspect ratio $\Gamma = h/d$ where h is the height of the cylinders and $d = R_2 - R_1$ is the gap width. In a finite sized container, because of no-slip boundary conditions, the velocity near the top and bottom walls drops to zero. The centrifugal force is weak in comparison with that at the mid-height. Hence, the flow near the top and bottom is expected to be radially inwards while at the mid-plane, the flow is expected to be radially outwards. This is indeed what is observed in experiments and numerics. However, many investigations have shown the existence of so called 'anomalous modes' discovered by Benjamin [4]. 'Anomalous modes' include modes which are symmetric about the mid-plane but have the opposite sense of rotation, i.e., near the top and bottom walls, the flow is radially outwards. Also, there is a possibility of odd numbered rolls, which break the mid-plane symmetry. In the small aspect ratio limit ($\Gamma = h/d \sim 1$, h being the length of the cylinder and d being the gap width $d = R_2 - R_1$), single-cell (or, asymmetric two-cell) modes have been observed.

To the best of our knowledge, single-cell modes in finite-size compressible TCF were obtained for the first time. To manifest single-cell modes in short-cylinder case ($\Gamma \sim 1$), a temperature boundary trick was described and employed. In order to visualize obtained single-cell modes, some steady state velocity vector plots are reproduced in Fig. 5.4 for $\Gamma = 1$ at $Re_1 = 158$, $Re_1 = 170$ and $Re_1 = 175$. From Fig. 5.4, it was clear that the single-roll for a higher Re_1 is bigger as compared to the one at a lower value of Re_1. On the other hand, at $Re_1 = 158$, the single-cell mode does not survive and we get a mid-plane symmetric Taylor-vortex mode.

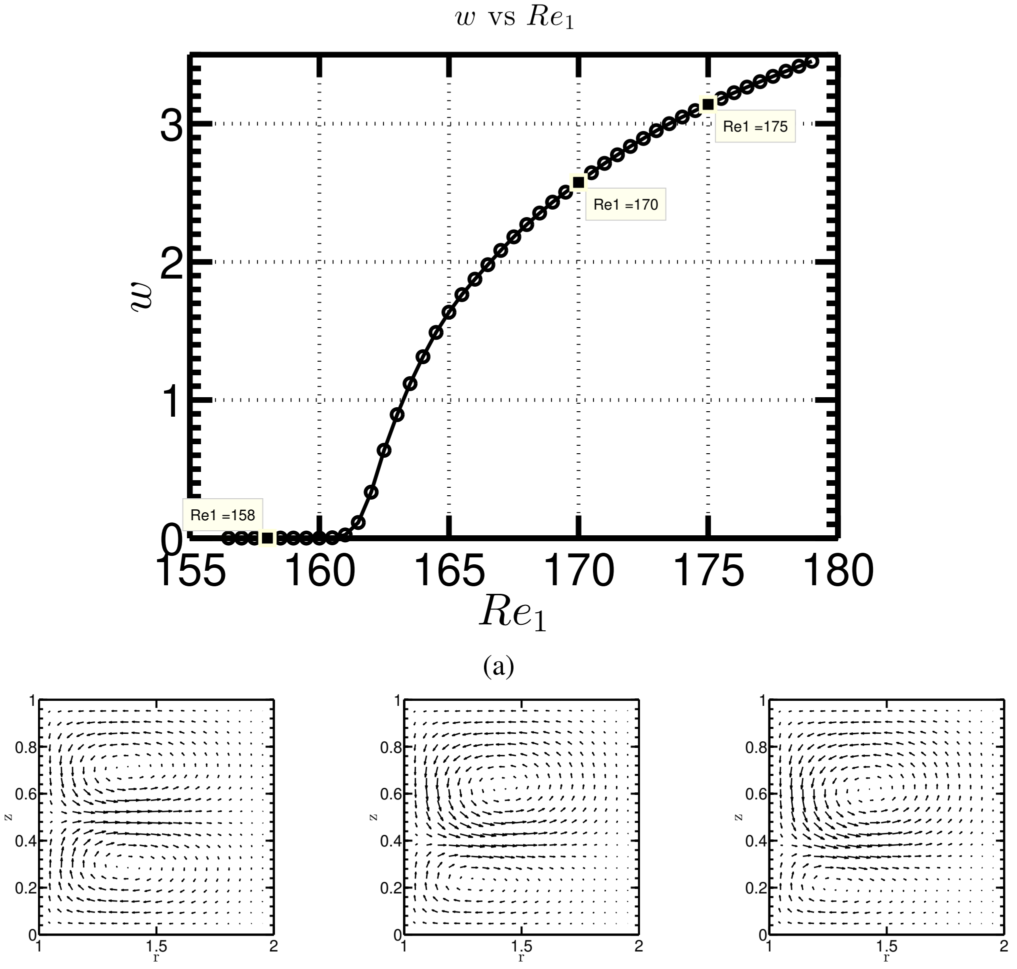

(a)

(b) (c) (d)

Fig. 5.4 Transition from symmetric 2-roll (Panel (b)) to 1-roll (asymmetric 2-roll) solutions (Panel (c) and (d)): (a) Upper branch of the bifurcation diagram of Fig. 4.8d. Velocity plots at points marked in Fig. 5.4a: (b) $Re_1 = 158$, (c) $Re_1 = 170$, (d) $Re_1 = 175$ at $\varepsilon = 0.1$, $Ma = 1$, $Pr = 1$, $\Gamma = 1$.

We changed the magnitude of ε, which in turn changed the provided artificial vertical temperature gradient. It was observed that for $|\varepsilon| < 10^{-6}$, single-cell modes were not realized. This observation suggested that single-cell modes obtained in current results are ‘finite-amplitude’ solutions and at least for the range of Re_1 considered in this study, disconnected from the mid-plane symmetric branch.

Other ways of manifesting these modes were also enumerated. To quantify the bifurcation from a mid-plane symmetric TVF to single-cell modes, axial velocity at mid-plane and mid-height was chosen as the bifurcation quantity. When the flow was mirror symmetric about the mid-plane, the bifurcation quantity was zero and when it was asymmetric, the bifurcating quantity was non-zero. Bifurcation diagrams obtained from different ways of manifesting single-cell modes were superimposed and a good match between them was observed (Fig. 4.10).

Bifurcation diagrams were plotted for a range of values of Γ between 0.8 to 1.24. At $\Gamma > 1.2$ the single-cell branches disconnect completely from the main Taylor-vortex branch. In this sense, single-cell modes became **secondary** or **disconnected modes.** Some speculations were made about the bifurcation scenario and a qualitative phase diagram was plotted in the (Re_1, Γ) plane as given in Fig. 5.5. The line joining circles in Fig. 5.5 represents the locus of limit points - this needs to be confirmed in a future work.

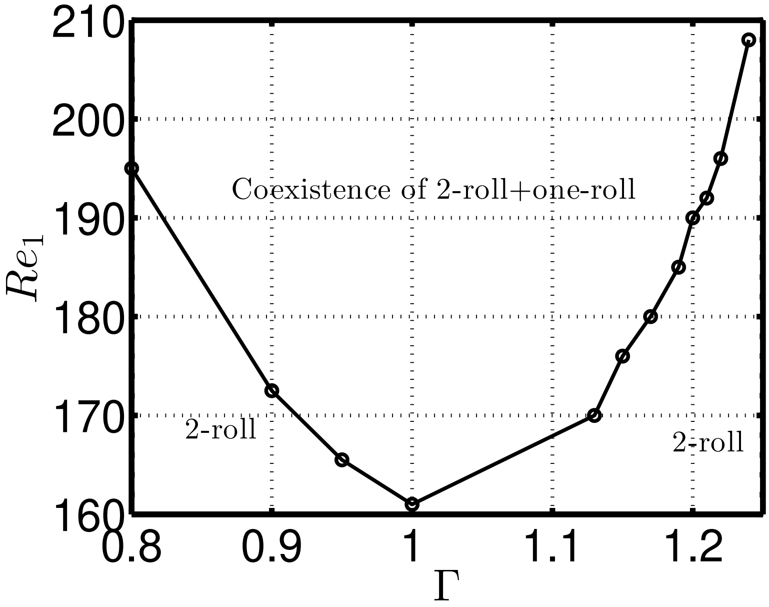

Fig. 5.5 Qualitative phase diagram in the (Re_1,Γ) plane.

Finally, the aspect ratio Γ was varied at a constant Re_1 for a range of Reynolds numbers. Γ was increased from 3.1 to 6.1 and decreased back to 3.1 while keeping Re_1 constant. Some interesting results were observed. At $Re_1 = 100$ and 125, while increasing Γ a $2 \to 4 \to 6$ roll catastrophic transition was observed and while coming back, catastrophic jumps from $6 \to 4 \to 2$ were seen. However, for $Re_1 = 150$ and 200, when increasing Γ, a direct $2 \to 6$-roll jump was observed. On the other hand, when coming back from $\Gamma = 6.1$ to 3.1, again a $6 \to 4 \to 2$ collapse was observed. These findings pointed towards a more complicated catastrophe than a simple cusp. It appears that there exist multiple entangled cusps in the (Re_1, Γ) plane.

Schematics of the hysteresis for four different values of Re_1 ($Re_1 = 100, 125, 150, 200$) are summarized in Fig. 5.6.

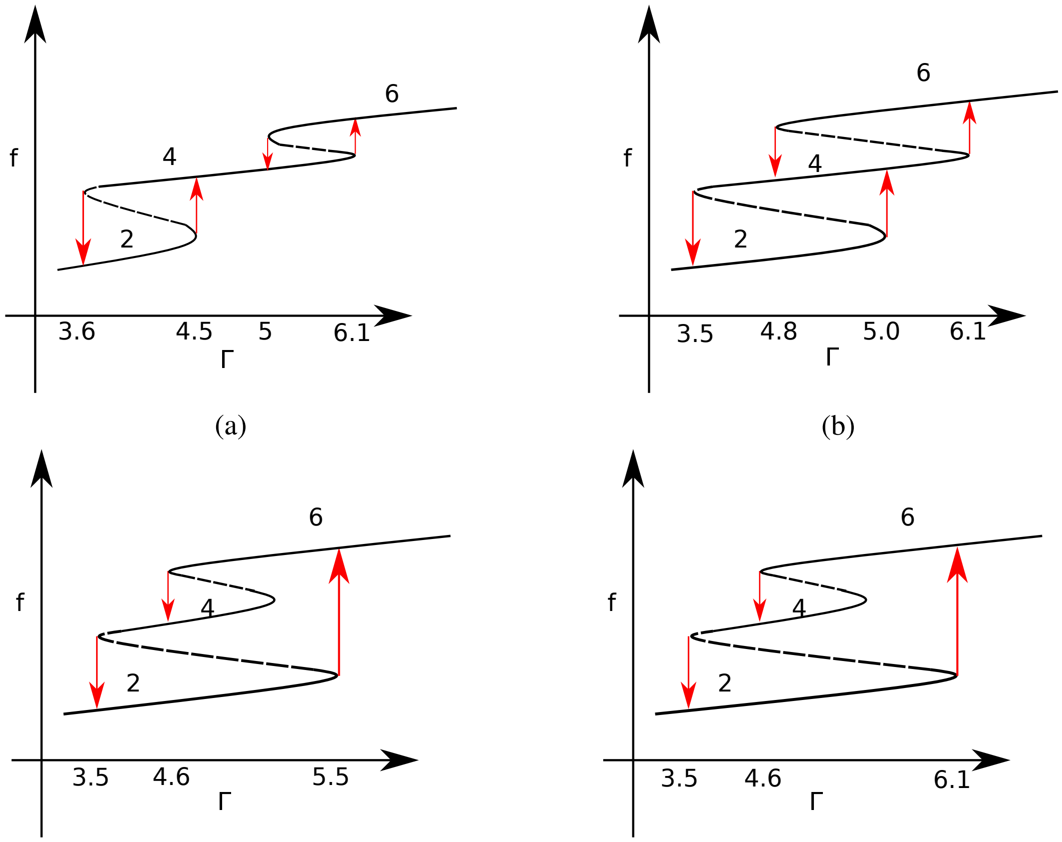

(a) (b) (c) (d)

Fig. 5.6 Schematics of hysteresis for (a) $Re_1 = 100$, (b) $Re_1 = 125$, (c) $Re_1 = 150$, (d) $Re_1 = 200$.

5.3 Possible Future Work

"We are at the very beginning of time for the human race. It is not unreasonable that we grapple with problems. But there are tens of thousands of years in the future. Our responsibility is to do what we can, learn what we can, improve the solutions, and pass them on." - Richard Feynman.

Compressible Taylor-Couette flow is rich in its complexity. Many possible directions can be taken in future to investigate the pattern formation in this system. Some of the possible ways of taking this work forward are enumerated below:

1. Write a continuation routine in order to track unstable branches of bifurcation diagrams at low-aspect ratios.
2. Track high-Re_1 traveling wave solutions of Chapter 3 by decreasing Ma, to check its connection to incompressible TCF.

3. To check if high-Re_1 traveling wave solutions of Chapter 3 survive for rigid top and bottom walls by varying Schaeffer's homotopy parameter τ from 0 to 1 [Schaeffer [34]].
4. Continue single-cell modes obtained in Fig. 4.8 in Ma all the way to $Ma \sim 0$ in order to see their connection with single-cell modes obtained in incompressible TCF.
5. Identify the phase-boundaries of (i) limit-points and (ii) subcritical-solutions in the (Re_1, Γ)-plane in Fig. 5.5.
6. Modify the present code to incorporate nonaxisymmetric effects.
7. Look at pattern formation scenario for dense gases and dilute granular gases.

References

[1] Andereck, C. D., Liu, S., and Swinney, H. L. (1986). Flow regimes in a circular Couette system with independently rotating cylinders. *Journal of Fluid Mechanics*, 164:155–183.

[2] Balbus, S. A. and Hawley, J. F. (1991). A powerful local shear instability in weakly magnetized disks. i-linear analysis. ii-nonlinear evolution. *The Astrophysical Journal*, 376:214–233.

[3] Benjamin, T. and Mullin, T. (1981). Anomalous modes in the Taylor experiment. *Proceedings of the Royal Society of London. Series A*, 377:221–249.

[4] Benjamin, T. B. (1978). Bifurcation phenomena in steady flows of a viscous fluid. I. Theory. In *Proceedings of the Royal Society of London A*, volume 359, pages 1–26.

[5] Chandrasekhar, S. (1960). The stability of non-dissipative couette flow in hydromagnetics. *Proceedings of the National Academy of Sciences*, 46(2):253–257.

[6] Chandrasekhar, S. (1961). Hydrodynamic and Hydromagnetic Stability, Clarendon Press.

[7] Cliffe, K. (1983). Numerical calculations of two-cell and single-cell Taylor flows. *Journal of Fluid Mechanics*, 135:219–233.

[8] Cliffe, K. and Mullin, T. (1985). A numerical and experimental study of anomalous modes in the Taylor experiment. *Journal of Fluid Mechanics*, 153:243–258.

[9] Coles, D. (1965). Transition in circular Couette flow. *Journal of Fluid Mechanics*, 21(3):385–425.

[10] Couette, M. (1890). *Etudes sur le frottement des liquides*. PhD thesis.

[11] Cvitanović, P., Artuso, R., Mainieri, R., Tanner, G., and Vattay, G. (2003). *Chaos: Classical and Quantum (ChaosBook. org)*.

[12] DiPrima, R. and Swinney, H. (1981). *Hydrodynamic Instabilities and the Transition to Turbulence*. Springer, New York.

[13] Golubitsky, M., Stewart, I., et al. (2012). *Singularities and Groups in Bifurcation Theory*, volume 2. Springer Science & Business Media.

[14] Greenspan, H. and Howard, L. (1963). On a time-dependent motion of a rotating fluid. *Journal of Fluid Mechanics*, 17(3):385–404.

[15] Grossmann, S., Lohse, D., and Sun, C. (2016). High–Reynolds number Taylor-Couette turbulence. *Annual Review of Fluid Mechanics*, 48:53–80.

[16] Harada, I. (1980a). A numerical study of weakly compressible rotating flows in a gas centrifuge. *Nuclear Science and Engineering*, 73(3):225–241.

[17] Harada, I. (1980b). Computation of strongly compressible rotating flows. *Journal of Computational Physics*, 38(3):335–356.

[18] Hatay, F. F., Biringen, S., Erlebacher, G., and Zorumski, W. (1993). Stability of high-speed compressible rotating couette flow. *Physics of Fluids A: Fluid Dynamics*, 5(2):393–404.

[19] Hyun, J. M. and Park, J. S. (1992). Spin-up from rest of a compressible fluid in a rapidly rotating cylinder. *Journal of Fluid Mechanics*, 237:413–434.

[20] Kao, K.-H. and Chow, C.-Y. (1992). Linear stability of compressible Taylor–Couette flow. *Physics of Fluids A: Fluid Dynamics*, 4(5):984–996.

[21] Kuhlthau, A. (1960). Recent low-density experiments using rotating cylinder techniques (ed. F. M. Devienne). In *Rarefied Gas Dynamics*, pages 192–200.

[22] Lele, S. K. (1992). Compact finite difference schemes with spectral-like resolution. *Journal of Computational Physics*, 103(1):16–42.

[23] Malik, M., Alam, M., and Dey, J. (2006). Nonmodal energy growth and optimal perturbations in compressible plane Couette flow. *Physics of Fluids*, 18(3):034103.

[24] Malik, M., Dey, J., and Alam, M. (2008). Linear stability, transient energy growth, and the role of viscosity stratification in compressible plane Couette flow. *Physical Review E*, 77(3):036322.

[25] Mallock, A. (1889). Determination of the viscosity of water. *Proceedings of the Royal Society of London*, 45(273-279):126–132.

[26] Manela, A. and Frankel, I. (2007). On the compressible Taylor–Couette problem. *Journal of Fluid Mechanics*, 588:59–74.

[27] Marcus, P. S. (1984). Simulation of Taylor-Couette flow. Part 1. Numerical methods and comparison with experiment. *Journal of Fluid Mechanics*, 146:45–64.

[28] Mullin, T. (1981). Anomalous modes in the Taylor experiment. *Proc. R. Soc. Lond. A*, 377(1770):221–249.

[29] Mullin, T. (1982). Mutations of steady cellular flows in the Taylor experiment. *Journal of Fluid Mechanics*, 121:207–218.

[30] Newton, I. (1999). *The Principia: mathematical principles of natural philosophy*. Univ of California Press.

[31] Orszag, S. A. (1971). Accurate solution of the Orr–Sommerfeld stability equation. *Journal of Fluid Mechanics*, 50(4):689–703.

[32] Pfister, G., Schmidt, H., Cliffe, K., and Mullin, T. (1988). Bifurcation phenomena in Taylor-Couette flow in a very short annulus. *Journal of Fluid Mechanics*, 191:1–18.

[33] Rayleigh, L. (1917). On the dynamics of revolving fluids. *Proceedings of the Royal Society of London. Series A*, 93(648):148–154.

[34] Schaeffer, D. G. (1980). Qualitative analysis of a model for boundary effects in the Taylor problem. In *Mathematical Proceedings of the Cambridge Philosophical Society*, volume 87, pages 307–337.

[35] Shi, L., Rampp, M., Hof, B., and Avila, M. (2015). A hybrid MPI-OpenMP parallel implementation for pseudospectral simulations with application to Taylor–Couette flow. *Computers & Fluids*, 106:1–11.

[36] Stokes, G. G. (2009). *Mathematical and Physical Papers*, volume 1 of *Cambridge Library Collection - Mathematics*. Cambridge University Press.

[37] Strogatz, S. H. (2014). *Nonlinear Dynamics and Chaos*. Westview press.

[38] Sutherland, W. (1893). The viscosity of gases and molecular force. *The London, Edinburgh, and Dublin Philosophical Magazine and Journal of Science*, 36(223):507–531.

[39] Taylor, G. I. (1923). Stability of a viscous liquid contained between two rotating cylinders. *Philosophical Transactions of the Royal Society of London. Series A*, 223:289–343.

[40] Velikhov, E. (1959). Stability of an ideally conducting liquid flowing between cylinders rotating in a magnetic field. *Sov. Phys. JETP*, 36(9):995–998.

[41] Welsh, S., Kersalé, E., and Jones, C. A. (2014). Compressible Taylor–Couette flow–instability mechanism and codimension 3 points. *Journal of Fluid Mechanics*, 750:555–577.

[42] Zeeman, E. C. (1976). Catastrophe Theory. *Scientific American*, 234(4):65–83.

[43] Zhang, K. K., Shotorban, B., Minkowycz, W., and Mashayek, F. (2006). A compact finite difference method on staggered grid for Navier–Stokes flows. *International Journal for Numerical Methods in Fluids*, 52(8):867–881.